Superconductivity in $BaFe_{2-x}Ru_xAs_2$ System and Investigation of its Critical Properties

By

SHILPAM SHARMA

Enrolment No: PHYS02200704004

Indira Gandhi Centre for Atomic Research, Kalpakkam

A thesis submitted to the Board of Studies in Physical Sciences

In partial fulfillment of the requirements For the Degree of

DOCTOR OF PHILOSOPHY

of

HOMI BHABHA NATIONAL INSTITUTE

February, 2013

Homi Bhabha National Institute

Recommendations of the Viva Voce Board

As members of the Viva Voce Board, we certify that we have read the dissertation prepared by **Shilpam Sharma** entitled **"Superconductivity in $BaFe_{2-x}Ru_xAs_2$ System and Investigation of its Critical Properties"** and recommend that it may be accepted as fulfilling the dissertation requirement for the Degree of Doctor of Philosophy.

_____Date:
Chairman-

_____Date:
Guide/Convener-

_____Date:
Examiner-

_____Date:
Member 1-

_____Date:
Member 2-

_____Date:
Member 3-

Final approval and acceptance of this dissertation is contingent upon the candidate's submission of the final copies of the dissertation to HBNI.

CERTIFICATE

I hereby certify that I have read this dissertation prepared under my direction and recommend that it may be accepted as fulfilling the dissertation requirement.

Dr. C. S. Sundar

Date:

Place:

STATEMENT BY AUTHOR

This dissertation has been submitted in partial fulfillment of requirements for an advanced degree at Homi Bhabha National Institute (HBNI) and is deposited in the Library to be made available to borrowers under rules of the HBNI.

Brief quotations from this dissertation are allowable without special permission, provided that accurate acknowledgement of source is made. Request for permission for extended quotation from or reproduction of this manuscript in whole or in part may be granted by the Competent Authority of HBNI when in his or her judgement the proposed use of the material is in the interests of scholarship. In all other instances, however, permission must be obtained by the author.

Shilpam Sharma

DECLARATION

I, hereby declare that the investigation presented in the thesis has been carried out by me. The work is original and has not been submitted earlier as a whole or in part for a degree / diploma at this or any other Institution / University.

Shilpam Sharma

To my loving Family

ACKNOWLEDGEMENTS

I would like to thank my supervisors Dr. C. S. Sundar and Dr. A. Bharathi for their able guidance and constant encouragement during the course of the work presented in this thesis.

I would like to thank my colleagues and collaborators Dr. Awadhesh Mani Tiwari, Shri A. T. Satyanarayna, Shri T. R. Devidas, Dr. K. Vinod and Dr. Edward Prabu for their help in carrying out measurements and for very interesting and helpful discussions on many parts of my work.

I would like to thank Dr. Baban Dhonge for his support and precious friendship.

I would like to thank Dr. Oliver H. Seeck, PETRA -3 synchrotron, Hamburg, Germany and Dr. Anil K. Sinha, INDUS II synchrotron, RRCAT, Indore, India for their generous support extended to us during the measurement of low temperature HRXRD and powder ADXRD measurements on our samples.

I am thankful to my parents and brother for their support, love, encouragement and belief in me. Last, but not least, I would like to thank my wife Neha who gave me strength and support during tough times, and also played a vital role in completion of this dissertation.

CONTENTS

Chapter 1

Superconductivity in $BaFe_2As_2$: An Overview

This chapter presents a brief account of the discovery of superconductivity in Fe-pnictogen based compounds. The crystal structures, magnetic and electronic structure of $BaFe_2As_2$ system are described. Various methods to stabilize superconductivity in the $BaFe_2As_2$ parent system are presented. With the help of examples of charge and neutral substitutions in $BaFe_2As_2$, the need to manipulate crystal structure for inducing bulk superconductivity in the system is emphasized. The motivation to substitute isovalent Ru at Fe site to induce superconductivity in $BaFe_2As_2$ is presented. The introductory chapter ends with a brief survey of various experimental investigations on this new superconductor that forms the content of the thesis.

1.1 Superconductivity in Iron-Pnictide based compounds

The study of iron-pnictide based high T_C superconductors had its genesis with the discovery of superconductivity in LaFePO at 4 K, in 2006 by Kamihara *et al.* [1]. Two years later, the same group discovered that the fluorine doping at oxygen site in the iron-arsenic based system ($LaFeAsO_{1-x}F_x$) induces superconductivity at 26 K [2]. The discovery of superconductivity in iron-pnictide (Fe-Pn) systems created much stir in the community as it was discovered in a wide range of structures containing Fe-Pn layers and the T_C was soon raised to 43 K in $LaO_{1-x}F_xFeAs$ under pressure of 4 GPa [3] increasing

marginally to a high of 56 K in $Gd_{1-x}Th_xFeAsO$ [4]. The flurry of research in this field was mainly due to the similarity of these compounds to the previously discovered cuprates [5].

The ability to create a wide variety of novel iron-pnictide based superconductors through chemical substitutions has allowed for the optimization of superconducting transition temperature and resulted in a number of families of superconductors with varying Fe-Pn layers and crystal structures. The crystal structures of the four main families of compounds are shown in figure 1.1. The large number of iron based superconductors discovered can be grouped under four major families based on the different types of crystal structures [6]: (i) the *RE*1111 family (*RE*=La, Ce, Pr, Nd, Sm, Tb, Dy) of Fe pnictides with the ZrCuSiAs type structure having T_C in the range of 25–55 K. (ii) The *AE*-122 family (*AE*=Ba,Sr, Ca), of which the $Ba_{1-x}K_xFe_2As_2$ with T_C about 38 K has $ThCr_2Si_2$ type structure. (iii) The third category is the 111 family of compounds, comprising of systems like $Li_{1-x}FeAs$ with T_C ~ 18 K and (iv) a non-arsenic family of compounds termed the 11 family consisting of compounds viz., $FeSe_x$, $FeSe_{1-x}Te_x$ with the α-PbO-type structure, having a T_C maximum of up to 14 K [7] that shows an increase with pressure up to a high value of T_C ~ 38 K [7].

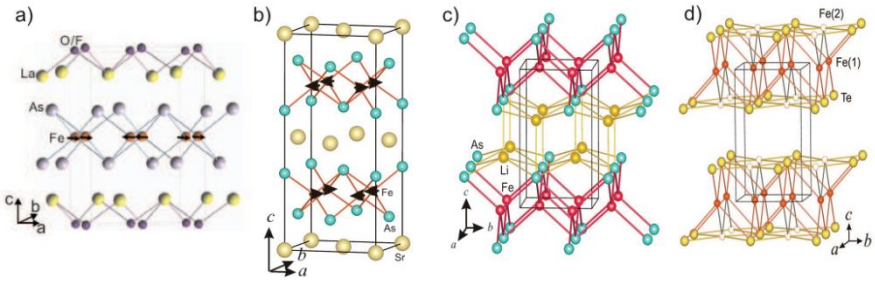

Figure 1.1: (a) crystal structure of $LaFeAsO_{1-x}F_x$, (b) $SrFe_2As_2$, (c) LiFeAs, and (d) $Fe_{1-x}Te$ family of iron based superconductors. The Fe atoms in the square lattice are tetrahedrally coordinated to pnictogen atoms (As, or Te). The figure is taken from Johnston et.al. (ref. 6)

In all of the above systems, detailed studies on the normal and superconducting state have been carried out (reference [6]). These include studies on the evolution of structure, magnetic and superconducting properties with various dopants [6]. Amongst the various families of iron based superconductors, the superconductors based on the $BaFe_2As_2$ system have been extensively investigated. These turn out to be the canonical system for the Fe-Arsenide superconductors, as they are structurally simple, can be grown in single crystalline form, and are amenable to in-depth investigations.

1.2 The $BaFe_2As_2$ system

The synthesis of $BaFe_2As_2$ was already reported in 1980, but excepting for the crystal structure and magnetic data, no physical properties were known at that time [8]. In the following, we briefly indicate the crystal and magnetic structure, electronic structure, *T-x* phase diagram obtained under pressure, by doping at Fe, Ba and As site and the superconducting as well as critical state properties of $BaFe_2As_2$ system of compounds.

1.2.1 Crystal structure

The ternary iron arsenide $BaFe_2As_2$ crystallizes with tetragonal $ThCr_2Si_2$ type structure (I4/mmm space group). Figure 1.2 shows the room temperature crystal structure of $BaFe_2As_2$ taken from reference [9]. Upon cooling below 140 K, the ternary $BaFe_2As_2$ undergoes a structural phase transition from high temperature tetragonal to low temperature orthorhombic structure having *Fmmm* symmetry [10]. The '*a*' and '*b*' lattice parameters change continuously with decreasing temperature [10]. This continuous variation in unit cell parameters suggests that the high temperature tetragonal phase transforms in low temperature orthorhombic phase below 140 K via second order phase

transition [11]. The resulting distortion can be visualized as a stretching of the tetragonal structure along the diagonal of the square face along [110] direction. The square nets of Fe become rectangular with Fe-Fe distances of 2.79 Å and 2.81 Å [9]. Chemical substitutions and mechanical pressure can be used to suppress structural phase transition and stabilize superconductivity in the system. Such studies of the crystal structure of Ru-substituted $BaFe_2As_2$ across the structural transition were performed and are presented in chapter 3 of present thesis.

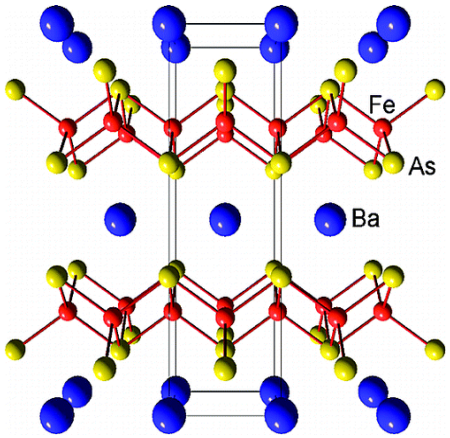

Figure 1.2: Crystal structure of the $BaFe_2As_2$. At room temperature, in the tetragonal phase, the Fe atoms form a square net, and each Fe atom is coordinated to four As atoms. This results in layers of edge sharing, slightly distorted tetrahedra [9]. The Ba atoms are coordinated by eight *As* atoms in a distorted cubic environment by ionic Ba-As bonds. The lattice parameters at room temperature are '*a*' = 3.963 Å and '*c*' = 13.017 Å, with the Ba at the Wyckoff position *2a*, Fe at *4d*, and As at *4e*. The fractional coordinate of arsenic z_{As} = 0.355 [10]. The different interatomic distances are $d_{Fe\text{-}Fe}$ = 2.80 Å, $d_{Fe\text{-}As}$ = 2.40 Å, and $d_{Ba\text{-}As}$ = 3.38 Å.

1.2.2 Magnetic structure

In $BaFe_2As_2$, the structural phase transition is almost coincident with an antiferromagnetic transition to spin density wave (SDW) ground state, from a room temperature paramagnetic state [12]. The heat capacity as a function of temperature

shows a single large and well defined anomaly at the structural/magnetic transition temperature in the compound [6, 9, 13]. The antiferromagnetic transition has been established through temperature dependent neutron diffraction measurements [11, 14], and is reflected in the resistivity and magnetization measurements [15].

The magnetic structure of $BaFe_2As_2$ is stripe type and is shown in figure 1.3. The magnetic moments on the Fe atoms are arranged ferromagnetically along the longer Fe-Fe distance in the rectangular Fe nets (along '*b*' axis) but antiferromagnetic ordering of the moments can be seen along the '*a*' and '*c*' axes [9]. The magnetic moment on individual iron atoms was found to be around $0.87\mu_B$ [14, 16]. The magnetic properties have been investigated through detailed electronic structure calculations [17].

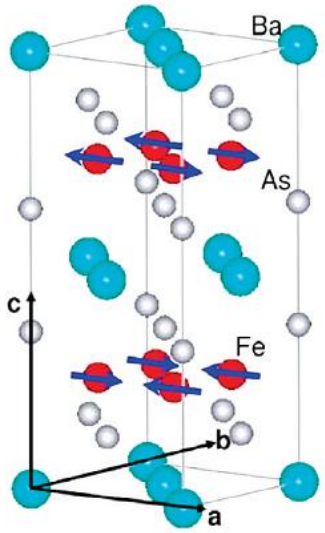

Figure 1.3: Magnetic structure of the parent compound $BaFe_2As_2$ below the SDW transition temperature T_{SDW} ~140 K. The magnetic moments form ferromagnetic chains along '*b*' axis which is longer Fe-Fe distance in rectangular Fe nets but are antiferromagnetically ordered along '*a*' and '*c*' axes. Figure from Mandrus et al. [9] and references there in.

1.2.3 Electronic structure

$BaFe_2As_2$ is a semimetal [9] with all the five *3d* Fe bands crossing the Fermi level. Substantial Fe-Fe interactions are expected in the compound due to relatively short Fe-Fe bond lengths. Band structure calculations based on local density approximation have been carried out [18] and it has been found that the states near the Fermi level are derived exclusively from the Fe orbitals. The density of states and the Fermi surface of $BaFe_2As_2$ as calculated by Singh *et al.* [18] is shown in figure 1.4.

The Fermi surface in general is crossed by five bands formed by the *d*-states of the iron [18]. Of these, three contribute to the hole-like Fermi surface pockets close to the Γ-point, and the other two are electron-like pockets at the corners of Brillouin zone [18, 19]. Thus there are three hole-like cylinders at the Brillouin zone center and two electron-like cylindrical Fermi-surfaces at the zone corners. The almost cylindrical form of the Fermi surfaces reflects the quasi-two dimensional nature of the electronic structure. Calculations also reveal that $BaFe_2As_2$ is a high density of states semimetal. The density of states increases strongly below the Fermi energy E_F. The electronic structure near the Fermi level is extremely sensitive to the fractional coordinate of the arsenic (z_{As}) [20].

These Fermi surface topologies have been verified experimentally by angle resolved photo emission measurements on $BaFe_2As_2$ [21]. The angle resolved photo emission spectroscopy measurements on $BaFe_2As_2$ revealed that even though the Fermi surface is strongly three-dimensional, it does indeed have long parallel segments along the k_z direction that leads to the magnetic order [22]. In addition, in-commensurate nesting of Fermi surface in the *ab-plane* was found at low temperatures. The superconductivity in the system emerges only when this nesting of Fermi surface is

destroyed by chemical substitution or under pressure. Mazin *et al.* [23] showed that the superconductivity in these FeAs based compounds is mediated by antiferromagnetic spin fluctuation, which are different from the usual super-exchange. The resulting state is extended *s-wave* pairing with a sign reversal of the order parameter between different Fermi surface sheets [23].

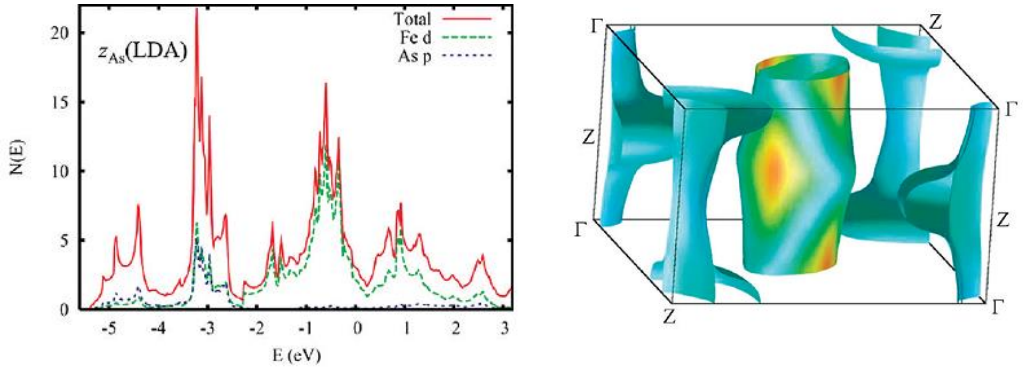

Figure 1.4: Fermi surface of the $BaFe_2As_2$ and LDA density of sates calculated using the experimental fractional coordinate of arsenic. The Fermi surface is crossed by five bands formed by the *d*-states of iron. Three hole-like Fermi surface pockets lie close to Γ-points and two electron-like Fermi surface pockets at corner of Brillouin zone. The details of the electronic structure near Fermi level are strongly dependent on the As position. Figure from Singh *et al.* [18].

1.2.4 Transport and magnetic properties

At room temperature $BaFe_2As_2$ is a poor metal with room temperature resistivity of ~ 430 μΩ-cm along *ab*-plane. The layered structure gives rise to anisotropy in the electronic properties and the resistivity anisotropy ~100 [6, 15]. Figure 1.5 presents the results [24] of resistivity as function of temperature in $BaFe_2As_2$ single crystal. A sharp decrease in resistivity, associated with the SDW transition is clearly seen. The decrease in resistivity at the SDW transition has attracted considerable attention and has been understood in terms of the dispersion of the bands near the Fermi surface of $BaFe_2As_2$.

Using band structure calculations, it has been suggested that because of the down folding of the bands to accommodate the magnetic order, Dirac cone states with linear energy versus wave vector (*E* vs. *K*) dispersion could occur [25]. ARPES measurements [26] have indeed confirmed the presence of linear dispersion. The observation of metallic resistivity in the SDW ground state of the $BaFe_2As_2$, despite the reduction in the number of carriers due to Fermi surface nesting is now thought to be due to increase in the mobility of charge carriers on account of zero effective mass and long mean free path of Dirac cone electrons.

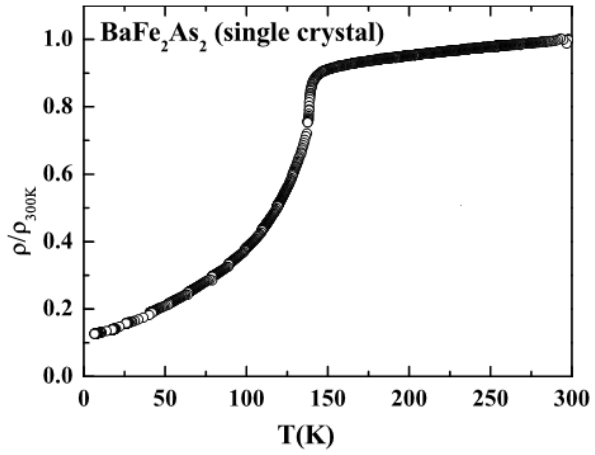

Figure 1.5: Resistivity as function of temperature for $BaFe_2As_2$ single crystal shows a signature at the magnetic/structural phase transition. This anomaly in the resistivity is due to SDW transition confirmed by neutron diffraction measurements. In the SDW ground state, the resistivity is seen to fall steeply with temperature. (Figure from A. Mani et. al. [24])

Temperature dependent susceptibility in $BaFe_2As_2$ also shows signature of SDW transition, marked by a fall in the susceptibility, as evident from susceptibility vs. temperature plot for $BaFe_2As_2$ is shown in figure 1.6 [9]. At room temperature, susceptibility along '*c*' axis and *ab-plane* is $6x10^{-4}$ cm^3mol^{-1}. With decrease in temperature the susceptibility decreases, a behavior opposite to that expected from Curie-Weiss law, which suggests the absence of local magnetic moments above T_{SDW}.

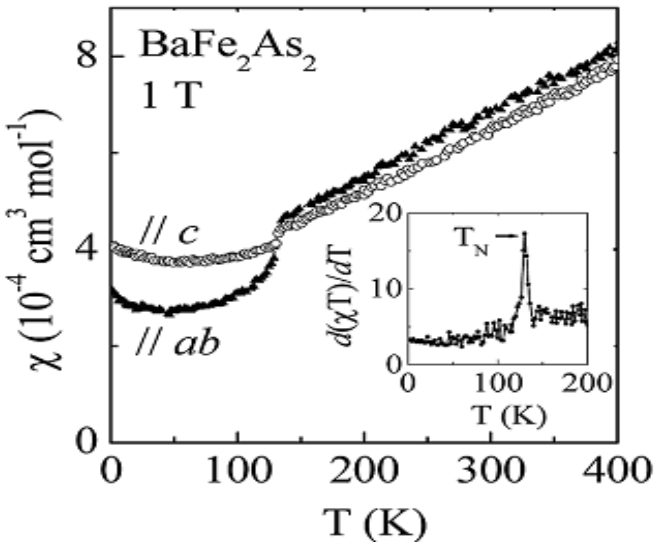

Figure 1.6: Anisotropic magnetic susceptibility of $BaFe_2As_2$ showing a linear dependence above T_{SDW}. Inset shows the peak in the derivative of susceptibility vs. temperature plot marking the T_{SDW}. Figure is taken from reference [9].

1.3 Superconductivity in $BaFe_2As_2$ system

The parent compound $BaFe_2As_2$ does not show any sign of superconductivity down to the lowest achievable temperatures. However, by charge doping on the Ba or Fe site, isovalent substitution at As site or under application of pressure, the superconducting ground state gets stabilized in the system [9].

1.3.1 Doping at Ba site in $BaFe_2As_2$

The first chemical change in the $BaFe_2As_2$ that stabilized superconductivity in the system was by alkali metal doping at Ba site. K-doped $Ba_{1-x}K_xFe_2As_2$ polycrystalline samples were synthesized by Rotter *et al.* [27]. It was found that with substitution, the SDW transition gradually gets suppressed and at substitution level of x = 0.4, the structural-magnetic phase transition were completely suppressed and superconductivity

was induced at T_C ~ 38 K. In figure 1.7, we present *R(T)* plot from Rotter *et al.* [27] showing superconducting transition at ~ 38 K.

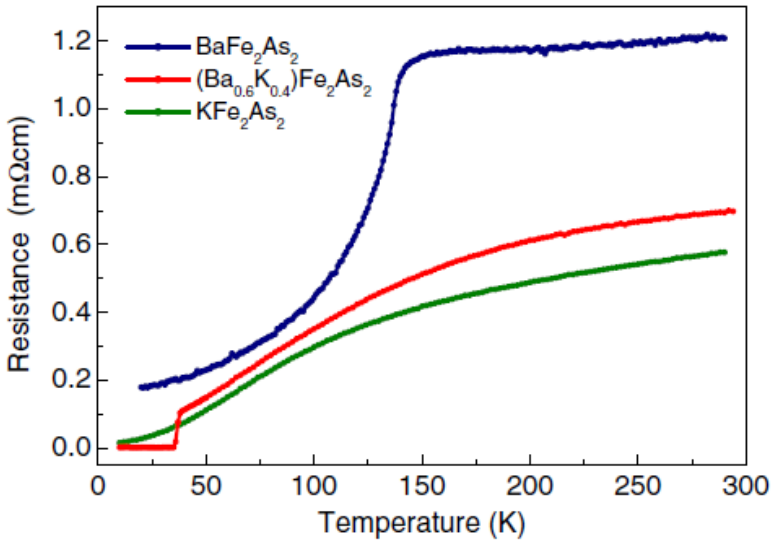

Figure 1.7: Electrical resistance of $BaFe_2As_2$, $Ba_{0.6}K_{0.4}Fe_2As_2$ and KFe_2As_2. K-doping drives the parent $BaFe_2As_2$ system into superconducting ground state at ~38 K. KFe_2As_2 behaves as a good metal but no superconductivity has been observed. Figure is taken from reference [27].

For the $Ba_{1-x}K_xFe_2As_2$ system, the superconducting transition temperature versus *x* shows a dome like feature. The substitution of potassium in place of Ba results in increase in '*c*' but a decrease in '*a*' lattice parameter. The single crystalline samples were later on synthesized using Sn flux [28] and self-flux of pre-reacted Ba and K [29]. The small size of the single crystals and the non-homogeneity of the K-doping across the single crystal restricted the use of these highest T_C superconducting samples for serious studies in understanding the normal and superconducting properties. The occurrence of highest T_C by K-doping at Ba site in the $BaFe_2As_2$ as compared to substitutions at the Fe site, suggests the influence of atom disorder in the Fe layer on the superconductivity in these systems.

1.3.2 $BaFe_2As_2$ under pressure

Under pressure the behavior of $BaFe_2As_2$ changes radically. With application of pressure the SDW transition and the structural transitions get suppressed and superconductivity occurs in the system. The onset of bulk superconductivity with a maximum T_C ~ 29 K in single crystalline $BaFe_2As_2$ under a pressure of 2 - 2.8 GPa was first reported by Alireza *et al.* [30]. The high pressure electrical resistivity studies carried out by Fukazawa *et al.* [31] on polycrystalline samples indicated superconducting transition at about 20 - 30 K above 2 GPa. The superconducting phase was found at pressures > 6 and 13 GPa [30, 31]. The value of the T_C was found to depend upon the degree of non-hydrostaticity of the apparatus used. Here we present the results of high pressure studies on $BaFe_2As_2$ from Mani *et al.* [24], where the T_C of the order of 33 K has been observed at ~1.4 GPa in non-hydrostatic pressure cell. The R(T) behavior of single crystals of $BaFe_2As_2$ observed under application of pressure in a quasi-hydrostatic cell is shown in figure 1.8. T_C exhibited an initial increase followed by decrease at higher pressures, while SDW and structural transitions were seen to quickly vanish [24]. This feature of *T-p* phase diagram is similar to the doping induced superconducting phase diagrams [32].

Even though the maximum T_C achievable through the application of pressure is high, the transition widths are observed to be large. The effect of non-hydrostatic conditions and the strain sensitivity of the FeAs based materials could be a possible reason for the broad transitions in $BaFe_2As_2$ system under pressure [33].

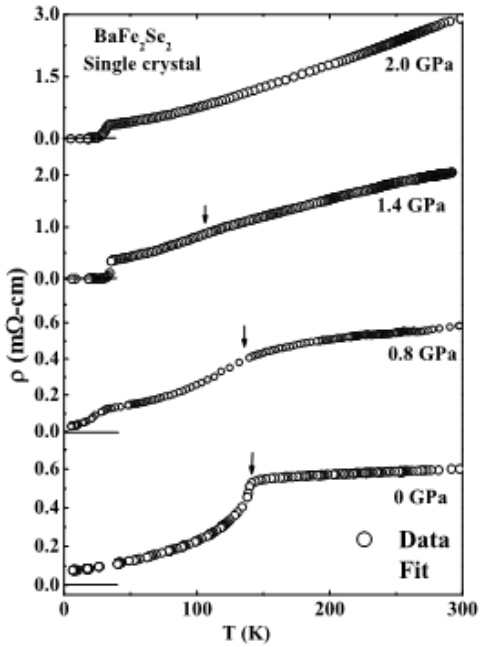

Figure 1.8: Temperature-dependent resistivity curves of the single-crystalline $BaFe_2As_2$ samples under pressures indicated in each panel. The zero of each panel is indicated by horizontal thick line. Downward arrows indicate the positions of T_{SDW} at various pressures. The figure clearly shows suppression of magnetic transition and stabilization of superconductivity with increase in pressure. Figure is taken from reference [24].

1.3.3 3*d*- and *4d*- Transition Metal substitutions at Fe site

There have been several studies on transition metal *(TM)* doping at Fe site. Most extensive investigations have been performed on Co-doped $BaFe_2As_2$, which we report below. Transition metal doping that led to the suppression of structural and magnetic phase transition and stabilized superconductivity was by Co atoms at the Fe site in $BaFe_2As_2$ system [34]. It was found that as the Co atoms replaces Fe, the resistive signature of the combined structural and magnetic phase transition gets modified [12]. At intermediate doping, whereas a clear structural and magnetic ordering can be seen, superconductivity was also found to stabilize, suggestive of a region of co-existence of superconductivity and magnetism. For still higher Co concentrations, the structural-magnetic transitions were found to be fully suppressed and superconducting transition

temperature was found to pass through a dome shaped maxima as a function of fraction of Co concentration.

Using x-ray and neutron diffraction studies along with data from resistivity and magnetic susceptibility, a *T-x* phase diagram was proposed (see figure 1.9) [35]. The phase diagram shown in figure 1.9 is remarkable as it shows that the superconductivity is robust despite in-plane disorder, due to the substitution of Co at Fe site. The structural and magnetic transitions split upon doping with Co, as the sample is cooled, it first undergoes a structural phase transition to orthorhombic phase and at a still lower temperature it orders antiferromagnetically. The split in the structural and magnetic phase transitions has not been observed in hole doped superconducting $BaFe_2As_2$ systems [9].

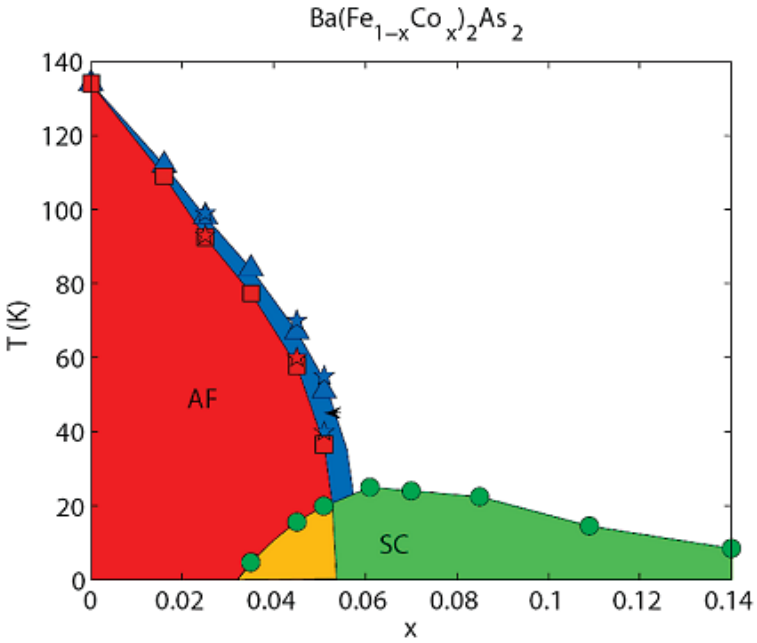

Figure 1.9: Phase diagram of $Ba(Fe_{1-x}Co_x)_2As_2$. The structural and magnetic transitions separate upon doping with Co. For lower doping levels, superconductivity is seen to co-exist with the antiferromagnetic order in the system. Superconducting transition temperature goes through a maximum upon increasing '*x*' and forms a dome like phase diagram. Figure is taken from reference Mandrus et.al.[9].

To determine how general the above *T-x* phase diagram of $BaFe_{2-x}Co_xAs_2$ system is, other higher *Z 3d-* and *4d-* transition metals have also been substituted for Fe and single crystalline samples of $BaFe_{2-x}TM_xAs_2$ (*TM*= Ni, Cu, Rh, Pd) grown [36, 37]. The Ni-doped system shows similar trends in properties as the Co-doped system. Here also the structural and magnetic phase transitions were found to occur at slightly different temperatures. The exception however is Cu, which even though suppresses and splits structural and magnetic phase transitions with increasing concentration, does not give rise to superconductivity in the system. A comparison of the *T-x* phase diagram [12] for the Ni, Co and Cu doped systems show that the suppression of the structural and magnetic phase transitions are similar but the superconducting dome do not fall on a single curve [12]. The Co and Rh *T-x* phase diagrams as well as Ni and Pd *T-x* phase diagrams were found to be similar. The phase diagrams are seen to be similar for dopants along the column of the periodic table, which points to the minor role of steric effects in determining the ground states of these compounds. Unlike hole doping by K at the Ba site, no superconductivity was found in Cr doped $BaFe_{2-x}Cr_xAs_2$ system [38]. The Cr doping suppresses structural and magnetic transitions but no splitting of the two transitions was observed. The slow rate of suppression of the structural-magnetic transitions by Cr may not be enough to induce superconductivity.

The effect of *3d-* and *4d- TM*-doping on the lattice parameters of $Ba(Fe_{1-x}TM_x)_2As_2$ are different [12]. For *3d*-doping, whereas the changes in the *a*-lattice parameter, unit cell volume, and the *a/c* ratio do not scale well with doping fraction '*x*', [39] the variation of *c*-parameter alone was found to scale with '*x*'. In the case of *3d*-doping the *a/c* ratio scales well with charge '*e*'. This imply that for *3d-TM*-doping the

change in '*x*' and the *c*-lattice parameters or charge '*e*' and *a/c* ratio are equivalent parameters [12]. while for the *4d-TM*-dopings *c*-lattice parameter and *c/a* ratio changes in a different manner from the *3d*- doping thus pointing to the fact that the '*x*' or the charge '*e*' are not equivalent to any combinations of the lattice parameters [12] . The superconducting region of the phase diagram of transition metal doping, while do not scale with '*x*', some correlation is seen to exist with the net charge '*e*' donated by the doped atoms. The superconducting dome in the over-doped region is seen to collapse on to one single curve when scaled with the charge '*e*'[12].

1.3.4 Isovalent substitutions in the $BaFe_2As_2$

One of the isovalent doping that attracted attention was phosphorus doping at As site. It is the only successful substitution in parent compound $BaFe_2As_2$ at As site and isovalent phosphorus substitution induces superconductivity at ~30 K [40, 41]. The T_C ~ 30 K, being larger than that obtained by transition metal ion substitution at Fe again suggests noninvolvement of Fe layer induces superconductivity at higher temperatures. The stabilization of superconductivity by isovalent phosphorus substitution suggests that charge doping is not a requirement for the superconductivity to exist in Fe based superconductors. In fact, superconductivity by phosphorus doping is sometimes ascribed to the effect of chemical pressure caused by shrinking of unit cell. It was shown by Kimber *et al.* [42] that in $BaFe_2As_2$ the key structural changes like suppression of tetragonal to orthorhombic phase, reduction in Fe-Fe bond lengths, and distortions in the $FeAs_4$ tetrahedra due to changes in As-Fe-As bond angles, show the same behavior under pressure as found in chemically substituted $BaFe_2As_2$ samples. It was also shown [42] that the electronic structure evolves in similar manner in both the cases. The similarity in

the alteration in As-Fe-As angles due to pressure and K-doping in $BaFe_2As_2$ are shown in figure 1.10 (figure taken from reference [42].

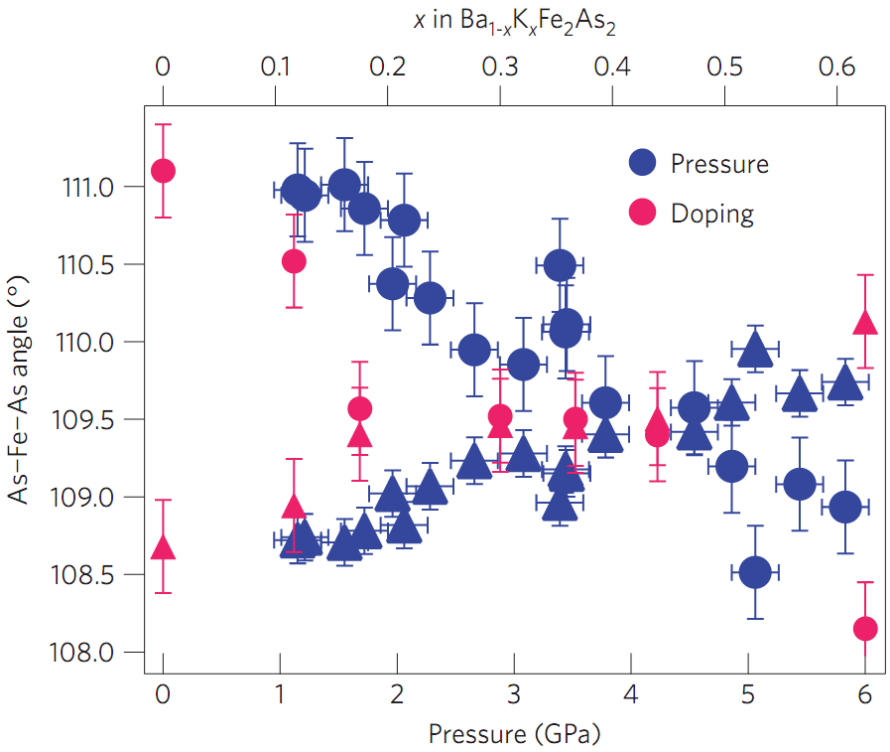

Figure 1.10: Variation of As-Fe-As bond angles as a function of external pressure and chemical doping (K-doping) in $BaFe_2As_2$. The similarity between the changes in structural parameters introduced by pressure and chemical substitutions suggest that suppression of the nesting of Fermi surface and destabilization of SDW state are necessary for the superconductivity to emerge in the iron arsenide superconductors. Figure is taken from reference Kimber et.al. [42].

While isovalent substitution by P at As site induces superconductivity, isovalent substitution of the Sr at Ba site in $BaFe_2As_2$ does not induce superconductivity in spite of the similar volume changes induced in the unit cell like in the case of P-substitution at As site [43]. Thus chemical pressure is an over-simplified cause of superconductivity by charge-neutral doping. Alternatively, alteration of local crystal structure leading to electronic structure changes could be the origin of inducing superconductivity [43]. In the case of phosphorus doping the structural and magnetic transitions are suppressed due to

the increase in the width of the *d*-bands, which in turn leads to the shorter Fe-As bonds due to its strong coupling to magnetic state. No significant contraction of the Fe-As bond length was observed for the case of Sr-doping at the Ba site and the SDW ground state was found to persist even though cell volume changes were similar to the case of phosphorus substitution [43]. It was found by x-ray measurements that the As and P are statistically distributed but remain at different fractional coordinates z_{As} and z_P thereby giving different Fe-As and Fe-P bond lengths. The Fe-As bond length contracts strongly at low doping levels where the magnetic ordering gets suppressed [43].

1.4 Critical state properties of $BaFe_2As_2$ based superconductors

The upper critical field, mass anisotropy and critical current density for the electron and hole doped $BaFe_2As_2$ system have been extensively studied [44-46]. These compounds show high upper critical fields ~ 40- 60 T and a very small anisotropy ~ 2-3. The critical current density of these superconductors ranges from 10^9 to 10^{10} A/m^2 [47]. The high value of upper critical fields, critical current density [48] and a very small anisotropy makes these superconductors suitable for applications when compared to the copper based high T_C materials. The vortex state behavior of the Co-doped $BaFe_2As_2$ system shows a wide variety of vortex phases and flux dynamics. The rich $\mu_0 H$-T vortex phase diagram of doped $BaFe_2As_2$ based superconductors comprises of weakly pinned vortices showing collective creep, crossovers to plastic creep regime [49] and sometimes a phase change from rhombic to a square lattice [50]. These changes in the structure or the dynamics of the flux line lattice give rise to a broad second magnetization peak (fish-tail effect) [49] in the $BaFe_2As_2$ based superconductors.

The magnetic phase diagram for Co-doped $BaFe_2As_2$ system [49] is shown in figure 1.11. The magnetic phase diagram clearly indicates the changes in the underlying vortex lattice from collectively pinned to weakly pinned and then finally getting unpinned giving rise to vortex liquid state prior to normal state transition. Such studies on the critical state properties and magnetic phase diagram for Ru-substituted $BaFe_2As_2$ superconductors are presented in chapter 4 and 5 of thesis.

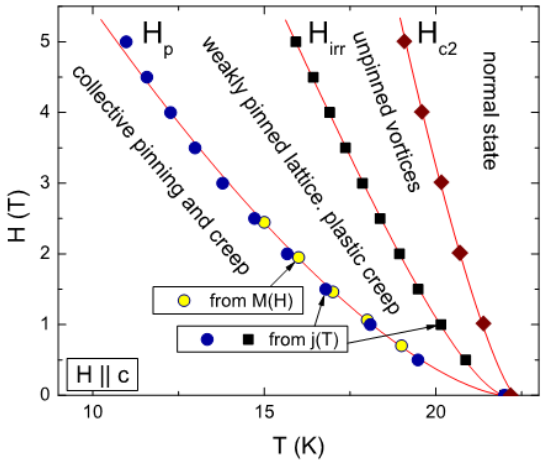

Figure 1.11: The $\mu_o H$-T vortex phase diagram of $Ba(Fe_{1-x}Co_x)_2As_2$. Figure is taken from reference [49]. Phase diagram indicates the changes in the underlying vortex lattice from collectively pinned to weakly pinned and then finally getting unpinned giving rise to vortex liquid state prior to normal state transition.

1.5 Investigations on $BaFe_{2-x}Ru_xAs_2$: Overview of the Thesis

Taking a clue from studies of various substitutions in $BaFe_2As_2$ described in section 1.3, we attempted the modification in the Fe-As bond lengths of $BaFe_2As_2$ system by isovalent substitution of Ru at the Fe site. Ru being a *4d* transition metal atom with larger ionic radius and nominally isoelectronic should only introduce changes in the crystal structure by modification of the unit cell parameters and thereby affecting the Fe-As bond lengths and $FeAs_4$ tetrahedra angles. The investigation of superconductivity by

isovalent Ru-substitution at Fe site in $BaFe_2As_2$ system [51] forms the main part of the present thesis. Detailed band structural calculations have been performed that indicate an increase in the carrier concentration due to increased hybridization of Fe *d*-bands with As *p*-bands. A *T-x* phase diagram for the $BaFe_{2-x}Ru_xAs_2$, based on the experimental results is presented in *chapter 3***.** Results of detailed structural studies for various Ru compositions, following Rietveld analysis of powder x-ray measurements, and low temperature single crystal XRD measurements, to see the correlation between the orthorhombic distortion and superconductivity in the under-doped system, are also presented in *chapter 3***.**

The growth of good quality single crystals allowed us to measure the anisotropic critical properties of the $BaFe_{2-x}Ru_xAs_2$ superconductors. The anisotropic upper critical field measurements were performed and are presented in *chapter 4.* The mass anisotropy ratio as a function of temperature for several Ru fractions is presented. Measurement of critical current density and study of flux pinning properties are presented in *chapter 5*. Based on the studies of vortex state and critical current density, a $\mu_0 H$-*T* vortex phase diagram is also proposed in *chapter 5*. In *chapter 6,* the effect of critical fluctuations on the superconducting properties of $BaFe_{2-x}Ru_xAs_2$ system has been studied, and it is shown that the fluctuations are three dimensional in character.

References

[1] Kamihara Y, Hiramatsu H, Hirano M, Kawamura R, Yanagi H, Kamiya T and Hosono H 2006 Iron-Based Layered Superconductor: LaOFeP *Journal of the American Chemical Society* **128** 10012-3

[2] Kamihara Y, Watanabe T, Hirano M and Hosono H 2008 Iron-Based Layered Superconductor $La(O_{1-x}F_x)FeAs$ (x = 0.05−0.12) with T_C = 26 K *Journal of the American Chemical Society* **130** 3296-7

[3] Takahashi H, Igawa K, Arii K, Kamihara Y, Hirano M and Hosono H 2008 Superconductivity at 43 K in an iron-based layered compound $LaO_{1-x}F_xFeAs$ *Nature* **453** 376-8

[4] Cao W, Linjun L, Shun C, Zengwei Z, Zhi R, Yuke L, Yuetao W, Xiao L, Yongkang L, Shuai J, Xiangfan X, Guanghan C and Zhu'an X 2008 Thorium-doping–induced superconductivity up to 56 K in $Gd_{1-x}h_xFeAsO$ *EPL (Europhysics Letters)* **83** 67006

[5] Mazin I I 2010 Superconductivity gets an iron boost *Nature* **464** 183-6

[6] Johnston D 2010 The puzzle of high temperature superconductivity in layered iron pnictides and chalcogenides *Advances in Physics* **59** 803-1061

[7] Mizuguchi Y and Takano Y Review of Fe Chalcogenides as the Simplest Fe-Based Superconductor *Journal of the Physical Society of Japan* **79** 102001

[8] Pfisterer M and Nagorsen G 1983 *Z. Naturforsch. B : J. Chem. Sci.* **38** 811

[9] Mandrus D, Sefat A S, McGuire M A and Sales B C 2010 Materials Chemistry of $BaFe_2As_2$: A Model Platform for Unconventional Superconductivity *Chemistry of Materials* **22** 715-23

[10] Rotter M, Tegel M, Johrendt D, Schellenberg I, Hermes W and Pöttgen R 2008 Spin-density-wave anomaly at 140 K in the ternary iron arsenide $BaFe_2As_2$ *Physical Review B* **78** 020503

[11] Wilson S D, Yamani Z, Rotundu C R, Freelon B, Bourret-Courchesne E and Birgeneau R J 2009 Neutron diffraction study of the magnetic and structural phase transitions in $BaFe_2As_2$ *Physical Review B* **79** 184519

[12] Canfield P C and Bud'ko S L 2010 FeAs-Based Superconductivity: A Case Study of the Effects of Transition Metal Doping on $BaFe_2As_2$ *Annual Review of Condensed Matter Physics* **1** 27-50

[13] Sefat A S, McGuire M A, Jin R, Sales B C, Mandrus D, Ronning F, Bauer E D and Mozharivskyj Y 2009 Structure and anisotropic properties of $BaFe_{2-x}Ni_xAs_2$ (x=0, 1, and 2) single crystals *Physical Review B* **79** 094508

[14] Huang Q, Qiu Y, Bao W, Green M A, Lynn J W, Gasparovic Y C, Wu T, Wu G and Chen X H 2008 Neutron-Diffraction Measurements of Magnetic Order and a Structural Transition in the Parent $BaFe_2As_2$ Compound of FeAs-Based High-Temperature Superconductors *Physical Review Letters* **101** 257003

[15] Wang X F, Wu T, Wu G, Chen H, Xie Y L, Ying J J, Yan Y J, Liu R H and Chen X H 2009 Anisotropy in the Electrical Resistivity and Susceptibility of Superconducting $BaFe_2As_2$ Single Crystals *Physical Review Letters* **102** 117005

[16] Su Y, Link P, Schneidewind A, Wolf T, Adelmann P, Xiao Y, Meven M, Mittal R, Rotter M, Johrendt D, Brueckel T and Loewenhaupt M 2009 Antiferromagnetic ordering and structural phase transition in $BaFe_2As_2$ with Sn incorporated from the growth flux *Physical Review B* **79** 064504

[17] Johannes M D and Mazin I I 2009 Microscopic origin of magnetism and magnetic interactions in ferropnictides *Physical Review B* **79** 220510

[18] Singh D J 2008 Electronic structure and doping in $BaFe_2As_2$ and LiFeAs: Density functional calculations *Physical Review B* **78** 094511

[19] Mikhail V S 2008 High-temperature superconductivity in iron-based layered iron compounds *Physics-Uspekhi* **51** 1201

[20] Mizuguchi Y, Hara Y, Deguchi K, Tsuda S, Yamaguchi T, Takeda K, Kotegawa H, Tou H and Takano Y 2010 Anion height dependence of T_C for the Fe-based superconductor *Superconductor Science and Technology* **23** 054013

[21] Fink J, Thirupathaiah S, Ovsyannikov R, Dürr H A, Follath R, Huang Y, de Jong S, Golden M S, Zhang Y-Z, Jeschke H O, Valentí R, Felser C, Dastjani Farahani S, Rotter M and Johrendt D 2009 Electronic structure studies of $BaFe_2As_2$ by angle-resolved photoemission spectroscopy *Physical Review B* **79** 155118

[22] Kondo T, Fernandes R M, Khasanov R, Liu C, Palczewski A D, Ni N, Shi M, Bostwick A, Rotenberg E, Schmalian J, Bud'ko S L, Canfield P C and Kaminski A 2010 Unexpected Fermi-surface nesting in the pnictide parent compounds $BaFe_2As_2$ and $CaFe_2As_2$ revealed by angle-resolved photoemission spectroscopy *Physical Review B* **81** 060507

[23] Mazin I I, Singh D J, Johannes M D and Du M H 2008 Unconventional Superconductivity with a Sign Reversal in the Order Parameter of $LaFeAsO_{1-x}F_x$ *Physical Review Letters* **101** 057003

[24] Awadhesh M and *et al.* 2009 Pressure-induced superconductivity in $BaFe_2As_2$ single crystal *EPL (Europhysics Letters)* **87** 17004

[25] Yin Z P, Haule K and Kotliar G 2011 Magnetism and charge dynamics in iron pnictides *Nat Phys* **7** 294-7

[26] Richard P, Nakayama K, Sato T, Neupane M, Xu Y M, Bowen J H, Chen G F, Luo J L, Wang N L, Dai X, Fang Z, Ding H and Takahashi T 2010 Observation of Dirac Cone Electronic Dispersion in $BaFe_2As_2$ *Physical Review Letters* **104** 137001

[27] Rotter M, Tegel M and Johrendt D 2008 Superconductivity at 38 K in the Iron Arsenide $Ba_{1-x}K_xFe_2As_2$ *Physical Review Letters* **101** 107006

[28] Ni N, Bud'ko S L, Kreyssig A, Nandi S, Rustan G E, Goldman A I, Gupta S, Corbett J D, Kracher A and Canfield P C 2008 Anisotropic thermodynamic and transport properties of single-crystalline $Ba_{1-x}K_xFe_2As_2$ (x=0 and 0.45) *Physical Review B* **78** 014507

[29] Huiqian L, Zhaosheng W, Huan Y, Peng C, Xiyu Z and Hai-Hu W 2008 Growth and characterization of $A_{1-x}K_xFe_2As_2$ (A = Ba, Sr) single crystals with x = 0–0.4 *Superconductor Science and Technology* **21** 125014

[30] Patricia L A, Ko Y T C, Jack G, Chiara M P, Jacqueline M C, Gilbert G L and Suchitra E S 2009 Superconductivity Up To 29 K in $SrFe_2As_2$ and $BaFe_2As_2$ at High Pressures *Journal of Physics: Condensed Matter* **21** 012208

[31] Fukazawa H, Takeshita N, Yamazaki T, Kondo K, Hirayama K, Kohori Y, Miyazawa K, Kito H, Eisaki H and Iyo A 2008 Suppression of Magnetic Order by Pressure in $BaFe_2As_2$ *Journal of the Physical Society of Japan* **77** 105004

[32] Klintberg L E, Goh S K, Kasahara S, Nakai Y, Ishida K, Sutherland M, Shibauchi T, Matsuda Y and Terashima T 2010 Chemical Pressure and Physical Pressure in $BaFe_2(As_{1-x}P_x)_2$ *Journal of the Physical Society of Japan* **79** 12

[33] Torikachvili M S, Bud'ko S L, Ni N, Canfield P C and Hannahs S T 2009 Effect of pressure on transport and magnetotransport properties in $CaFe_2As_2$ single crystals *Physical Review B* **80** 014521

[34] Sefat A S, Jin R, McGuire M A, Sales B C, Singh D J and Mandrus D 2008 Superconductivity at 22 K in Co-Doped $BaFe_2As_2$ Crystals *Physical Review Letters* **101** 117004

[35] Pratt D K, Tian W, Kreyssig A, Zarestky J L, Nandi S, Ni N, Bud'ko S L, Canfield P C, Goldman A I and McQueeney R J 2009 Coexistence of Competing Antiferromagnetic and Superconducting Phases in the Underdoped $Ba(Fe_{0.953}Co_{0.047})_2As_2$ Compound Using X-ray and Neutron Scattering Techniques *Physical Review Letters* **103** 087001

[36] Ni N, Thaler A, Yan J Q, Kracher A, Colombier E, Bud'Ko S L, Canfield P C and Hannahs S T 2010 Temperature Versus Doping Phase Diagrams For $Ba(Fe_{1-x}TM_x)_2As_2$(TM=Ni,Cu,Cu/Co) Single Crystals *Physical Review B* **82** 24519

[37] Ni N, Thaler A, Kracher A, Yan J Q, Bud'ko S L and Canfield P C 2009 Phase diagrams of $Ba(Fe_{1-x}TM_x)_2As_2$ (*TM* = Rh, Pd) single crystals. In: *ArXiv e-prints*, p 4894

[38] Sefat A S, Singh D J, VanBebber L H, Mozharivskyj Y, McGuire M A, Jin R, Sales B C, Keppens V and Mandrus D 2009 Absence of superconductivity in hole-doped $BaFe_{2-x}Cr_xAs_2$ single crystals *Physical Review B* **79** 224524

[39] Canfield P C, Bud'ko S L, Ni N, Yan J Q and Kracher A 2009 Decoupling of the superconducting and magnetic/structural phase transitions in electron-doped $BaFe_2As_2$ *Physical Review B* **80** 060501

[40] Shuai J and *et al.* 2009 Superconductivity up to 30 K in the vicinity of the quantum critical point in $BaFe_2(As_{1-x}P_x)_2$ *Journal of Physics: Condensed Matter* **21** 382203

[41] Kasahara S, Shibauchi T, Hashimoto K, Ikada K, Tonegawa S, Okazaki R, Shishido H, Ikeda H, Takeya H, Hirata K, Terashima T and Matsuda Y 2010 Evolution from non-Fermi- to Fermi-liquid transport via isovalent doping in $BaFe_2(As_{1-x}P_x)_2$ superconductors *Physical Review B* **81** 184519

[42] Kimber S A J, Kreyssig A, Zhang Y-Z, Jeschke H O, Valenti R, Yokaichiya F, Colombier E, Yan J, Hansen T C, Chatterji T, McQueeney R J, Canfield P C, Goldman A I and Argyriou D N 2009 Similarities between structural distortions under pressure and chemical doping in superconducting $BaFe_2As_2$ *Nat Mater* **8** 471-5

[43] Rotter M, Hieke C and Johrendt D 2010 Different response of the crystal structure to isoelectronic doping in $BaFe_2(As_{1-x}P_x)_2$ and $(Ba_{1-x}Sr_x)Fe_2As_2$ *Physical Review B* **82** 14513

[44] Sun D L, Liu Y and Lin C T 2009 Comparative study of upper critical field H_{C2} and second magnetization peak H_{SP} in hole- and electron-doped $BaFe_2As_2$ superconductor *Physical Review B* **80** 144515

[45] Tanatar M A, Ni N, Martin C, Gordon R T, Kim H, Kogan V G, Samolyuk G D, Bud'ko S L, Canfield P C and Prozorov R 2009 Anisotropy of the iron pnictide superconductor $Ba(Fe_{1-x}Co_x)_2As_2$ (x=0.074, T_C=23 K) *Physical Review B* **79** 094507

[46] Tanatar M A, Ni N, Bud'ko S L, Canfield P C and Prozorov R 2010 Field-dependent transport critical current in single crystals of $Ba(Fe_{1-x}TM_x)_2As_2$ (*TM* = Co, Ni) superconductors *Superconductor Science Technology* **23** 4002

[47] Taen T, Nakajima Y, Tamegai T and Kitamura H 2012 Enhancement of critical current density and vortex activation energy in proton-irradiated Co-doped $BaFe_2As_2$ *Physical Review B* **86** 094527

[48] Yanwei M, Chao Y, Xianping Z, He L, Dongliang W, Matsumoto A, Kumakura H, Tsuchiya Y, Sun Y and Tamegai T 2013 Large transport critical currents and magneto-optical imaging of textured $Sr_{1-x}K_xFe_2As_2$ superconducting tapes *Superconductor Science and Technology* **26** 035011

[49] Prozorov R, Ni N, Tanatar M A, Kogan V G, Gordon R T, Martin C, Blomberg E C, Prommapan P, Yan J Q, Bud'ko S L and Canfield P C 2008 Vortex phase diagram of $Ba(Fe_{0.93}Co_{0.07})_2As_2$ single crystals *Physical Review B* **78** 224506

[50] Kopeliansky R, Shaulov A, Shapiro B Y, Yeshurun Y, Rosenstein B, Tu J J, Li L J, Cao G H and Xu Z A 2010 Possibility of vortex lattice structural phase transition in the superconducting pnictide $Ba(Fe_{0.925}Co_{0.075})_2As_2$ *Physical Review B* **81** 092504

[51] Sharma S, Bharathi A, Chandra S, Reddy V R, Paulraj S, Satya A T, Sastry V S, Gupta A and Sundar C S 2010 Superconductivity in Ru-substituted polycrystalline $BaFe_{2-x}Ru_xAs_2$ *Physical Review B* **81** 174512

Chapter 2

Experimental Methods

This chapter describes the sample synthesis techniques and experimental setups used in course of the thesis work. Significant efforts in employing an innovative nontoxic method of synthesis of the precursor binary arsenide powders and polycrystalline samples in a pressure locked stainless steel tube filled with ultra-high purity (UHP) argon gas were made. To synthesize single crystals, a high temperature melt growth from stoichiometric precursor powders sealed in evacuated quartz tube was employed. While the samples have been characterized in the laboratory by powder XRD, in-depth measurements on structure changes as function of Ru content were carried out using synchrotron sources at INDUS II and Petra3 beam lines, and these are discussed. In-field transport measurements up to 12 T in 4 K to 50 K temperature range were performed in a home built magneto-resistance cryostat. Hall effect on the poly-crystal samples was measured using Van der Pauw method, implemented during the course of this thesis and is explained in some detail. Magnetization measurements as function of temperature and magnetic fields up to 16 T were performed using a commercial vibrating sample magnetometer. Methodology of estimating critical current density using the ac susceptibility measurement is also discussed.

2.1 Introduction

In this chapter, we present an account of the various experimental methods used during the course of investigations on the Arsenide superconductors. These include (a) Methods to synthesize the polycrystalline and single crystalline samples of $BaFe_{2-x}Ru_xAs_2$, (b) Structural studies using the XRD setups, both the laboratory source and synchrotron facilities, and (c) Resistivity and magnetization measurements, to

evaluate the superconducting and critical properties. As a part of this work, several experimental facilities for measurements at low temperatures have been built / augmented, which are described in some detail. Mention must be made of the facility for ac susceptibility using the Vibrating Sample Magnetometer that has been used to determine the critical current density, and Hall effect measurements, that has been used to investigate the nature of carriers in the Ru doped $BaFe_2As_2$.

2.2 Polycrystalline sample preparation

The $BaFe_{2-x}Ru_xAs_2$ (x = 0.0, 0.25, 0.50, 0.75,0.875, 1.0,1.125,1.25 and 1.5) samples were prepared by solid state reaction from preformed FeAs and RuAs powders and Ba chunks, under 35 bar Ar pressure locked inside a stainless steel (SS 304) tube. A schematic sketch of the setup is shown in figure 2.1. To keep the synthesis process free from the hazards of free arsenic contamination and also for the ease of reaction, all the compounds were synthesized using FeAs and RuAs as the precursors [1] along with Ba chunks. Synthesis of RuAs precursor powder was a crucial step and several different heat treatments were tried to obtain phase pure RuAs. For the synthesis of FeAs and RuAs, stoichiometric Fe/Ru and As powders were ground thoroughly and filled in quartz crucibles. The powders in the quartz crucibles were then heat treated up to 800^{o}C under the 35 bar UHP Ar in the setup [2] shown in Fig. 2.1.

After loading the sample (5) into the sample space (1), the high pressure fitting was tightened with a sealing Teflon tape. The setup was then flushed with high purity argon gas through the pressure lock valve by connecting the setup to a vacuum system and finally 35 bars of 99.999% UHP Ar gas was locked-in. The pressure was seen to

remain without leakage for several hours at room temperature. In order to prevent the oxidation of the SS tube at the reaction temperature ~ 800 ^{o}C, the setup was clamped into a quartz tube (6) with a Wilson seal (7) through a T-joint. The quartz tube was evacuated to ~10^{-3} Torr using rotary pump. The quartz tube containing the SS tube assembly was inserted into a vertical tubular furnace (9) which was programmed according to the temperature profile required for the synthesis. During the heat treatment, the quartz tube was constantly pumped to avoid any oxidation of SS tube. The pressure inside the sample space was seen to rise to ~ 50 bar and remains constant throughout the reaction time. This prevented any As vapor from coming out of the setup. At the end of the reaction schedule, the setup was removed from the furnace and cooled to room temperature. During this time the pressure inside falls back to ~35 bar. The precursor powders were retrieved by opening the ferrule coupling and were ground thoroughly. The grounded powders were weighed to check for any weight loss and then a second similar heat treatment was given to the powders. Finally the precursor FeAs/RuAs powders were ground and checked for phase formation by XRD analysis.

Following the synthesis of precursor FeAs and RuAs powders, $BaFe_{2-x}Ru_xAs_2$ samples of various compositions, were prepared by solid state reaction from preformed FeAs and RuAs powders and Ba chunks, under 35 bar UHP Ar pressure in the same setup described above. Tantalum crucibles were used for the synthesis. To obtain optimum phase purity, several different heat treatment temperatures ranging from 800 ^{o}C to 960 ^{o}C along with different annealing time and temperatures were tried. The samples were heat treated for 5 hours to 8 hours in order to find an optimum heat treatment and phase purity

was studied using X-ray diffraction at each step. The optimized heat treatment procedure is described below.

After an initial heat treatment at 960^{o} C for 8 hours, the reacted powder was ground, pelletized and sintered at 900^{o} C for 5 hours. All weighing operations and loading of the reactants into the Ta crucibles were done in a Helium filled glove box. The procedure was repeated twice with an intermediate grinding. This resulted in good grain to grain contact and hard pellets that could be used for carrying out transport and magnetization studies.

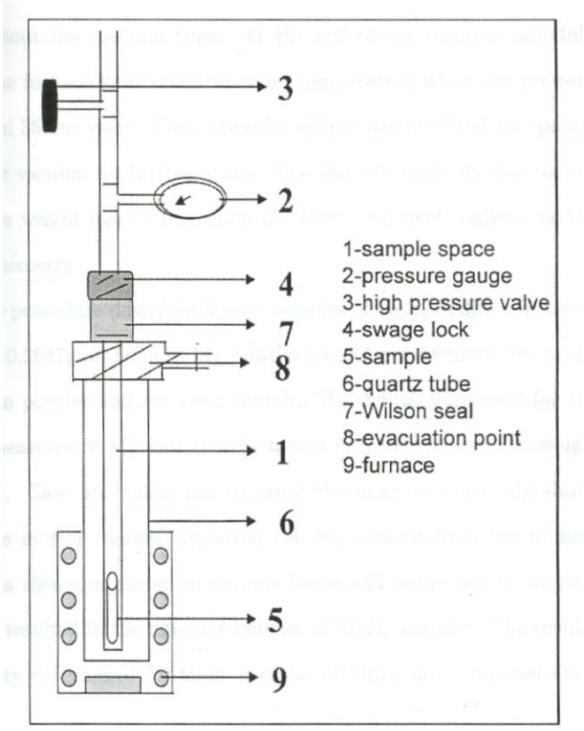

Figure 2.1: Schematic of the setup to lock 50 bar of ultra-high purity argon gas is shown. The setup was made from *SS-304* tube having 1/2 inch diameter with 1.6-2 mm wall thickness. The bottom of the tube was closed using a SS plug, welded to it. To the upper part of the setup was attached a pressure gauge (2) and a high pressure valve (3) which was used to lock-in the pressure. The upper part containing pressure gauge along with pressure lock valve and the lower parts consisting of sample (5) inside the SS tube were connected using ferrule fitting (4) which was closed and opened during the loading and unloading of the sample.

2.3 Single crystal growth

After the successful synthesis of the polycrystalline samples of Ru-substituted $BaFe_2As_2$, growth of single crystals of these compounds was carried out by high temperature melt growth technique. The single crystalline samples helped us in measurements of anisotropic critical properties of these superconductors, described in Chapters 4 and 5. Figure 2.2 show photograph of a few of the $BaFe_{2-x}Ru_xAs_2$ single crystals. The typical dimensions of crystals are 2 mm x 2 mm.

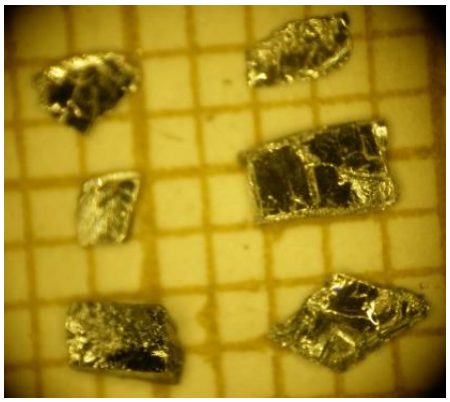

Figure 2.2: Photograph of cleaved $BaFe_{2-x}Ru_xAs_2$ single crystals grown by high temperature melt growth technique. The crystals are c-axis oriented, shiny plate like and layered. Typical dimension of as grown crystals are ~ 2 mm x 2 mm and around 1-2 mm thick.

For the growth of single crystals, using the high temperature melt growth process, initially, indium or excess FeAs were used as flux but in both the cases retrieval of crystals from the solidified flux was difficult. To avoid problems associated with the excess flux growth. Ru-substituted single crystals were grown by slow cooling of the high temperature melt of stoichiometric precursors. In the following, we enumerate the crucial steps in the growth of single crystals.

1) FeAs, RuAs powders along with Ba chunks were weighed in the stoichiometric ratio and filled in high purity alumina crucibles. The FeAs and RuAs powders were thoroughly ground and mixed well using a mortar and pestle.
2) Prior to the use, the high purity alumina crucibles were baked at 500^{o} C for 5 hours to remove any moisture from them. The baked crucibles were not touched by bare hands and all the operations were then performed in glove box containing dry ultra-high pure helium gas.
3) The mixtures of FeAs, RuAs and Ba chunks were then filled in the baked alumina crucibles and were sealed inside a baked quartz ampule. The quartz ampule was flushed three times with UHP argon gas. The crucible was covered with cotton wool to avoid heating the precursors while sealing the quartz tube.
4) The quartz ampules containing alumina crucibles having precursor powders were then kept for heat treatment. Initially the precursors were slowly heated to 1190^{o} C at nearly 50^{o} C per hour. Then the ampule was kept at 1190^{o}C for 24 hours, for the homogenization of the melt.
5) The furnace temperature was then slowly lowered at a rate of around 1-1.5^{o} C per hour up to 1000^{o} C. After that the furnace was cooled at 50^{o} C per hour till room temperature.

The above process resulted in shiny, plate like flat single crystals (Fig. 2.2) without impurities. Even though the size of the crystals grown by the flux-free method are smaller, they are much more pure then what we could synthesize using excess flux.

2.4 X-ray diffraction measurements

All the samples used in the experimental studies that form a part of the present thesis were characterized for the phase purity using powder XRD patterns. The initial characterization of polycrystalline samples and single crystals was performed using a STOE diffractometer operated with a power of 40 kV and 30 mA, in the Bragg-Brentano geometry. The X-ray radiation used was the $Cu-K_{\alpha}$ line. The lattice parameters from XRD pattern have been extracted using STOE and PCW programs. A typical powder XRD pattern for the $BaFe_{1.5}Ru_{0.5}As_2$ sample is shown in figure 2.3 (a).

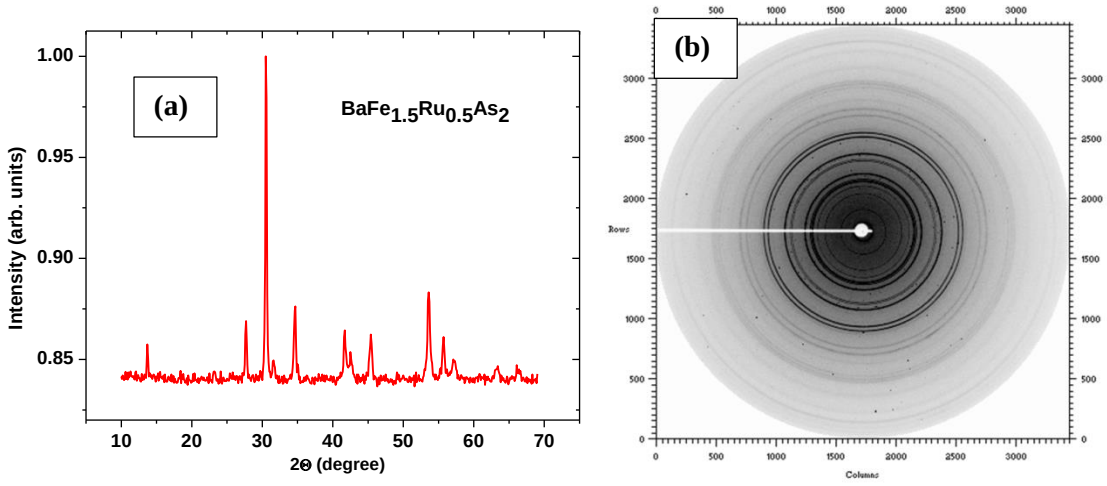

Figure 2.3 (a): A typical powder XRD pattern recorded in Bragg-Brentano geometry using *Cu K-*α line on a STOE XRD machine. **(b)** Image plate MAR3450, 2D-data collected using Debye Scherrer geometry at INDUS II ADXRD beam line. Fit2D program is used to convert 2D data to I vs. 2θ plots.

To get high quality diffraction data for performing Rietveld structural refinement, XRD data were recorded using BL-12 ADXRD beam line at INDUS-II synchrotron source at RRCAT, Indore India. The XRD patterns were recorded on a MAR3450 image plate and the sample was mounted in Debye-Scherrer geometry. The 2D ring pattern (

See Fig. 2.3b) recorded on the image plate was converted to the 2θ versus intensity (I) plots using FIT2D program [3]. The Rietveld analysis was performed using GSAS program [4].

Low temperature HRXRD measurements on the single crystals of under- doped $BaFe_{2-x}Ru_xAs_2$ samples were performed to see the correlation between the superconductivity and orthorhombic distortion in the system, as described in Chapter 3. Investigations on the phase transition from the high temperature tetragonal to low temperature orthorhombic structure in the under-doped single crystals were carried out using the P08 beam line at PETRA -3 synchrotron source, Hamburg, Germany.

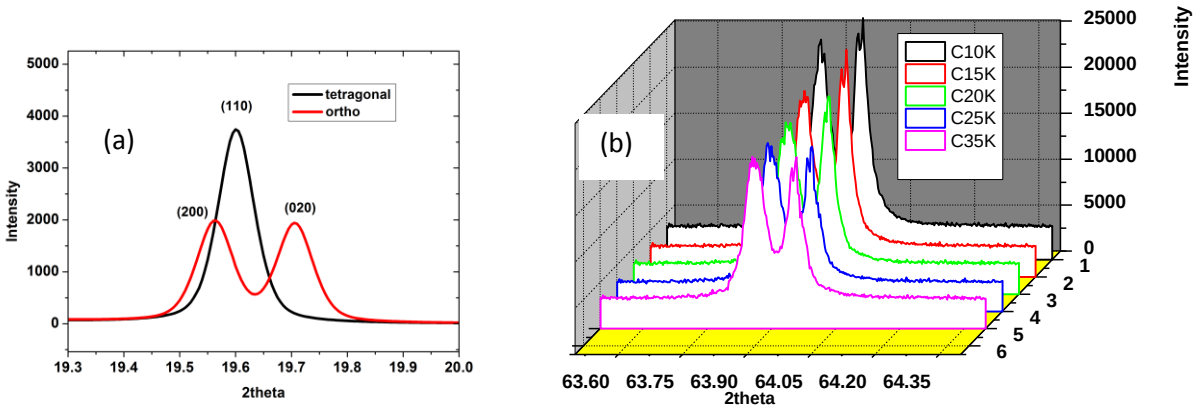

Figure 2.4 (a): Upon cooling the $BaFe_{2-x}Ru_xAs_2$ sample below the SDW transition temperature (1, 1, 0) line of tetragonal crystals symmetry (I4/mmm) splits into two lines: (2, 0, 0) and (0, 2, 0) for the orthorhombic (Fmmm) crystal symmetry. **(b)** HRXRD data in the orthorhombic phase collected at different temperatures. These data are used to evaluate the evolution of the orthorhombic distortion at low temperatures (For details: See Chapter 3)

The tetragonal to orthorhombic structural phase transition in this system (see Chapter 1) was tracked by following the splitting of (1, 1, 0) line of tetragonal phase (I4/mmm) as a function of sample temperature from room temperature to 10 K (See Fig, 2.4) . A helijet cryostat was used to control the sample temperature and Mythen line

detector with 0.003º/step angle resolution was employed to record intensity data. At the tetragonal to orthorhombic phase transition, the (1, 1, 0) line splits into two (2, 0, 0), (0, 2, 0) lines of orthorhombic phase (Fmmm symmetry). These (2, 0, 0) and (0, 2, 0) lines were fitted to multiple Lorentzian to estimate the '*a*' and '*b*' lattice parameters that can finally give the degree of orthorhombic distortion $\delta = (a-b)/(a+b)$. These results are discussed in Chapter 3.

2.5 Low temperature resistivity measurements

Figure 2.5 shows the low temperature resistivity set-up that was used during the course of these investigations. The samples are mounted on oxygen free high conductivity (OFHC) copper platform (See Fig 2.5b) on which a pre-calibrated silicon diode sensor is firmly attached using GE-varnish for monitoring the temperature.

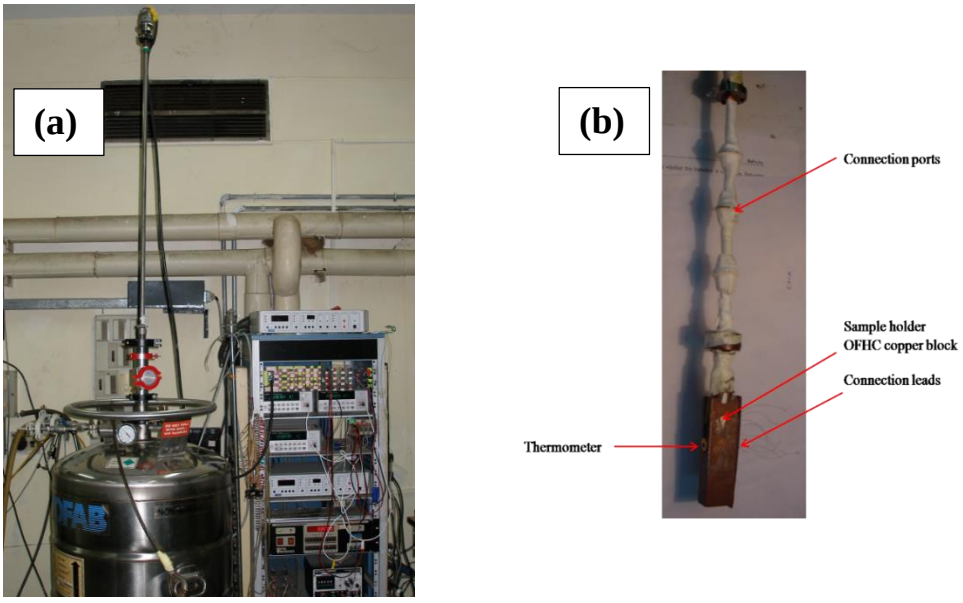

Figure-2.5 (a): Photograph of resistivity measurement setup showing dipstick inserted inside the liquid helium storage Dewar. Instrument rack contains current sources and nano-voltmeters. The sample holder part of the dipstick is shown in photographs **(b).** At a time, resistivity of four samples can be measured using this setup.

The sample of known, uniform thickness (t ~ 1 mm), is attached using GE varnish or sticky tape to the OFHC copper platform. The sample remains electrically insulated from the Cu block due to tape and the GE varnish. To avoid any thermal gradients between thermometer and sample, the samples are attached to the Cu block exactly at the back of the diode temperature sensor. The resistance of the samples is measured in four probe Van-der Pauw [5] configuration (shown in figure 2.6) using Cu wires (38 SWG) which are attached to the sample using silver filled epoxy. The leads of the sensor and the sample are soldered onto a connector pad, from which connections to the corresponding current sources and nano-voltmeters are made. The temperature variation of 300 K to 4.2 K is achieved by inserting the dipstick mounted with the sample and sensor into a liquid helium storage Dewar. The samples are cooled making use of the natural thermal gradient of the Dewar. During the insertion of the dipstick, data from the sample and the sensor are simultaneously collected using a LabView program through GPIB interface with a computer. The sequence of data acquisition is as follows. Initially a known minimal current (I) is passed through the sample leads using a DC current source. The Si diode is activated with 10 μA current with another similar current source. The nano-voltmeters, reading the voltages from temperature sensor and samples, are triggered simultaneously using a bus command over GPIB interface. This helps in synchronized reading of resistance at each corresponding temperature without any delay between the two. The meters start collecting data into their volatile memory according to a preconfigured set of parameters like number of readings, channels to be read and offset values. The voltage readings that are stored in the volatile memory of the meters are then read into the computer over the GPIB interface. The sensor voltage is then converted into the

temperature from a set of pre-calibrated Chebyshev polynomial coefficients. Since the voltage leads from sample see a temperature gradient from the room temperature to the sample temperature, the voltage across sample always contains thermo-emf added to it. To remove the thermo-emf, voltages are read with both forward (I^+) and reversed currents (I^-) separately and are then subtracted from one another. From these voltage values the sample resistance is determined as $R_S = V_S / I_S$ where $V_S = V_S^{I+} - V_S^{I-}$. This process of data acquisition is repeated after a small delay of about 1-2 seconds while the dipstick is slowly inserted into the liquid helium Dewar to achieve the temperature variation from 300 K to 4.2 K. After each data collection at a given temperature, the values of temperature and resistance are written onto a file and stored for further analysis. The measurement is generally repeated in the warming run by raising the dipstick and repeatable data could be obtained as in the cooling run, by the slow movement of the dip-stick and ensuring good contacts were made on the samples. The procedure that was adopted to determine the room temperature Van-der Pauw resistivity is schematically described in figure 2.6.

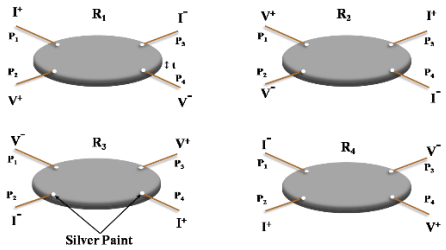

Figure 2.6: Schematic representation of the electrical contacts made using silver paint for measuring four probe Van der Pauw resistivity. Four contacts are made on the sample as shown in figure and the four resistances (R_1, R_2, R_3 and R_4) are measured on the sample by sequentially changing the current and voltage leads (P_1, P_2, P_3 and P_4). Then by substituting the pair of resistance values (R_2, R_3), (R_3, R_4) and (R_4, R_1) in place of (R_1, R_2) in the Van-der Pauw equation (1), a set of four Van-der Pauw values (ρ^1_{RT}, ρ^2_{RT}, ρ^3_{RT} *and* ρ^4_{RT}) are obtained and the average of these values is taken as the room temperature Van-der Pauw resistivity(ρ_{RT}) of the sample.

The room temperature (RT) Van-der Pauw resistivity (ρ_{RT}) is determined by iteratively solving the equation [5]

$$\exp(-\pi t R_1 / \rho_{RT}) + \exp(-\pi t R_2 / \rho_{RT}) = 1 \qquad (2.1)$$

where R_1 and R_2 are the resistance of the sample in two perpendicular configurations of current input and t, the thickness of the sample. The temperature dependent resistance on the sample is then scaled to the ρ_{RT}, by the factor ($\alpha = \rho_{RT} / R_i$) where R_i (i = 1 to 4) are the resistances at room temperature of a particular configuration.

2.5.1 Transport measurements in magnetic field

The in-field resistivity measurements across the superconducting transition are one of the several possible methods to establish $\mu_0 H$-T phase diagram of a superconductor. The upper critical fields as a function of temperature for our Ru-substituted $BaFe_2As_2$ superconducting single crystalline samples were measured in a home built magneto-resistance (MR) measurement setup. The cross sectional view of the cryostat with the magnet, schematically illustrating MR setup is shown in figure-2.7(a) and photographs of the setup and the sample holder are shown in figure-2.7(b) and figure-2.7(c) respectively. Resistivity of the samples in the temperature range from 4.2 K to 300 K and in the presence of magnetic fields up to 12 T has been measured in the magneto-resistance setup.

The cryostat used in the setup is a gas shielded, stainless steel, cryostat procured from CVE, Korea. The cryostat is having a liquid helium capacity of 30 liters and the dimensions are shown in figure-2.7(a). The superconducting magnet housed in this cryostat was procured from M/S Cryogenic Consultants ltd. and has a clear bore of 30

mm. The superconducting solenoidal magnet is capable of producing fields up to 12 T at a current of ~ 84.5 A. The magnet is mounted on a support structure and is suspended into the tail region of the cryostat. The current leads of the magnet are vapor cooled Cu leads. The sample holder assembly is placed inside sample space which is a part of the double walled exchange chamber made up of stainless steel. The exchange chamber is placed inside the 30 mm bore of the magnet. The outer region of the double walled exchange chamber is usually kept at a partial pressure (~ 8 mbar) of helium gas that serves as a thermal link to control the temperature of the sample. The inner chamber is filled with dry helium gas at a pressure of 1 bar and contains the sample holder assembly.

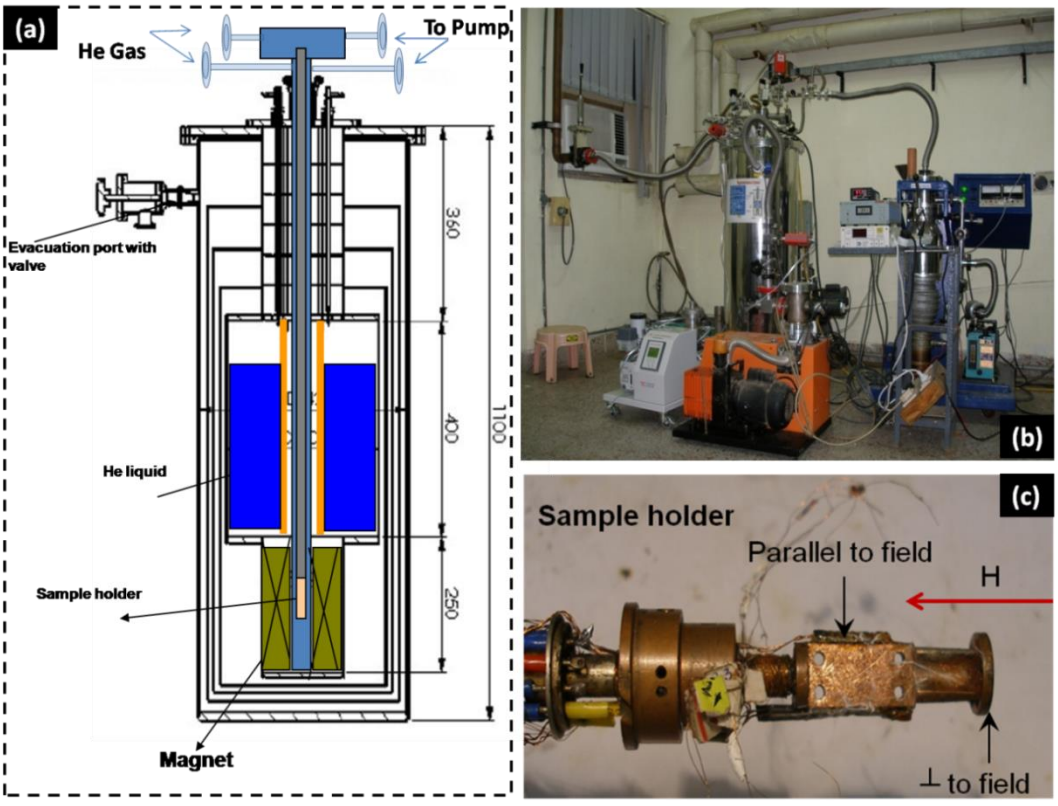

Figure 2.7: (a) Schematic **c**ross-sectional view of the Magneto-Resistance cryostat illustrating the position of SC magnet, sample holder etc. **(b)** Photograph of the MR setup **(c)** Photograph of the sample holder; showing the OFHC platforms mentioned in the text. The Red arrow indicates the direction of the magnetic field.

The desired rate of cooling and warming is achieved using a temperature controller (Oxford instruments, model ITC503) which uses 30 Ω manganin wire as heater wound around a copper shield, surrounding the sample holder. The copper shield provides a uniform temperature environment for samples. The sample holder shown in figure 2.7 (c) is made up of OFHC (Oxygen Free High thermal Conductivity) copper block attached to one end of a SS rod by brazing. The other end of SS rod is welded on to the top flange of the double wall chamber. The top flange seals the double walled exchange chamber using vacuum compatible neoprene O-rings. The current and voltage leads are thermally anchored to the SS rod at various places using GE varnish. The leads are terminated at connection ports in order to avoid the thermal gradient from ambient temperature to OFHC copper sample holder.

Initially, the cryostat and the magnet are pre-cooled, prior to liquid helium transfer. For pre-cooling, the cryostat is filled with liquid nitrogen and cooled to 12-24 hours so that the radiation shield and super-insulation cools sufficiently and reaches equilibrium. After pre-cooling, the liquid nitrogen is removed by pressurizing the cryostat with warm nitrogen gas. Once the liquid nitrogen is completely removed, the cryostat is purged with helium gas three times. After purging, liquid helium is transferred, and once the liquid helium bath is filled, the magnet is completely immersed in liquid helium.

The sample holder has three platforms; two for mounting the samples parallel to the field and one perpendicular to the field (figure-2.7(c)). For measurements parallel to the field, the sample holder can accommodate four samples with maximum size of 5 mm diameter and 1 mm thickness (figure 2.7(c)). Four samples can be mounted two on each side of the copper block. Four different set of probes each consisting of four leads are

made available to the connection pad attached to OFHC copper block to feed in the current and to measure the voltage across the four samples.

The resistance is measured by four probe technique in the Van der Pauw configuration described earlier in section 2.5. A calibrated DC current source (Time Electronics) is used to pass a fixed current (~1-10 mA) to the sample and an Agilent (model 34420A) two channel nano-voltmeter is used to measure the voltage across the sample. The block diagram of the setup for measuring the resistance of four samples simultaneously is shown in figure 2.8.

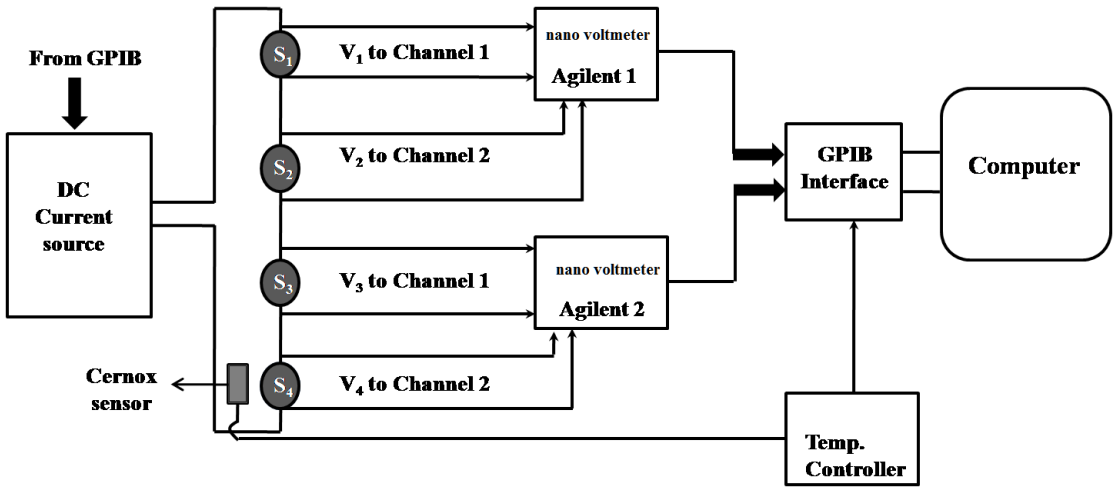

Figure 2.8: Block diagram of the set up for resistance measurement in MR setup. Four samples are connected in series with a DC current source and the voltage drop across the samples is measured using two channel Agilent nano-voltmeters.

The voltage drop across the four samples, V_1-V_4, is measured using the two channel Agilent nano-voltmeters. The temperature of the sample is measured using a pre-calibrated Cernox sensor which is known to be a good miniaturized temperature sensor at high magnetic fields. The Cernox sensor is firmly fixed at one side of the copper block, very close to the samples. The resistances of the sample during positive and negative currents are measured (in order to remove the contribution from the thermo-emf

generated in copper leads) and the averaged value is taken as the resistance at that particular temperature. Current source and Agilent voltmeters are connected to computer through GPIB interface and the data is collected onto disk after each temperature step. Figure 2.9 shows typical plots of in-field resistivity measurements on superconducting samples. The estimation of the critical fields from such measurements is discussed in detail in Chapter 4 and critical fluctuations in Chapter 6.

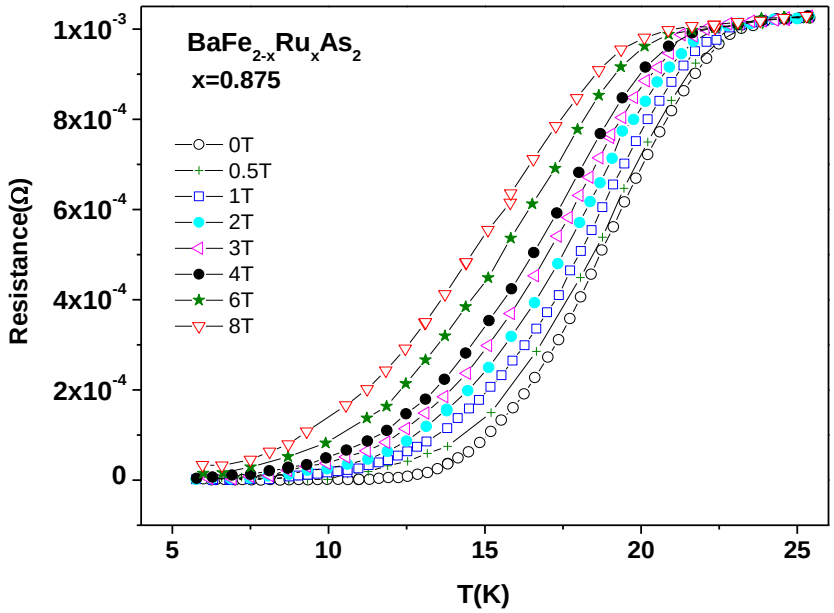

Figure 2.9: Variation of resistance versus temperature for various external magnetic fields indicated, for Ru fraction, x= 0.875 in polycrystalline $BaFe_{2-x}Ru_xAs_2$ samples. The plots shows shift in superconducting transition due to application of external field. These *R(T)* plots under different magnetic fields are used to estimate upper critical field of superconductors.

2.6 Hall effect measurements

To understand the superconducting system, knowledge of the charge carrier type in the normal state of the material is important. The Hall effect provides an easy means to determine the charge carrier density and their mobility in a material. Based upon the technique of conformal mapping of 2D fields, Van der Pauw proposed a method [5, 6] for

determining the resistivity and Hall mobility of singly connected flat samples of any arbitrary shape. In this method, the sample should be of uniform thickness and sufficiently small contacts should be made on its circumference. The Hall coefficient in our samples is measured using a home-built interface coupled to the magneto-resistance cryostat described above. The design of the Hall coefficient measurement setup, carried out as a part of the thesis work, [7] is described in detail in the following:

It is well known [8] that the Hall voltage, that is anti-symmetric in applied magnetic field, is generally accompanied by different spurious voltages depending upon the instability in temperature and other measurement conditions. Some of these error voltages are Thermoelectric voltage (V_S), Ettingshausen voltage (V_E), Nernst voltage (V_N), Righi-Leduc voltage (V_R) and contact-misalignment voltage (V_M). These voltages are symmetric either in magnetic field or current or sometimes both and this helps to discriminate them from the Hall voltage, by a combination of measurements for different field and current directions. Of all these, the misalignment voltage that arises from geometrical mismatch in voltage contacts, has the largest effect on the measurement. Whereas the V_S, V_N and V_R can be removed by combining measurements for two opposite current direction, V_M can be removed from apparent Hall voltage by combining the measurements for two opposite field directions. In addition to this, swapping the voltage and current leads helps in reducing errors due to non-uniform shape of the sample. The change of direction and electrical contacts is a burdensome process and is usually implemented using switching system.

Several methods have been proposed for measuring the Hall voltage with minimal offset voltages. Offset voltages are removed from measurements either by mathematical

manipulations of the collected data or sometimes even at the time of collection by employing special electronic instrumentation [9-11] . We adopted the switching scheme of electrical contacts and magnetic field, all automated using LabView VI and interface cards.

For the sample geometry and contacts as shown in figure 2.10 and for a given direction of field, the various electrical configurations of Hall voltage measurements are V_{1324}, V_{3142}, V_{2431}, *and* V_{4213} (hereafter named V_C, V_D, V_E, V_F). Here V_{ijkl} notation signifies that current is entering from terminal *i* and leaves from terminal *j*, while measuring voltage between terminal *k* and *l* with *k* being the positive terminal of voltmeter. Similar set of voltages are collected for other field direction also. To use the single current source and voltmeter the complete set of four voltage measurement require eight switches in all.

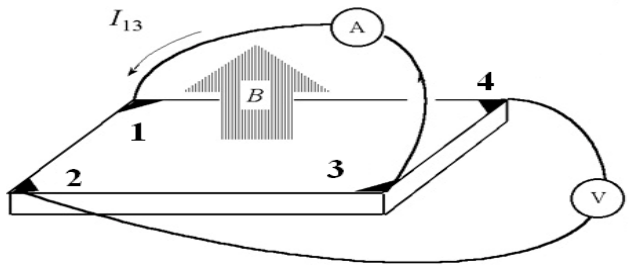

Figure 2.10: Current and voltage leads configuration for the van-der Pauw Hall coefficient measurement setup. The voltage and current leads are required to be swapped for the error free measurement of Hall voltage.

To measure the Hall effect in the normal state of our iron arsenide based superconducting samples, we have designed and implemented a computer *(PC)* controlled switching card (figure-2.11 (b)) that can connect voltmeter and current source between any of the four terminals on the sample.

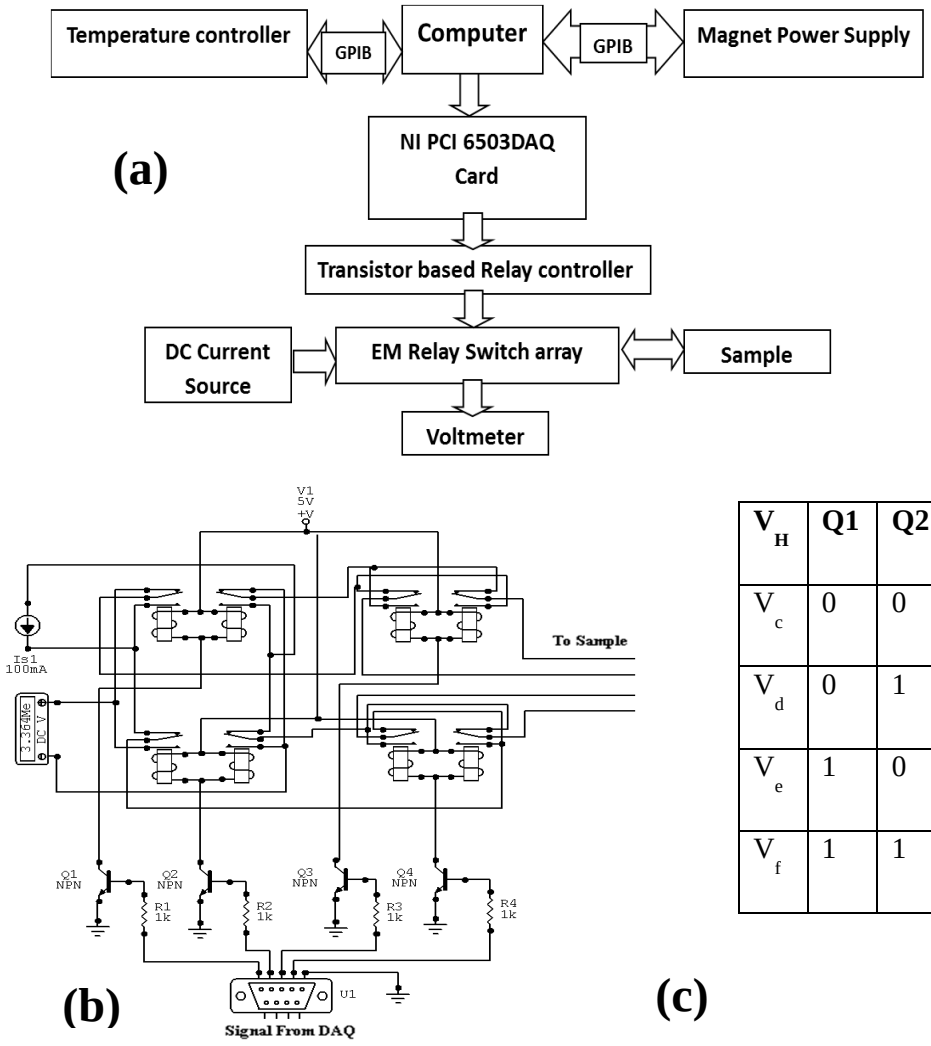

V_H	Q1	Q2	Q3	Q4
V_c	0	0	0	0
V_d	0	1	1	0
V_e	1	0	1	1
V_f	1	1	0	1

Figure 2.11: (a) The block diagram of the main hardware components and process flow used in the scheme for the measurement of Hall coefficient. All the operations are automated using the NI PCI 6503 DAQ card and GPIB interfaces. **(b)** Circuit diagram of switching card. Any of the sample terminals can be connected to the voltmeter and current source leads using the proper control logic shown in figure **(c)**

The 5 volt electromagnetic relays are used as switching elements. Each relay unit contains two NC/NO contacts, this makes their programming simpler as one needs only four driving transistors and 4 control lines for interfacing with the *PC*. To collect all the four Hall voltages in a given magnetic field direction the control logic given in figure 2.11 (c) is sent to the switching circuit using *NI PCI 6503* DAQ card which has three

8-bit ports. The block diagram of the main hardware components and process flow is shown in figure-2.11(a).

The switching card is programmed in LabView to select the proper current direction through sample and it connects the voltmeter to the sample such that irrespective of the current direction, the Hall voltage measured is always positive for one magnetic field direction and negative for the other. The samples are mounted perpendicular to the field direction in our 12 T magneto-resistance cryostat. The reversal of the magnetic field direction is achieved by magnet power supply and the sample temperature is controlled using Oxford make *ITC503* temperature controller. The magnet power supply and the temperature controller are GPIB controlled through the same LabView VI.

The Hall voltage and R_H are estimated by averaging the voltages collected for all current configurations and field directions. For averaging, the voltages are used with proper sign as measured in the experiment. The Hall coefficient is then calculated using the equation,

$$R_H = \frac{V_H * d}{B * I} \qquad (2.2)$$

Where, V_H is the Hall Voltage, B is magnetic field in Tesla, d is sample thickness in m, and I is excitation current in Amperes.

To validate the experimental setup and measurement protocol, Hall coefficient measurements were performed on YBCO and $(Ba_{1-x}K_x)Fe_2As_2$ polycrystalline superconductor samples and also in high purity Ge single crystal. The plots of

temperature variation of Hall coefficient with temperature for $Ba_{1-x}K_xFe_2As_2$ (x = 0.41 and 0.47) superconductors [7] is shown in figure 2.12. The value of Hall coefficient and its temperature dependence for $Ba_{1-x}K_xFe_2As_2$ [12] and all other materials also was found to be similar to the values reported and thus the setup after been tested for satisfactory working was used to measure Hall coefficient as a function of temperature for Ru-substituted $BaFe_2As_2$ polycrystalline samples described in section 3.4.

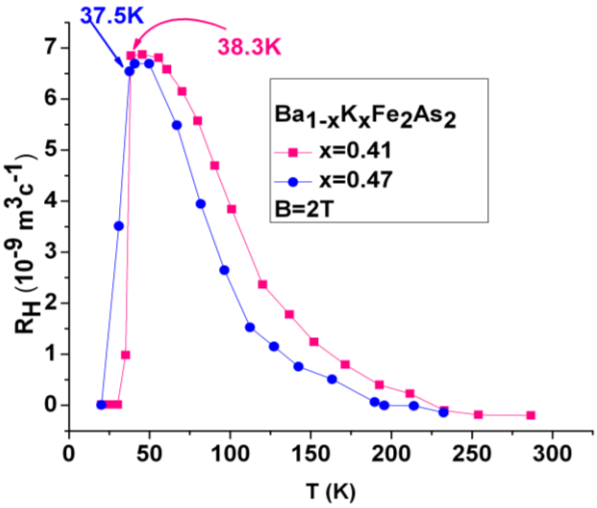

Figure 2.12: Hall coefficient variation as a function of temperature for two different K doped $BaFe_2As_2$ samples. The K substitution for Ba, dopes holes in the system and thus the value of the Hall coefficient is positive in whole temperature range. The Hall coefficient is temperature dependent due to multiband nature of the compound.

2.7 Vibrating sample magnetometer

During the course of the work presented in the thesis, magnetization and AC susceptibility measurements were performed extensively for establishing the occurrence of bulk superconductivity and to study the critical current density along with vortex state of Ru-substituted superconductors. The magnetization measurements were performed in 16 T liquid helium based Vibrating Sample Magnetometer (VSM) [5], shown in Fig.

2.13. The schematic diagram of the cryostat is shown in figure 2.14(a). The cryostat has a single vacuum insulated chamber that contains one inner helium reservoir of ~ 100 liters capacity and an outer liquid nitrogen jacket of ~ 90 liters capacity. The cryostat is fitted with high purity aluminum radiation shield that helps in minimizing the temperature gradients to reduce the helium boil off. The radiation shields are surrounded by a super-insulation blanket of alternative layers of reflective aluminized-mylar and nylon netting. This helps in further reducing the radiation load. The helium evaporation rate is typically ~ 400 cc / hour.

Figure 2.13: Photograph of M/S Cryogenic Inc., U.K. make VSM; Inset shows the sample mounted inside a straw with the help of non-magnetic kapton tape. The straw is attached to the vibrating rod with the help of kapton tape.

The superconducting magnet is a vertically oriented hybrid solenoid wound from copper stabilized filamentary superconducting wire of NbTi with Nb_3Sn. The magnet has an inductance of 55.5 Henry and the maximum operational field is 16 T with central field

homogeneity of 0.01% over 40 mm. The magnet is powered using a power supply (Cryogenic; Model SMS120C), with maximum current 120 A and voltage ±5 V. The electrical access to the magnet is via High Temperature Superconducting current leads that terminate on the cryostat top plate. The magnet is cooled by liquid helium through tubes wound along with the magnet from the bottom of the liquid helium reservoir (figure 2.14 (a)). The magnet is fitted with carbon resistor thermometers in the inner and outer layers so that the temperatures are monitored continuously during the cool down and normal VSM operation. The thermometers are constantly monitored for the any loss of liquid helium and thus saves magnet from any potential damage.

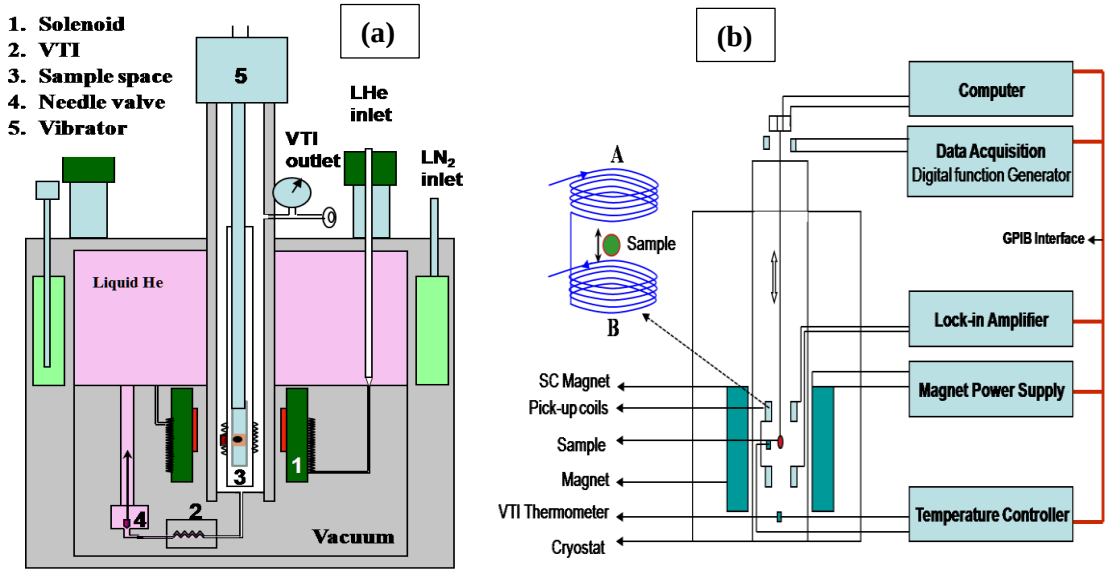

Figure-2.14 (a): Schematic diagram VSM cryostat and instruments. The helium vessel is indicated in pink color, the outer liquid nitrogen vessel is shaded as green and the surrounding portions are kept in vacuum. **(b):** Block diagram of vibrating sample magnetometer. The schematic picture of the pick-up coil and the sample is shown separately.

The cryostat contains a variable temperature insert (VTI) to operate in the temperature range of 1.6-325 K. The VTI has an internal diameter of 25 mm and is fitted inside the central bore of the magnet. The bottom of VTI tube is fitted with a Cernox

thermometer and a heater. At the bottom, the VTI is connected to a helium reservoir through a small capillary tube and the helium pot is connected to the helium reservoir through a needle valve (see figure 2.14 (a)). The needle valve is adjusted manually to control the flow of liquid He to the pot. Once the needle valve is set (usually for 5-15 mbar at the VTI circuit) the temperature of the VTI is controlled by controlling the heater power at the VTI bottom by a *LakeShore (Model 340)* temperature controller. The helium gas from the helium pot through the VTI circuit is driven back to the helium recovery line through an oil-free rotary vacuum pump, connected to the VTI outlet (see figure-2.14 (a)).

The sample is loaded inside the sample chamber, is in thermal contact with the VTI via static helium exchange gas. The sample chamber has an internal diameter of 14 mm, and the temperature of the sample is monitored by a Cernox thermometer located on the sense coils, close to the sample. Temperature is controlled using a heater wound across the pick-up coil by the *LakeShore* temperature controller.

At the heart of the VSM sits a small vibrator that provides the sinusoidal vertical motion of the sample within the pickup coils. Typically the vibrator runs at 20.4Hz and 1 mm peak to peak amplitude. Inside the vibrator, a small permanent magnet is mounted on the driving rod which vibrates near a reference coil. The voltage generated in the coil is constantly monitored by a LabView program to control the amplitude and offset of the vibration using a feedback circuit with a PID loop. The sample is positioned correctly in the pickup coils with the help of stepper motors by means of a ball screw attached to the motor's shaft which enables precise up and down movement of the sample holder over a vertical range of 100 mm.

2.7.1 Experimentation using the VSM

The vacuum space of the VSM is pumped down to 10^{-3} torr before cool down. The cryostat is first pre-cooled with liquid nitrogen, before cooling with liquid helium. For pre-cooling the cryostat is filled with liquid nitrogen and kept cold for 12-24 hours so that the radiation shields and super-insulation cool sufficiently and reach equilibrium. The liquid nitrogen is then removed by pressurizing the cryostat with warm nitrogen gas. Any residual liquid nitrogen on the base of helium reservoir can be removed completely by boiling it off with the heater mounted at the base of the reservoir. Once the liquid nitrogen is completely removed, the cryostat is purged with helium gas three times. After the purging, liquid helium is transferred. As the liquid helium is transferred, the base temperature of the helium reservoir starts to fall and once the temperature reaches 4.2 K, liquid starts to collect and at this stage, the helium transfer rate is increased. The magnet and VTI are cooled with helium through the separate capillary tubes from the helium reservoir (see figure 2.14). The helium level is measured using helium level gauge fitted inside the reservoir. Once the cooling procedure is over, the sample can be loaded for the measurement.

The sample is mounted on non-magnetic plastic straw and attached to the lower end of a rigid rod (see inset of the figure-2.13) which is made to oscillate vertically, typically over 1 mm at a frequency of 20.4 Hz. If the sample is magnetic in response to an external applied field, the oscillation will induce an AC signal in a set of suitably placed pick-up or sense coils (see figure-2.14). The amplitude of this signal is proportional to the magnetic moment of the sample. The pick-up signal is fed to the lock-in amplifier (LIA) which is tuned to lock the signal precisely at the sample's vibration

frequency using a reference signal from the vibrator control. Thus, LIA detects the in-phase voltage from the pick-up coils. The vibration amplitude is controlled by PID controlled feedback circuit. It maintains the vibration amplitude at approximately ±1 mm about the optical center, correcting for changes in temperature, pressure and load in the sample chamber. The pick-up coils are matched and connected in opposite sense. The pick-up coil is wound in such a way that, an external field (a constant field, traversing uniformly through both set of coils A and B) would induce equal and opposite voltages in the two sets of pick up coils, producing no overall signal. Moving a magnetic sample, vertically through the center of pickup coils in upward direction, flux enclosure within the pick-up coil diameter increases in one set of coil and decreases in the other set of coil.

After centering the sample, the desired mode of measurement is started by running a sequence of programs written in LabView software. The LabView sequence has all control parameters which have to be fixed and specified before the measurement starts. All the hardware in VSM is controlled by LabView code which has separate modules of virtual instrumentation (VI) for individual hardware in the VSM. The interfacing to computer is achieved through serial ports using USB to RS232 handshakes and RS 232 serial communications.

A single crystal of Yttrium Iron Garnet (YIG) sphere which has the specific magnetization σ = 27.6 ± 0.1 emu/g, is used for calibration of VSM. Saturation magnetisation of YIG is 7.76 10^{-2} emu = 7.76 10^{-5} A m^2 at 298 K, 5000 Oe. Figure 2.15 (a) and (b) shows the magnetization measurement as a function of field and temperature on $BaFe_{1.29}Ru_{0.71}As_2$ single crystal. Such magnetization studies are used to estimate the

T_C, H_{C2} and critical current density of the superconducting samples, as discussed in subsequent chapters.

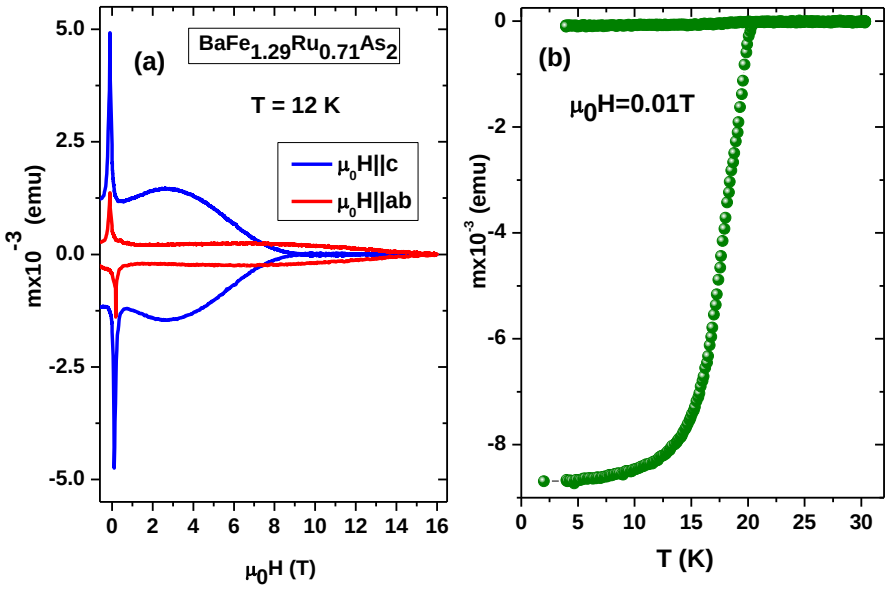

Figure-2.15 (a): Isothermal magnetization loops with field applied along *ab-plane* and *c-axis* of single crystal of $BaFe_{1.29}Ru_{0.71}As_2$. The magnetization loops were measured up to 16 T while the temperature was kept constant at 12 K These loops are used to calculate critical current density of samples (described in chapter 5) **(b):** Magnetization as a function of temperature measured at 0.01 T. These *M(T)* plots are used to measure H_{C2} and superconducting phase fractions in samples.

2.7.2 AC susceptibility

The temperature dependent ac susceptibility measurement can also be performed using the VSM. The schematic diagram of ac susceptibility setup is given in Figure 2.16. The ac susceptibility set up consists of a primary coil which is driven by an AC current to give a modest AC field (typically 1 mT at frequencies from 100 – 10000 Hz). The two secondary coils are the same pick-up coils essentially used in the VSM option. These are accurately matched and connected in series opposition so the net signal from these is close to zero. When a sample is positioned at the center of one of the secondary coils, the secondary coils become unbalanced due to the magnetic properties of the material. When

the signal from one coil is subtracted from the other the resultant voltage is no longer zero and it is this resultant voltage that is proportional to the AC susceptibility (χ).This voltage is usually very small which can be detected only phase sensitively. The lock in amplifier detects both the in and out of phase signals from the coils, which are termed as real and imaginary components of χ, usually denoted as χ' and χ'' respectively. The results of such measurements in P-doped Arsenide [13] are shown in figure 2.17

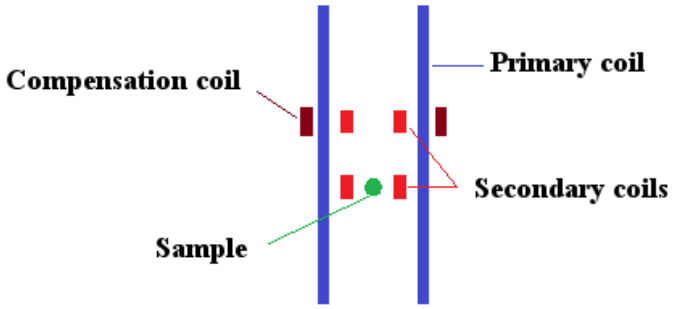

Figure 2.16: Schematic representation of AC Susceptibility pick-up coils. Figure shows primary coils generating the driving AC field that is superimposed on the DC field from superconducting solenoid. The oppositely wound secondary coils sense any additional signal due to the magnetic susceptibility of the sample in one of the secondary arm. Offset voltages in the secondary coils are compensated at each temperature using the compensation coils wound on one of the secondary coil as shown in figure

As an example to show the use of AC susceptibility measurements for estimation of critical current density, the results and estimation methodology are presented for the polycrystalline P substituted $PrOFe_{0.9}Co_{0.1}As_{1-x}P_x$ superconductors [13]. J_C was obtained from the AC susceptibility measurements carried out as a function of DC magnetic field, for different AC field amplitudes. In the critical state model [14-16], the peak in $\chi''(H)$ of the superconducting slab of thickness $2R$ gives an estimate of inter-granular current density J_C according to relation, $H_{AC} = \sqrt{2}\mu_0 J_C R$. H_{AC} is he amplitude of the applied AC field for which a peak was observed in $\chi''(H)$, and μ_0, is the permeability.

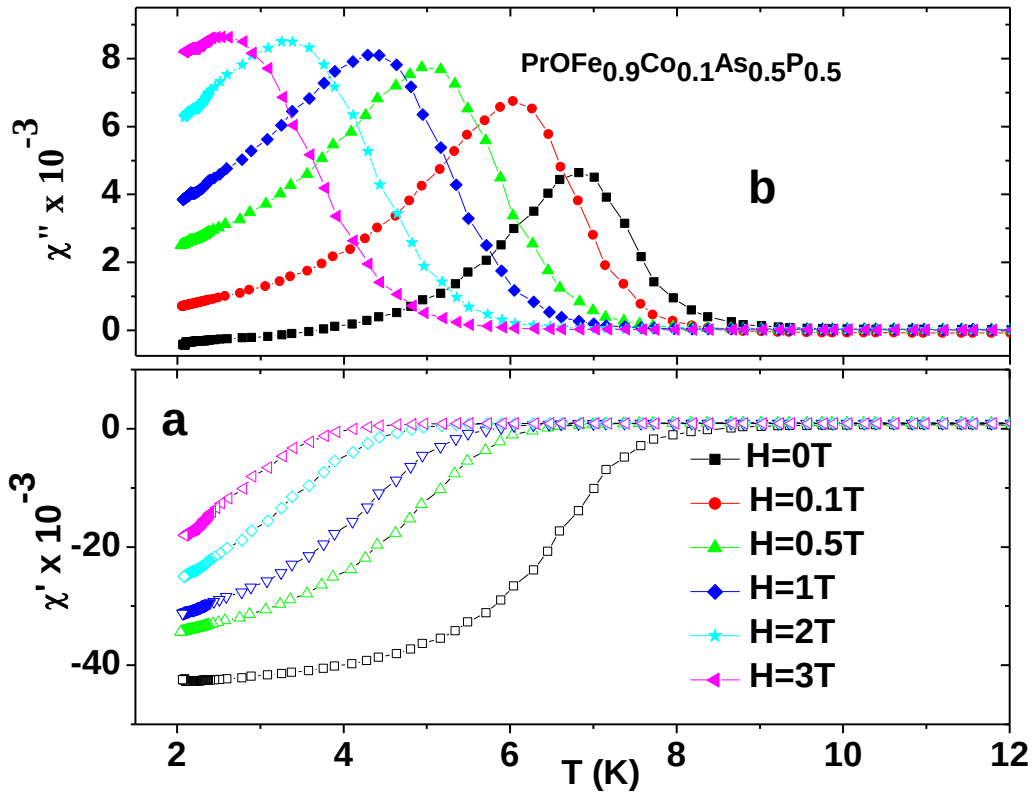

Figure 2.17 (a) and (b): Real and imaginary components of AC susceptibility as a function of temperature measured on polycrystals of P substituted $PrOFe_{0.9}Co_{0.1}As$ superconductor. The imaginary component show a peak near the mean field transition temperature but remains zero elsewhere. Real component of susceptibility show Meissner shielding.

In the Bean's critical state model, the peak in the imaginary component of AC susceptibility will occur when the field after penetrating the surface of superconductor reaches its center. Here $J_C(H_{DC}+H_{AC})$ is taken to be independent of AC driving field since $\mu_0 H_{DC} >> \mu_0 H_{AC}$ ($\mu_0 H_{AC}$~ 0.1 mT). For performing these measurements, the samples were shaped in the form of thin rectangular bar with a thickness 0.5 mm and length of around 4-5 mm. The sample was mounted such that the long axis of the sample lies along the DC field direction; the AC field was also applied along the direction of the DC field. AC fields used, ranged from 0.025 mT to 0.2 mT and frequency of the AC field was 941 Hz.

Figure 2.18 shows a plot of normalized χ'' as function of DC field for sample with a phosphorus fraction of x=0.2, measured at 8 K. From the particular value of AC magnetic field and sample width *2R*, $J_C(H)$ was calculated for all the samples at that DC field $\mu_0 H$ at which a peak in $\chi''(H)$ plot occurs. From similar measurements done on several P substituted samples, $J_C(H)$ was obtained for different phosphorus substitutions and is shown in inset of figure 2.18.

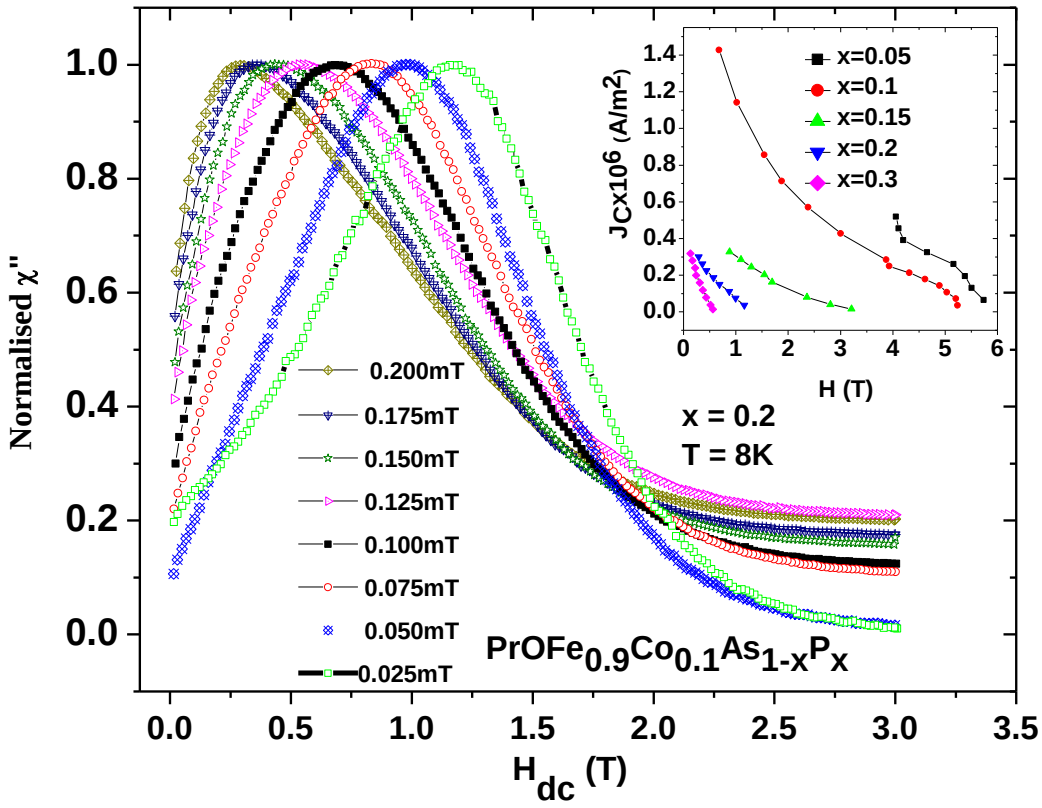

Figure 2.18: In-field intra-grain current density $J_C(H)$ for different P substituted compounds, measured using AC susceptibility; inset: Variation of χ'' with DC magnetic field at different AC fields applied parallel to DC field. A peak in imaginary susceptibility can be seen to shift lower DC fields with increasing AC driving field. Peak occurs at that DC field for which flux profile inside the superconductor reaches center.

The AC susceptibility technique is very useful to estimate critical current density of samples in the presence of large fraction of magnetic impurities. However, in our case, due to the small size of Ru substituted single crystals, signal in the AC susceptibility measurement was not large enough to be used for $J_C(H)$ estimation. Thus the isothermal magnetization measurement protocol described in section 2.7.1 was used for the determination of J_C of our $BaFe_{2-x}Ru_xAs_2$ single crystals and these results are presented in Chapter 5.

References

[1] Bharathi A, Sharma S, Paulraj S, Satya A T, Hariharan Y and Sundar C S 2010 Critical properties of superconducting $Ba_{1-x}K_xFe_2As_2$ *Physica C: Superconductivity* **470** 8-11

[2] Balaselvi J 2004 Studies on Magensium Diboride and Related Systems. In: *Ph.D. Thesis*: University of Madras)

[3] Hammersley A P, Svensson S O, Hanfland M, Fitch A N and Hausermann D 1996 Two-dimensional detector software: From real detector to idealised image or two-theta scan *High Pressure Research* **14** 235-48

[4] Toby B 2001 EXPGUI, a graphical user interface for GSAS *Journal of Applied Crystallography* **34** 210-3

[5] Van der Pauw L J 1958 A Method of Measuring Specific Resistivity and Hall Effect of Discs of Arbitrary Shape *Philips Research reports* **13** 1-9

[6] Van der Pauw L J 1959 A Method of Measuring The Resistivity and Hall Coefficient of Lamellae of Arbitrary Shape *Philips Technical Review* **20** 220

[7] Sharma S, Bharathi A, Hariharan Y and Sundar C S 2008 Hall Coefficient measurements in $Ba_{1-x}K_xFe_2As_2$ superconductor *Proceedings of DAE Solid State Physics Symposium* **53** 917

[8] Hall E H 1879 On a New Action of the Magnet on Electric Currents *American Journal of Mathematics* **2** 287

[9] Parisini A and Reverberi R 1989 Computer-assisted Hall effect measurements as a function of temperature *European Journal of Physics* **10** 281

[10] Riss O, Shaked E, Karpovsky M and Gerber A 2008 Offset reduction in Hall effect measurements using a nonswitching van der Pauw technique *Review of Scientific Instruments* **79** 073901-3

[11] Levy M and Sarachik M P 1989 Measurement of the Hall coefficient using van der Pauw method without magnetic field reversal *Review of Scientific Instruments* **60** 1342-3

[12] Wu G, Liu R H, Chen H, Yan Y J, Wu T, Xie Y L, Ying J J, Wang X F, Fang D F and Chen X H 2008 Transport properties and superconductivity in $Ba_{1-x}M_xFe_2As_2$ (M=La and K) with double FeAs layers *EPL (Europhysics Letters)* **84** 27010

[13] Shilpam S and et al. 2011 Superconducting And Critical Properties of $PrOFe_{0.9}$ $Co_{0.1}As$: Effect of P Doping *Superconductor Science and Technology* **24** 065020

[14] Gömöry F, Forsthuber M and Hilscher G 1993 Field dependence of critical current density determined from a.c. susceptibility measurements *Cryogenics* **33** 277-80

[15] Fedor G 1997 Characterization of high-temperature superconductors by AC susceptibility measurements *Superconductor Science and Technology* **10** 523

[16] Gömöry F 1989 Fast inductive method for determination of macroscopic critical current density in bulk high-Tc superconductors *Solid State Communications* **70** 879-83

Chapter 3

Superconductivity in Ru-substituted $BaFe_2As_2$: Phase Diagram

This chapter reports on the occurrence of bulk superconductivity in polycrystalline and single crystalline specimens of $BaFe_{2-x}Ru_xAs_2$ at ~22 K. From the features in the resistivity as function of temperature data for several Ru contents, the variation of the Spin Density Wave (SDW) transition and occurrence of superconducting transitions were determined. This enabled the mapping of the phase diagram. Experimental evidence for the weakening of magnetic moment on Fe with increase in Ru substitution is obtained from low temperature and high field Mossbauer measurements. Band structure calculations were performed to understand the electronic structure changes induced by Ru substitution. The growth of single crystals enabled us to study the correlation in structural parameters with superconductivity in the system. From Rietveld refinement of XRD data, detailed study of structural parameters at room temperature and their variation with increase in Ru concentration has been carried out. The results of low temperature single crystal XRD measurements across structural phase transition were performed to see the correlation between superconductivity and orthorhombicity. Finally the T-x phase diagram, established from the measurements on single crystals, is presented.

3.1 Introduction

As discussed in Chapter 1, the discovery of Fe based superconductors gained impetus after LaFePO was found to superconduct at 5 K [1] and two years later report on superconductivity in $LaFeAs(O_{1-x}F_x)$ at 26 K [2] by fluorine doping at oxygen site. Around the same time Rotter *et al.* [3] discovered $BaFe_2As_2$, a compound having similar

layered structure comprising of two FeAs layers sandwiching a Barium atom in between (see figure 1.2). The pristine $BaFe_2As_2$ has a spin density wave (SDW) ground state that gives way to a superconducting state by charge doping and application of external pressure [4-8]. The first report [4] of superconductivity in $BaFe_2As_2$ was by hole doping with the substitution of potassium (K) at Ba site. It was found that a nominal potassium substitution (x = 0.4) induces superconductivity at ~38 K after fully suppressing the structural and magnetic transition. Single crystals of the K-doped system were later on synthesized using Sn flux and self-flux [5, 9]. Several transition-metal (*TM*) substitutions $BaFe_{2-x}TM_xAs_2$ with electrons in excess of iron have been studied but the maximum transition temperature has remained at 25 K for Co-doped $Ba(Fe_{1-x}Co_x)_2As_2$ system [6, 10]. Similar to Co, Ni-doping was also found to induce superconductivity at ~ 20.5 K when substituted at the Fe site [11]. In the case of $Ba(Fe_{1-x}Ni_x)_2As_2$, the suppression of SDW state and structural transition along with appearance of superconductivity has been similar to Co-doped system except for the fact that the Ni substitution induces superconductivity faster than Co [12].

Although *TM* doping of the $BaFe_2As_2$ system is convenient because large, good quality single crystals can be synthesized easily [12], it is not the only way of tuning the $BaFe_2As_2$ system to induce superconductivity. Pressure can also be used to suppress the magnetic and structural transitions and stabilize a superconducting ground state [7, 13, 14]. A much higher T_C of around 35 K was observed in $BaFe_2As_2$ by application of pressure [8]. Strained crystals of $BaFe_2As_2$ and $SrFe_2As_2$ show superconductivity even at ambient pressure [15]. A systematic investigation on the role of hydrostatic pressure in the pressure dependent resistivity revealed that uniaxial pressure favors the occurrence of

superconductivity at a higher T_C ~35 K whereas truly hydrostatic pressure induces superconductivity at a lower temperature ~29 K [16].

In rationalizing the occurrence of superconductivity with both pressure and doping, attempts have been made to look for the crucial role of Fe-As bond lengths. In the case of *Re*OFeAs (*Re* = rare earth) family it was found that the T_C is optimized at a particular Fe-As distance [17] and/or at a particular $FeAs_4$ tetrahedral angle [18]. This indicates that the local structure of the $FeAs_4$ tetrahedra is crucial for bringing in superconductivity and the maximum transition temperature in these superconductors. Attempts have been made to understand if there is a common origin of superconductivity induced by mechanical pressure and substitution [19, 20].

Since the superconductivity in the FeAs based compounds depends upon the local structure of $FeAs_4$ tetrahedra, isovalent substitutions in $BaFe_2As_2$ were also tried for inducing superconductivity by many groups. Isovalent substitutions are expected to exert chemical pressure. Superconductivity was observed with a maximum T_C ~30 K by isovalent phosphorus substitution at As site in the $BaFe_2As_2$ [21] and T_C ~26 K has been found in $EuFe_2As_{2-x}P_x$ [22]. Furthermore, it has been shown by Klintberg *et al.* [23] that the effect of mechanical and chemical pressure is similar and the maximum T_C was identical in both.

Ru if substituted at Fe site, being larger in size should introduce steric effects, affecting the Fe-As bond length leading to the distortion of $FeAs_4$ tetrahedra. In addition, the larger radius of Ru *4d* electron shell should increase the metal-metal overlap in the Fe/Ru layer and increase the hybridization, leading to a change in the band structure. Motivated by the attempts of inducing superconductivity by mechanical and chemical

pressure, isovalent substitution of Ru at Fe site in $BaFe_2As_2$ was attempted [24] and a superconducting ground state was discovered. It must be mentioned here that superconductivity in isovalent substitution at Fe site in $SrFe_{2-x}Ru_xAs_2$ was also reported [25].

This chapter reports the stabilization of the superconducting ground state after suppression of structural and magnetic transitions in $BaFe_{2-x}Ru_xAs_2$ polycrystalline system. From the features in the resistivity as function of temperature for several Ru contents, the variation of SDW transition and occurrence of superconducting transitions have been determined. This has enabled the mapping of T_C/T_{SDW} vs. *'x'* phase diagram for poly crystalline samples. Band structure calculations were performed to understand the electronic structure changes induced by Ru-substitution. Electronic structure calculations were also used to calculate the magnetic moment on Fe that shows a minimum for the superconducting composition. Experimentally, through low temperature and high field Mossbauer measurements, evidence for the weakening of magnetic moment on Fe with increase in Ru-substitution is presented. Following the initial experiments on polycrystalline samples, experiments were carried out on single crystals. This was necessitated to resolve the discrepancy between our *T-x* phase diagram [24], and those reported subsequently [26, 27], as also for in-depth measurements on transport and magnetic properties of the new superconductor. Detailed structural changes with increase in Ru concentration have been obtained from Rietveld refinement of XRD data collected at INDUS-II synchrotron. Low temperature single crystal XRD to track the orthorhombicity as function of Ru fraction was performed at HRXRD beam line of PETRA synchrotron. Attempts have been made to correlate orthorhombic distortions in

under substituted $BaFe_{2-x}Ru_xAs_2$ single crystals to the superconductivity in the system. The results of above mentioned studies form the content of this Chapter.

3.2 Sample synthesis and X-ray diffraction

Polycrystalline samples of $BaFe_{2-x}Ru_xAs_2$, with x = 0.0, 0.25, 0.50, 0.75, 0.875, 1.0, 1.125, 1.25 and 1.5, have been synthesized by solid state reaction, starting from high purity FeAs and RuAs powders and Ba chunks, under 30 bar Ar pressure, as described in Chapter 2. The samples were characterized for phase formation and crystal structure by powder x-ray diffraction (XRD) using *Cu-*K_α radiation in STOE diffractometer operating in the Bragg-Brentano geometry. Figure 3.1 shows the XRD patterns for various compositions. The x-ray diffraction results indicate the formation of the I4/mmm, $ThCr_2Si_2$ structure for all Ru fractions substituted. A small fraction of impurity peaks due to Ru/Fe and Ba arsenides are also identified. Further grinding and heat treatments to get rid of impurities were found to degrade the samples as superconductivity was seen to get destroyed after further heat treatments and hence it was not performed.

The lattice parameters have been obtained from a least square fit to the observed '*d*' values using STOE software. The lattice parameter variations as a function of Ru concentration are shown in figure 3.2. It is clear from the figure that with Ru-substitution there is an increase in the '*a*'-lattice parameter, whereas the '*c*'-lattice parameter shows a decrease, leading to a decrease in the *c/a* ratio. There is an overall increase in the cell volume of ~1.18% for x = 1.0. Similar changes have been observed in the $SrFe_{2-x}Ru_xAs_2$ system [25].

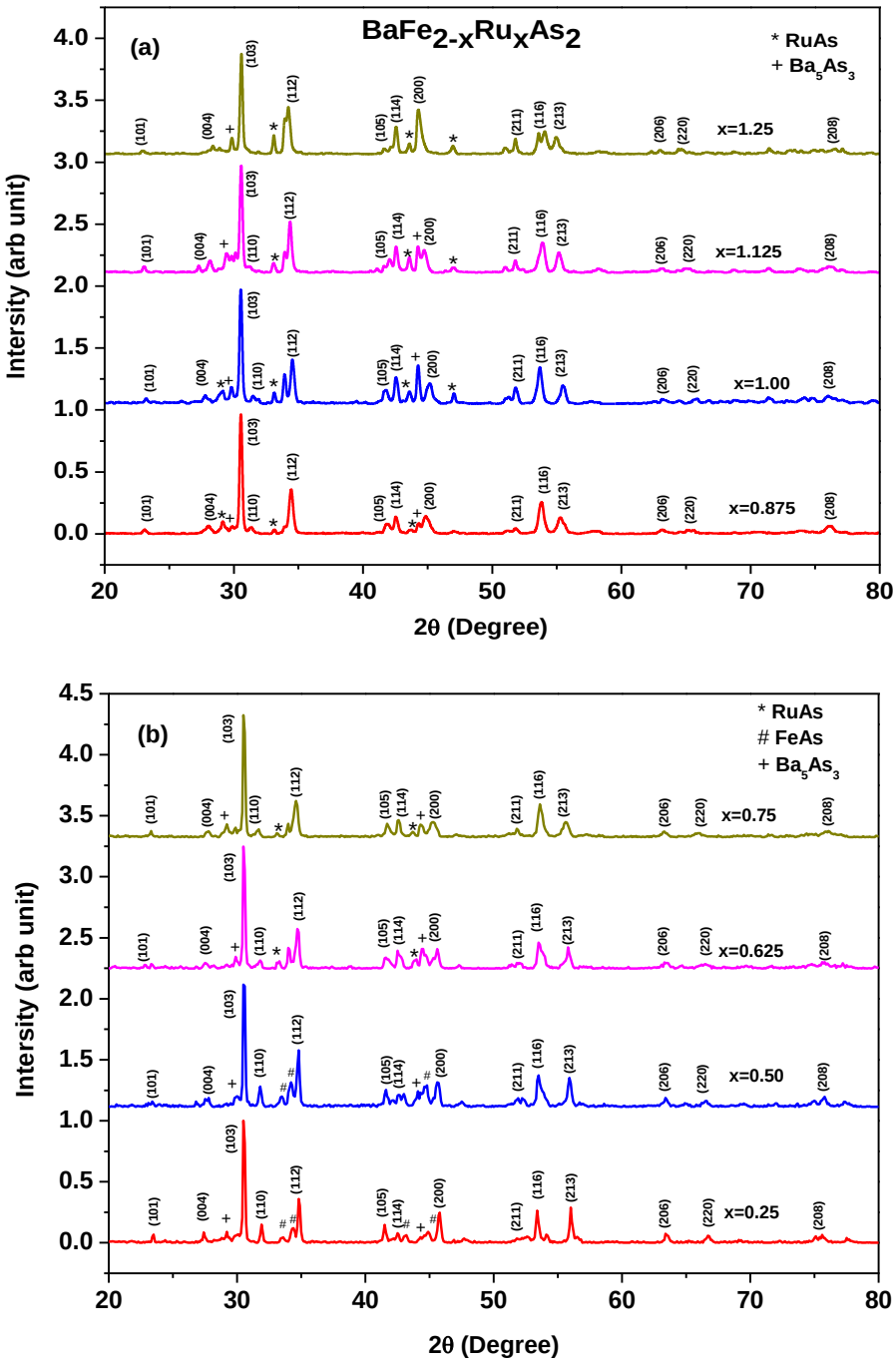

Figure 3.1 (a), (b): XRD patterns for all the Ru-substituted polycrystalline samples. Majority of the observed reflections could be indexed on the basis of tetragonal cell (I4/mmm). The x-ray diffraction results indicate the formation of the I4/mmm, $ThCr_2Si_2$ structure for all Ru fractions substituted. A small fraction of impurity peaks due to Ru/Fe and Ba arsenides can be seen.

It must be mentioned that the changes in the cell parameters due to Ru-substitution contrasts with the variations obtained in Co [28] and P-substituted $BaFe_2As_2$ [21] and that under the application of pressure [20], wherein a monotonic decrease in cell volume arises as a consequence of a decrease in both the '*a*' and '*c*' lattice parameters. Further, in the case of $Ba_{1-x}K_xFe_2As_2$ system, while the '*a*'-lattice parameter decreases and '*c*'-lattice parameter increases, the cell volume remains constant with substitution. This suggests that the cell volume is not the only important factor in influencing the superconducting ground state of these compounds.

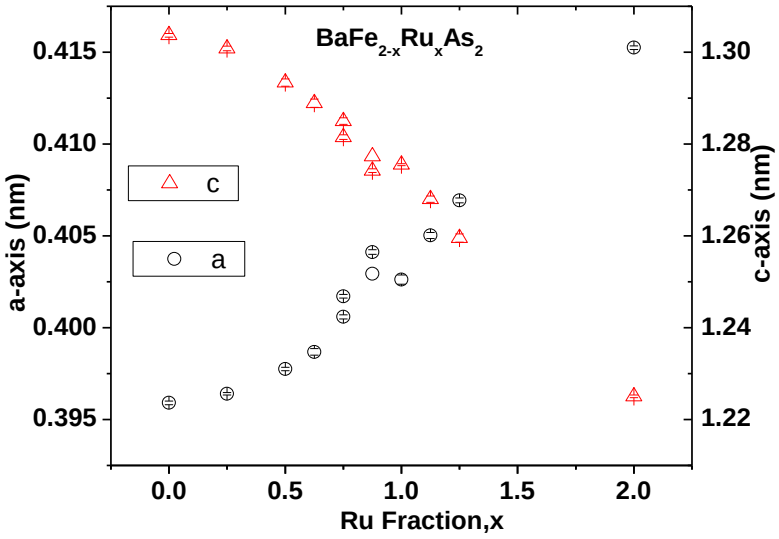

Figure 3.2: The lattice parameter variations obtained from XRD data as a function of Ru concentration. With Ru substitution there is an increase in the '*a*'-lattice parameter, whereas the '*c*'-lattice parameter shows a decrease, leading to a decrease in the *c/a* ratio. There is an overall increase in the cell volume of ~1.18% for $x = 1.0$.

Rietveld refinement has been performed for $x = 0.875$ sample using GSAS program [29]. From Rietveld analysis (shown in figure 3.3) of the XRD data of $x = 0.875$ sample, the fractional z-coordinate of Arsenic (z_{As}), transition metal-As bond length, the two ($e_{1,2}$) tetrahedral angles of $FeAs_4$ tetrahedron (see inset of figure 3.3) were

determined to be, 0.3554, 0.2424 nm and 112.51 degrees and 107.97 degrees respectively. The refined Ru composition x = 0.864, is close to the nominal composition. The tetrahedral angles are similar to those obtained in the case of isovalent substitution of phosphorus at As site for the optimal superconducting composition [21], but different from those seen under the application of pressure [20]. Thus, Ru-substitution in FeAs layer produces similar structural changes as produced by P-substitution. Detailed study of structural parameters as a function of Ru fraction for single crystals is presented in section 3.8.1.

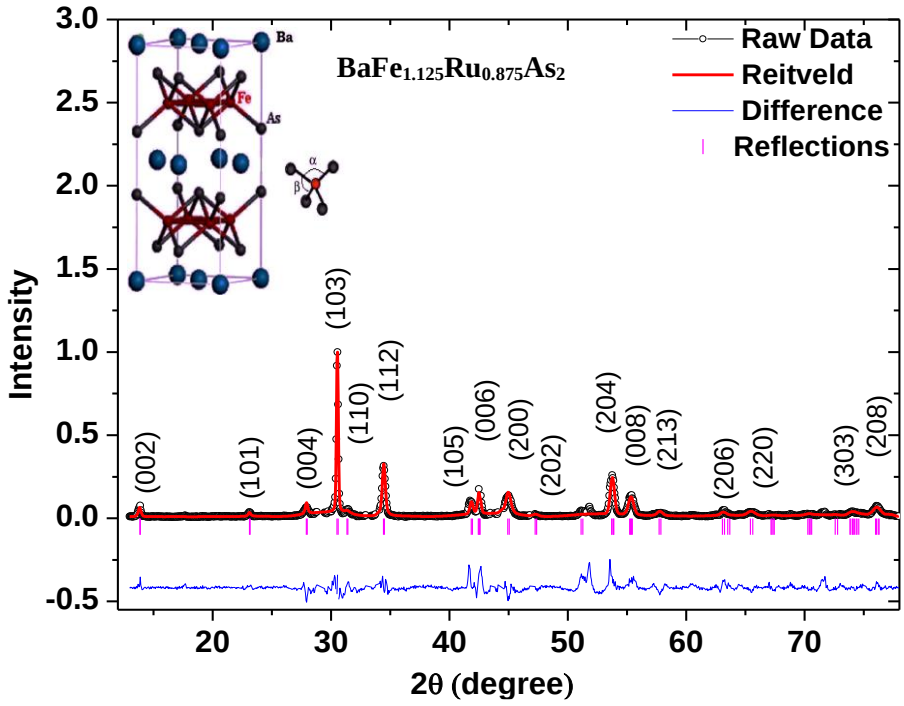

Figure 3.3: Rietveld analysis performed for x = 0.875 sample using GSAS program. From Rietveld analysis, the fractional z-coordinate of Arsenic (z_{As}), transition metal-As bond length, the two ($e_{1,2}$) tetrahedral angles of $FeAs_4$ tetrahedron were determined to be 0.3554, 0.2424 nm and 112.51 degrees and 107.97 degrees respectively. The refined Ru composition was determined to be 0.864, which is close to the nominal composition. **Inset:** shows the crystal structure of $BaFe_2As_2$ and the angles of $FeAs_4$ tetrahedra

3.3 Resistivity and magnetization measurements

The temperature dependence of resistivity normalized to the room temperature value obtained in all Ru-substituted samples is shown in various panels in figure 3.4. The well-known drop in resistivity corresponding to the SDW transition [3] seen in $BaFe_2As_2$, is clearly visible at ~ 140 K in the x = 0.0 sample. With increasing Ru-substitution viz., for x = 0.25 0.50 and 0.625, the room temperature resistivity decreases and the SDW transition shifts to a lower temperature. The onset of the SDW transition for the different Ru compositions are marked by '*' in the figure. For a Ru fraction of x = 0.75, a small bump due to the SDW transition is seen.

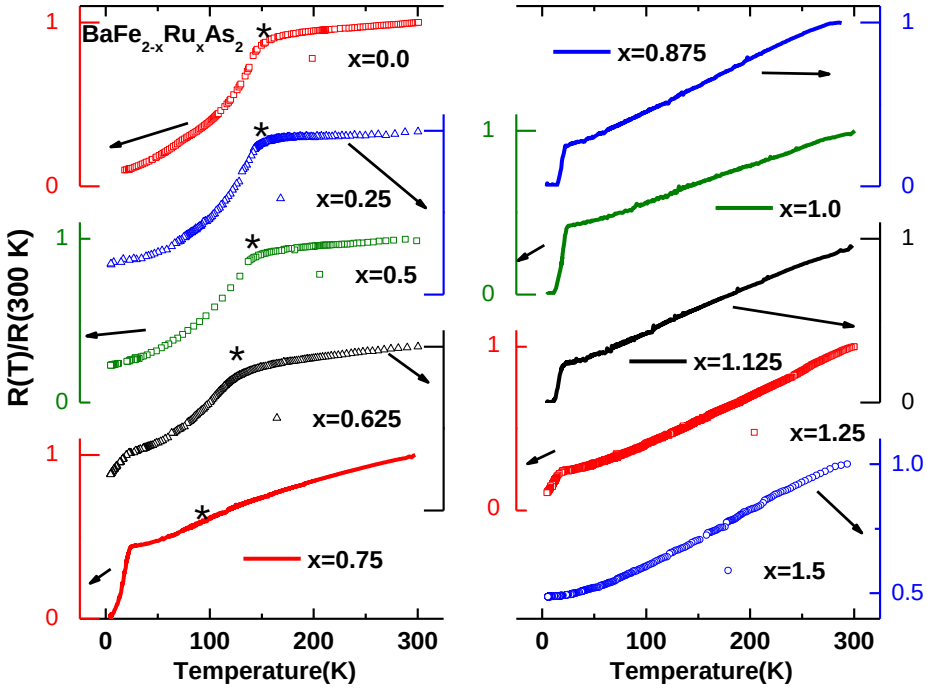

Figure 3.4: Variation in normalized resistivity with temperature in $BaFe_{2-x}Ru_xAs_2$ polycrystalline samples for various nominal Ru fractions 'x' indicated. The origin is shifted for each composition for clarity. The ordinate axis alternates for each composition showing the 0 and 1 markers. The SDW transitions are indicated by stars. A systematic suppression of SDW transition and stabilization of superconductivity is evident with increasing Ru content in the samples. Temperature dependence of normal state resistivity also changes with Ru fraction (see figure 3.6 and text below).

In addition, the resistivity in this sample shows a clear signature of the occurrence of a superconducting transition with an onset of 22 K, leading to zero resistance. This transition to the superconducting state is clearly seen in samples with Ru fraction of x = 0.875, x = 1.0 and x = 1.125, but the anomaly due to SDW transition is not observed in them. Further for the x = 0.625 and x = 1.25 samples, although a fall in *R(T)/R(300 K)* is observed, no zero resistance is seen and in the sample with x = 1.5 no drop in resistivity is observed. The results of zero field cooled (ZFC) magnetization data of the four samples with Ru fraction x = 0.75 to 1.125 are shown in figure 3.5.

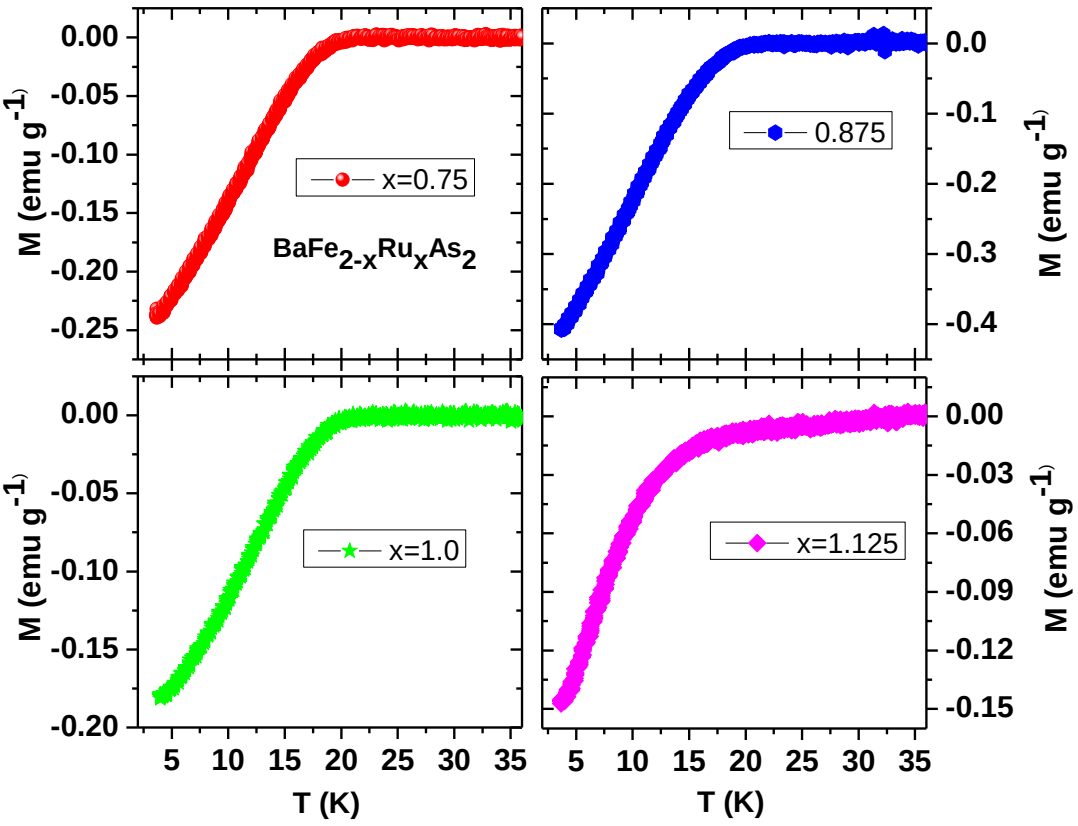

Figure 3.5: DC magnetization as a function of temperature for nominal x = 0.75, 0.875, 1.0 and 1.125 samples. Bulk superconductivity is evident from the magnetization plots. The transition temperatures vary only slightly and maximum T_C is found for x = 0.875 sample. The value of $|M|$ is seen to be maximum for the x = 0.875 sample having highest T_C ~ 20 K and the least for x = 1.125 sample.

The diamagnetic drop at ~20 K is evident from the data for samples with *x* in the range of *x* = 0.75 to *x* = 1.125. No diamagnetic signals were observed for samples with *x* = 0.625 and *x* = 1.25. The presence of zero resistance (see figure 3.4) and diamagnetism in the samples with Ru composition in the composition range of *x* = 0.75 to *x* = 1.125 provides unambiguous evidence for observance of superconductivity in the $BaFe_{2-x}Ru_xAs_2$ system in this composition regime.

The temperature dependence of the normal state resistance of various Ru-substituted samples is shown in figure 3.6. It is seen that for the *x* = 1.25 and 1.5 samples, the normal state resistivity acquires curvature.

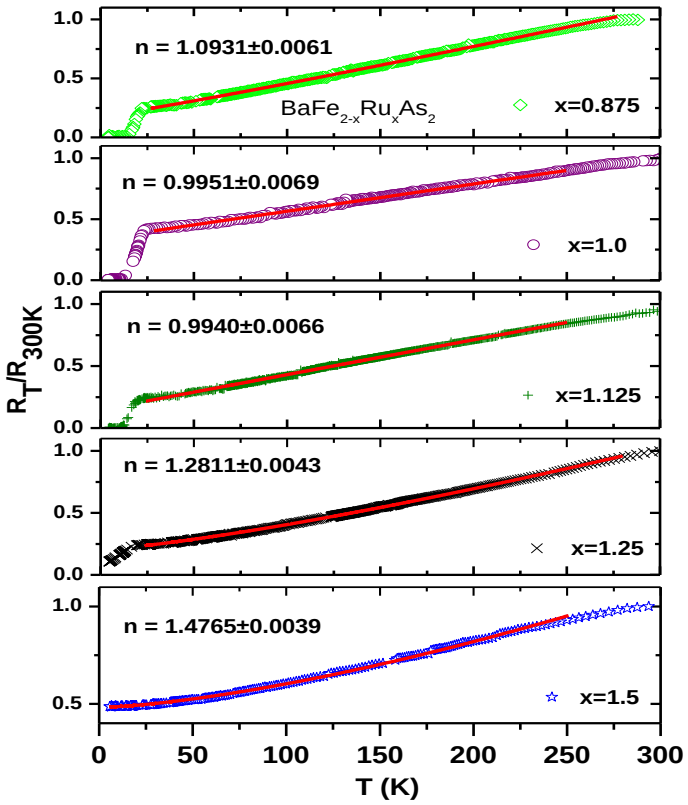

Figure 3.6: Fitting of normal state resistivity to power law T^n. power law changes from linear in *T* for the superconducting samples to *n* = 1.5 for over-substitute non-superconducting samples. The value of '*n*' close to 2 suggests a Fermi-liquid state arising due to electron-electron interactions. The linear low temperature resistivity in superconducting samples suggests a non-Fermi liquid behavior, as usually observed in the regime of quantum criticality

For these samples the *R(T)* in the normal state fit to a T^n power law with $n \sim 1.5$. It must be mentioned that a value of $n \sim 2$, suggests a Fermi-liquid state with electron-electron interactions. For the superconducting compositions, the normal state resistivity shows a linear dependence on the temperature, indicative of a non-Fermi liquid behavior, as usually observed in the regime of quantum criticality [21]. Similar composition dependent changes in the power law behavior of the normal state R(T) was seen in the $BaFe_2As_{2-x}P_x$ system [21] and under the application of pressure [8].

3.4 Phase diagram from studies on polycrystalline samples

Figure 3.7 summaries the variation of T_{SDW} and T_C as a function of Ru concentration, obtained from the resistivity curves shown in figure 3.4. The superconducting onsets obtained from magnetic measurements (figure 3.5) are also shown in the figure. It is evident from the figure that the SDW transition temperature decreases from that in the pristine compound for Ru fractions up to $x = 0.75$. A co-existence of SDW and superconductivity seems to occur in the $x = 0.75$ sample. For Ru fractions of $x = 0.875$, 1.0 and 1.125, only the superconducting phase is stabilized, and superconductivity is absent for Ru concentration greater than or equal to $x = 1.25$. Following this report on superconductivity in Ru-substituted $BaFe_2As_2$, studies were carried out on single crystals [26, 27] and a slightly different *T-x* phase diagram has been reported. Given this discrepancy, synthesis of single crystals of these compounds were carried out, followed by detailed structural and transport studies, to propose a new phase diagram, as described in section 3.8.3.

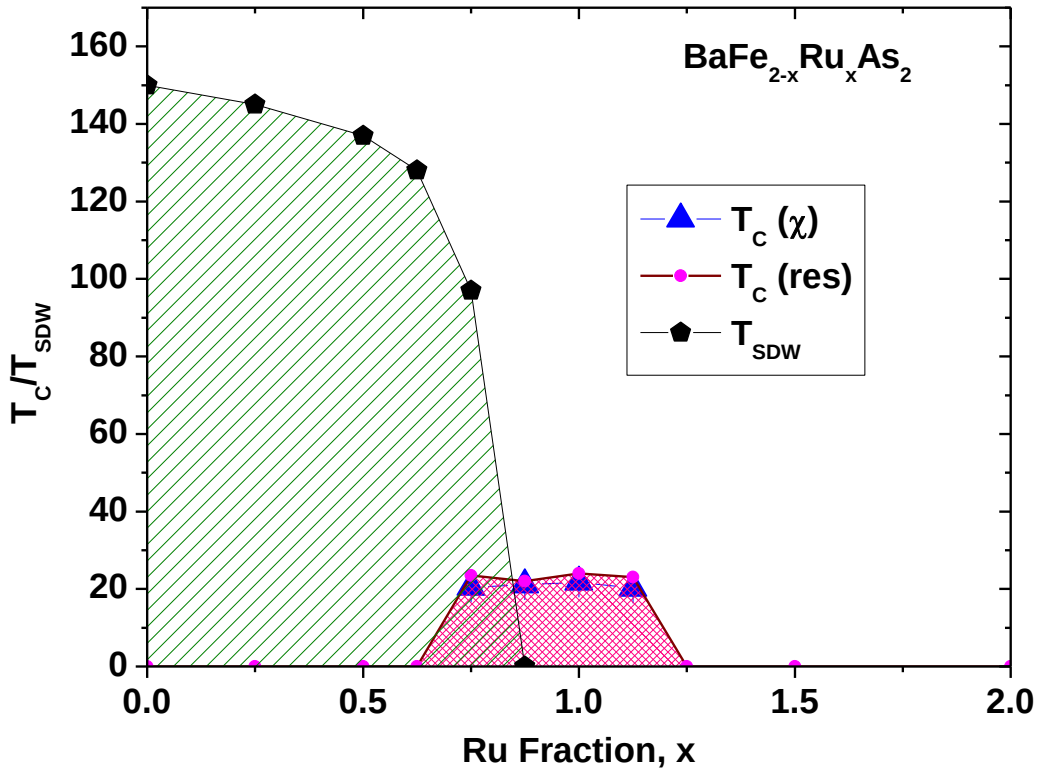

Figure 3.7: The variation of the SDW transition temperatures (T_{SDW}) and superconducting onsets (T_C) as a function of nominal Ru fraction x. Spin Density Wave and superconducting states co-exists for the x = 0.75 sample.

3.5 Hall effect measurements

To check on the nature of carriers introduced due to Ru-substitution, Hall co-efficient measurements have been carried out in the 10 K to 300 K temperature range in a home built set up in the Van der Pauw geometry (described in section 2.6). The R_H versus T for the single crystalline sample of $BaFe_2As_2$ is shown in figure 3.8 (b), and that for polycrystalline $BaFe_{2-x}Ru_xAs_2$ (x = 0.75) sample is displayed in figure 3.8 (a). Both the magnitude and temperature dependence of the Hall co-efficient for $BaFe_2As_2$, shown in figure 3.8 (b), are in agreement with earlier reports on single crystals of $BaFe_2As_2$ [30]. It is seen from figure 3.8 (a) that the R_H is negative in the normal state of the

superconducting Ru-substituted sample. The R_H values also show the characteristic drop to zero due to occurrence of superconductivity below ~20 K.

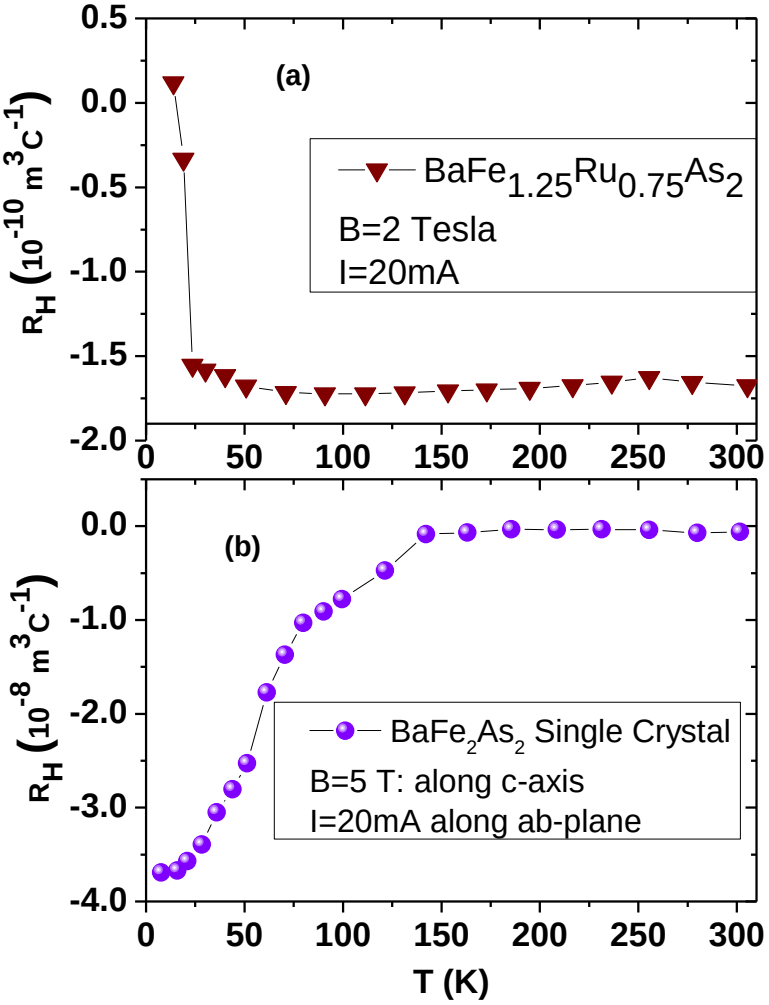

Figure 3.8: (a) Hall coefficient in polycrystalline $BaFe_{2-x}Ru_xAs_2$ for $x = 0.75$; the measuring field and current used in the experiments are indicated. The Hall coefficient was found to remain negative and nearly temperature independent down to superconducting temperature of the sample. No change in the sign of Hall coefficient was observed. (b) Temperature variation of Hall coefficient in $BaFe_2As_2$ single crystal.

The Hall coefficient in our polycrystalline sample does not show any sign change at low temperature but remains negative down to superconducting transition. It was however reported subsequently [26], that in the case of Ru-substituted single crystals the sample shows a sign change from negative at higher temperatures to positive at lower

temperatures near to the superconducting transition. In the case of multiband superconductors the temperature variation of Hall coefficient depends upon temperature variations of the electron and hole mobilities. The discrepancy in the low temperature behavior of Hall coefficient in our samples from that reported on single crystals [26] can be due to the polycrystalline ceramic nature of the samples.

To confirm the results of the Hall effect measurements and understand the effect of Ru-substitutions on electronic structure of $BaFe_2As_2$, we performed detailed band structure calculations for $BaFe_{2-x}Ru_xAs_2$ (x = 0, 0.5 and 1.0). Details of the calculations and results are described in next section.

3.6 Band structure calculations

To investigate how Ru-substitution affects the electronic structure, spin polarized density functional calculations have been performed for $BaFe_2As_2$, $BaFe_{1.5}Ru_{0.5}As_2$, $BaFe_{1.0}Ru_{1.0}As_2$, $BaFe_{0.50}Ru_{1.5}As_2$, and $BaRu_2As_2$, using the full potential linearized plane wave plus localized orbitals (FP-LAPW+LO) method, with the WIEN2k code [31] and the results are shown in figure 3.9. The generalized gradient approximation (PBE96) has been used for the exchange interaction. The calculations have been done with 1000 k points in full Brillouin zone and Muffin Tin radius times reciprocal lattice vector $R^*_{MT}K_{max}$ was 12 for all the calculations. Using the method outlined by D. J. Singh [32] for $BaFe_2As_2$, the ground-state-relaxed structure has been obtained. The muffin tin radii used were $2.2a_0$ for Ba and $2.1a_0$ for Fe, Ru and As, where a_0 is the Bohr radius [32]. The calculation was converged with respect to the energy, charge displacement and forces to the tune of 10^{-6} Ry, 10^{-6} Bohr and 1 mRy/Bohr respectively. The calculations have been

carried out using a superstructure (see Fig. 3.9 c) obtained by the $\sqrt{2}\times\sqrt{2}\times1$ construction ($a' = (a+b)$, $b' = (a-b)$, $c' = c$) from the ground state relaxed crystal structure of $BaFe_2As_2$ [33], as shown in Figure 3.9 (c). In this reconstructed structure, all the four Fe atoms occupy nonequivalent sites. The experimental lattice parameters of the Ru fraction 'x' = 0.5, 1.0 and 2.0 were used for the Ru-substituted electronic structure calculations.

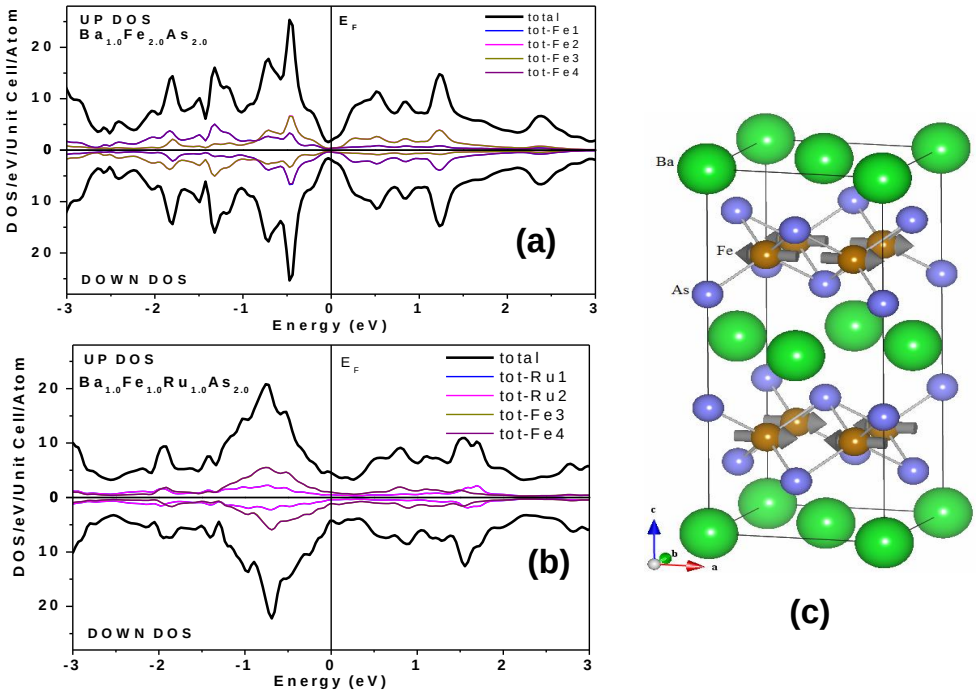

Figure 3.9: A comparison of the spin polarized density of states (DOS) obtained from first principles calculations in (a) $BaFe_2As_2$ and (b) $BaFe_{1.0}Ru_{1.0}As_2$. (c) Schematic of the structure of the super-cell used in the calculation.

The calculated DOS shown in figure 3.9 (a) for $BaFe_2As_2$ is in agreement with that obtained earlier [32]. The atom resolved DOS for *d*-Fe and *p*-As are also indicated in the figure 3.9. It was found that the Ba atom does not contribute appreciably to the DOS near the Fermi level (E_F). A steady increase in DOS at E_F was seen with increase in Ru-substitution. This is clear from figure 3.9 (b), where with 50% Ru-substitution, the DOS at E_F increases to 4.40 eV/unit cell/atom from 1.82 eV/unitcell/atom in the

$BaFe_2As_2$ (see from figure 3.9(a)). A similar increase in DOS at E_F has been observed for the $BaFe_2As_2$ system under the application of pressure and with K-doping [20]. The significant broadening and their increased contribution to DOS, suggests that the Fe *3d*-electrons get delocalized with Ru-substitution. Ru *d* levels also contribute to a small extent to the DOS at E_F. The converged E_F for $BaFe_2As_2$ is 0.60268 Ryd, while that for $BaFe_{1.5}Ru_{0.5}As_2$ is 0.63645 Ryd. The upward shift in E_F with Ru addition implies an increase in electron count due to Ru-substitution.

Figure 3.10 displays the evolution of the Fermi surface with Ru- substitution, as obtained from band structure calculations for the spin-down bands. The spin-up bands also show similar features in all the cases excepting for $x = 0.5$. A few notable features of Fermi surfaces shown in figure 3.10 are: (i) the Fermi surfaces become more connected with increase in Ru content, suggestive of increased delocalization of the carriers at E_F. (ii) Fermi surfaces for spin up and spin down electrons become very similar with increase in Ru content, suggesting a preference for a paramagnetic ground state for a substantial increase in Ru content and (iii) The Fermi surface gets larger, indicating electron addition due to Ru-substitution.

Band structure calculations were also used to evaluate the evolution of the magnetic state of $BaFe_2As_2$ as a function of Ru-substitution. For the $x = 0.0$ and $x = 0.5$ structures, the lowest energy occurs for the stripe anti-ferromagnetic order [33] and for the $x = 1.0$ and 1.5 superstructures, the lowest energy configuration turns out to be paramagnetic.

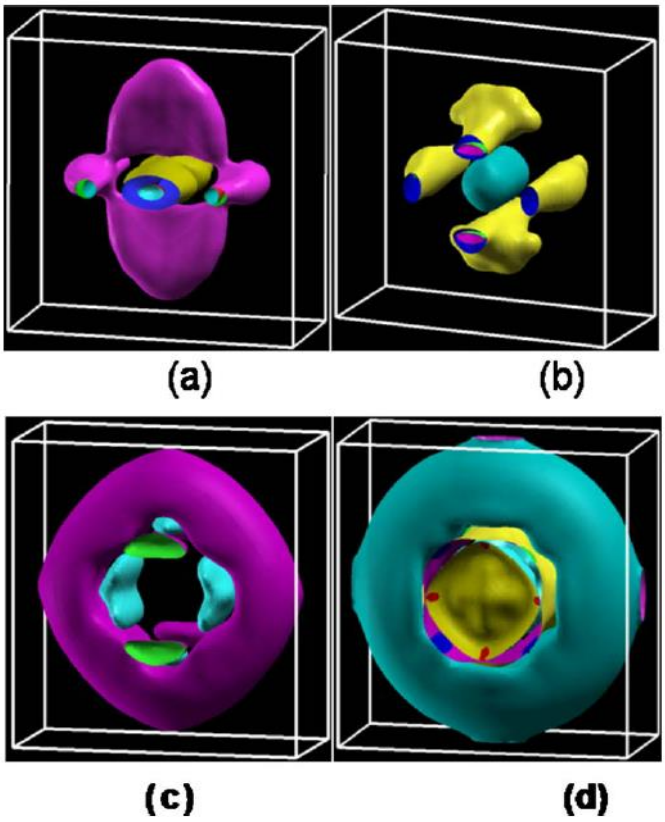

Figure 3.10: Evolution of the Fermi surface obtained from spin polarized DFT calculations for the spin up bands in $BaFe_{2-x}Ru_xAs_2$ for (a) x = 0.0, (b) x = 0.5, (c) x = 1.0 and (d) x = 2.0.

The magnetic moments of the Fe/Ru atoms were obtained from unconstrained minimization of total energy during the self-consistent iterations in the spin polarized calculations. It was seen that the Ru atoms always align antiferromagnetically to the Fe atoms and only in the presence of the Fe atoms, do they show a small magnetic moment. In the x = 0.5 and 1.5 compositions, there are three Fe(Ru) atoms for one Ru(Fe), whereas, for x = 1.0, there are two Fe atoms for two Ru. Hence for the x = 0.5 and 1.5 compositions, the magnetic moments obtained for all the Fe atoms in the unit cell are different. The variation of the magnitude of Fe and Ru moment with increase in Ru concentration is shown in figure 3.11, where the maximum of the moments obtained for the Fe/Ru atom are plotted. The Fe magnetic moment shows a minimum value at x = 1.0.

A small contribution from the Ru magnetic moment is also evident from figure 3.11. The Ru atoms in $BaRu_2As_2$ show zero magnetic moments.

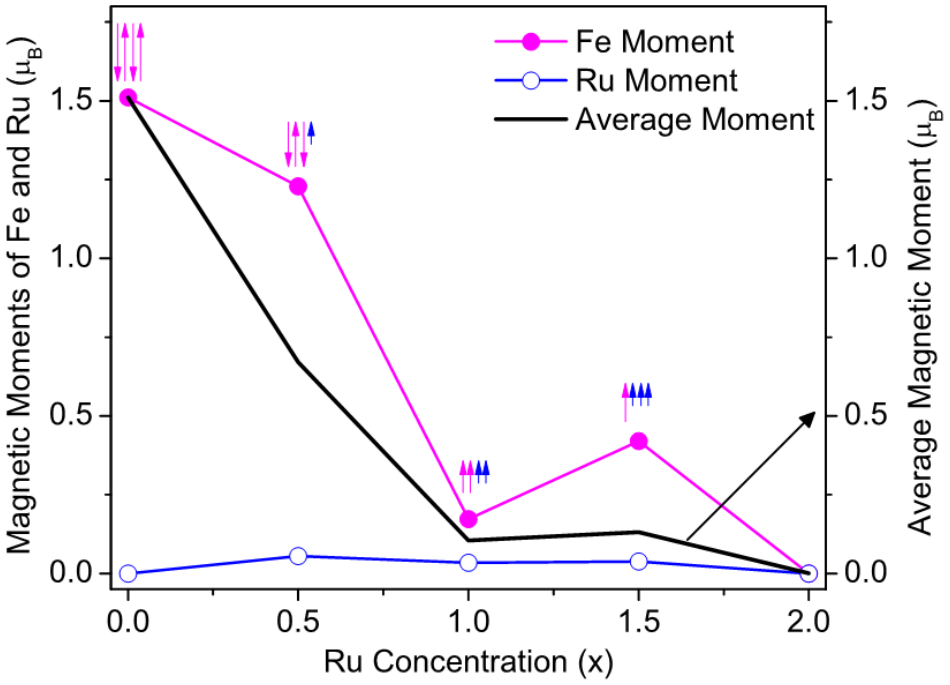

Figure 3.11: The variation of the calculated magnetic moment at the Fe site and Ru site with increase in Ru concentration in the supercell calculations.

3.7 Low temperature Mossbauer measurements

To experimentally investigate the magnetic moment at the Fe site, Mossbauer measurements have been carried out on the x = 0.0, 0.5 and 1.0 samples at 5 K. ^{57}Fe Mossbauer measurements were carried out at UGC-DAE CSR, Indore. These measurements have been performed in transmission geometry with ^{57}Co radioactive source in constant acceleration mode using standard PC-based Mossbauer spectrometer equipped with a Weissel make velocity drive. The measurements have been carried out at 300 K, 5 K and 5 Tesla external magnetic field applied parallel to the gamma rays (using JANIS SuperOptiMag superconducting magnet). Velocity calibration of the spectrometer was done with natural iron absorber at room temperature. The Mossbauer data for these

samples obtained at 5 K are displayed in figure 3.12. The Mossbauer data displayed for the x = 0.0 and 0.5 samples (see Figure 3.12 (a), (b)), show the characteristic six finger pattern due to magnetic ordering in the spin density wave state of the samples at 5 K. The magnetic hyperfine split data is analyzed with NORMOS-DIST program [34] and the data of superconducting sample is analyzed with NORMOS-SITE program [34].

The hyperfine magnetic split spectrum is fitted to a distribution of fields for x = 0 and 0.5 samples as shown by solid lines in the figure. The probability distribution of hyperfine fields obtained from the fits, for the x = 0.0 and 0.5 samples are shown in the inset of figure 3.12 (a). It is clear from the figure, that the hyperfine field distribution has a maximum at a field of ~ 5 T in the pristine sample and it becomes more spread out in the Ru containing sample with x = 0.5. The observed value of average hyperfine field (B_{HF}) for x = 0 sample matches closely with that obtained earlier [3, 35]. The Mossbauer spectrum of x = 1.0 sample shown in figure 3.12 (c) shows a broad singlet which is similar to that reported in potassium substituted samples which show superconductivity at 38 K [35]. The fitted data of figure 3.12 (c) has an isomer shift value of 0.55 ± 0.01 mm/sec corresponding to superconducting phase and a doublet with the hyperfine parameters matching with the $FeAs_2$ impurity phase [36]. The fraction of the $FeAs_2$ phase is estimated to be about ~3.5%. Figure 3.12 (d) shows the Mossbauer spectrum of x = 1.0 sample measured at 5 K and 5 Tesla external magnetic field. The fact that the observed effective B_{HF} (internal field) value is close to that of applied external magnetic field, within experimental errors, indicates that there is no magnetic ordering present in the x = 1.0 sample. The Mossbauer results thus indicate the magnetic interactions due to the

SDW phase weaken with Ru-substitution and are altogether absent in the superconducting sample with Ru composition of x = 1.0.

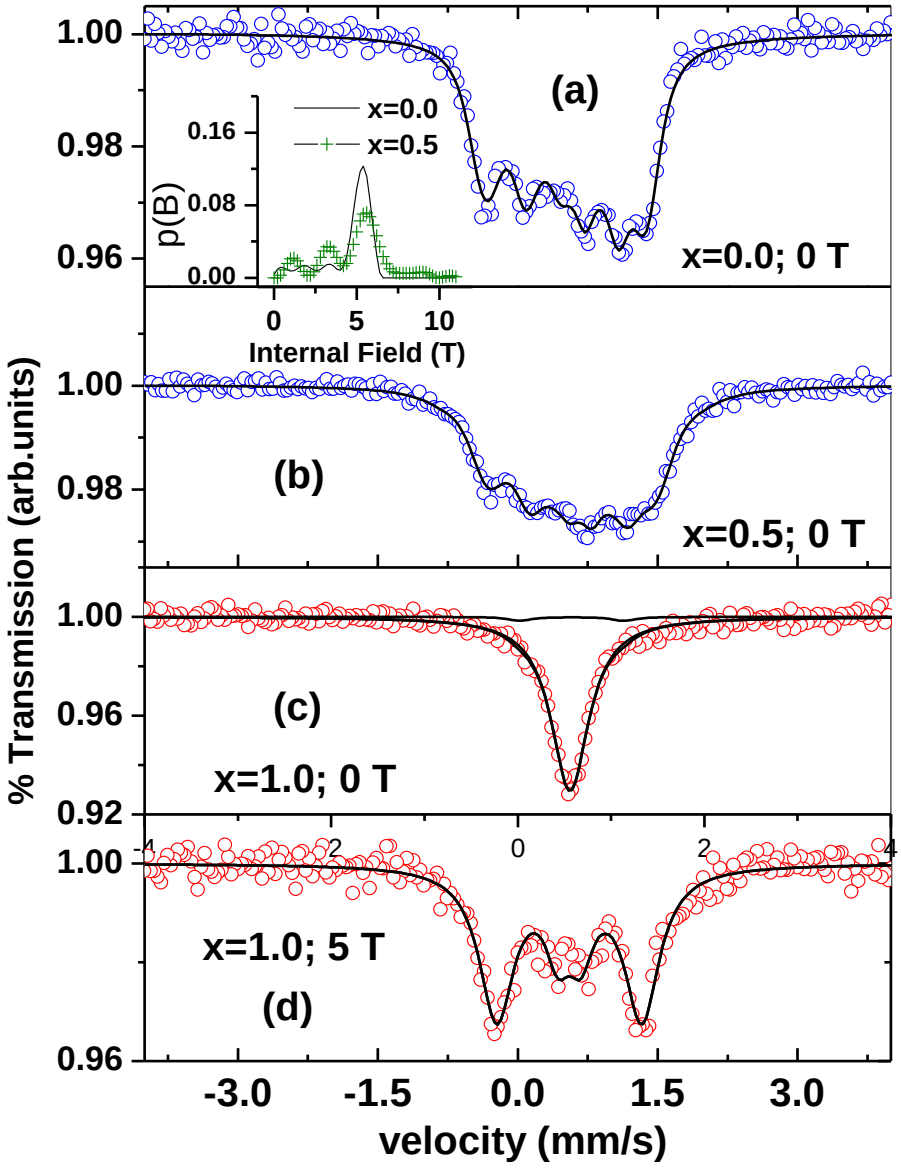

Figure 3.12: Mossbauer spectra measured at 5 K in $BaFe_{2-x}Ru_xAs_2$ samples with **(a)** x = 0.0, **(b)** x = 0.5 **(c)** x = 1.0 and **(d)** x = 1.0 with an external magnetic field of 5 T. **Inset** in **(a)** shows the probability distribution of the magnetic field for x = 0.0 and x = 0.5 samples, obtained from fits of the corresponding data shown in (a) and (b). It is clear from the figure, that the hyperfine field distribution has a maximum at a field of ~ 5 T in the pristine sample and it becomes more spread out in the Ru containing sample with x = 0.5.

3.8 Experiments on single crystals

As indicated earlier, (see from Sec. 3.4) the phase diagram shown in figure 3.7 was found to be at variance from the phase diagrams obtained for single crystal samples synthesized using flux growth techniques [26, 27]. To resolve this discrepancy, and also to study anisotropic superconducting properties of $BaFe_{2-x}Ru_xAs_2$, growth of Ru-substituted $BaFe_2As_2$ single crystals was attempted using high temperature melt growth technique. The crystals were grown without excess FeAs flux (see Chapter 2), by cooling from melt of stoichiometric ratios of Ba chunks, FeAs and RuAs powders. A large numbers of small shiny flat-plate like single crystals having dimensions around 1-2 mm^2 were grown (see figure 2.2)

The single crystals were characterized by powder XRD patterns shown in figure 3.13. For XRD measurements a large number of small crystals were powdered. Unlike the XRD pattern shown in figure 3.1 for polycrystalline samples, the XRD patterns in figure 3.13 show no impurity phases. The x-ray diffraction results indicate the formation of the I4/mmm, $ThCr_2Si_2$ structure for all Ru fractions substituted.

The lattice parameters, determined from the XRD data show a slight increase of *a*-lattice parameter while *c*-lattice parameter decreases with increase of the Ru content [37]. The variation of '*a*' and '*c*' lattice parameters with Ru fraction is shown in figure 3.14 (a) and (b) respectively. The variation of lattice constants with Ru fraction is similar to that of the polycrystalline samples shown in figure 3.2. The Ru content in the samples was estimated from the reported variation of '*c*' parameter with '*x*' determined from wavelength dispersive spectroscopy reported by Thaler *et al.* [27] and Rullier *et al.* [26].

The plot of nominal (x_{nom}) vs. estimated Ru fraction (x_{est}) is shown in figure 3.14 (c), which indicates that estimated value of Ru fraction x_{est} and its nominal value x_{nom} differ only slightly from one another.

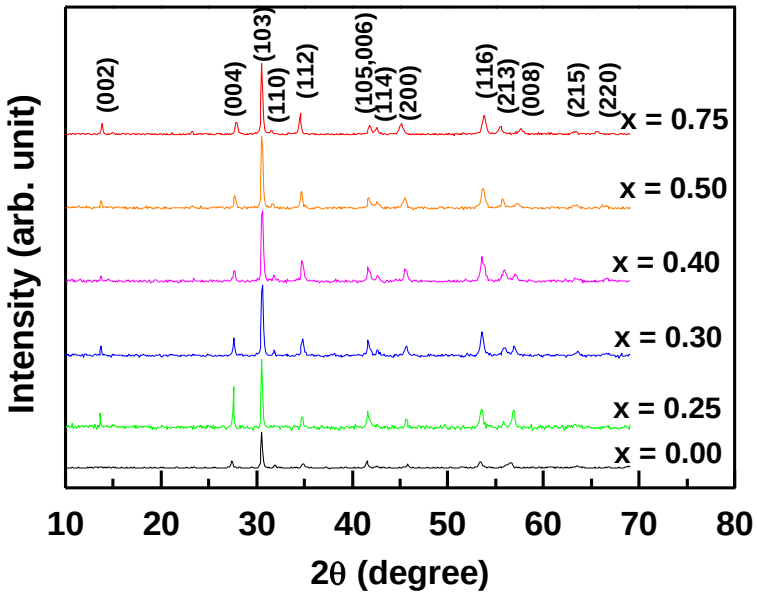

Figure 3.13: Powder XRD pattern of Ru-substituted $BaFe_2As_2$ single crystals. y-axis is shifted for clarity. For the powder XRD measurements a large number of small crystals were powdered. XRD patterns show no impurity phases. The x-ray diffraction results indicate the formation of the I4/mmm, $ThCr_2Si_2$ structure for all Ru fractions substituted.

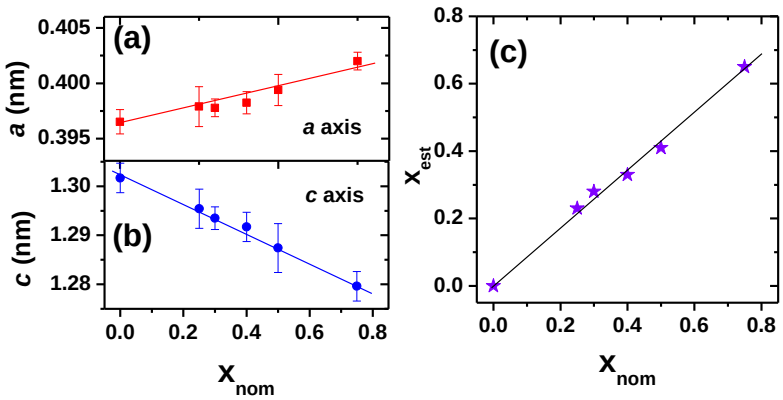

Figure 3.14 (a), (b): The lattice parameters, determined from the XRD data show a slight increase of *a*-lattice parameter while *c*-lattice parameter decreases with increase of the Ru content. The Ru content in the samples was estimated from the reported variation of '*c*' parameter with '*x*' determined from wavelength dispersive spectroscopy reported by Thaler *et al.* [27] and Rullier *et al.* [26]. (c).The plot of nominal (x_{nom}) vs. estimated Ru fraction (x_{est}) is shown.

3.8.1 Rietveld refinement: Relationship between T_C and structural properties

Investigations on the correlation between structural properties and transition temperatures of FeAs based superconductors have revealed that the transition temperature of these compounds is closely related to the structural properties like Fe-As bond angles, pnictogen height from Fe plane and orthorhombicity [19]. A correlation was reported for the wide range of parent compounds that the highest T_C occurred for the doped materials having least distorted $FeAs_4$ tetrahedra.

In order to determine the structural properties and their correlations with the transition temperature of $BaFe_{2-x}Ru_xAs_2$ superconductors, powder XRD patterns were recorded at BL-12 beam line of INDUS II synchrotron. XRD patterns were recorded in Debye-Scherrer geometry in the angle dispersive x-ray scattering beam line. The single crystals were finely powdered and were mounted on kapton tape. The diffraction rings were recorded on a MAR3450 image plate. X-ray energy of 13 keV was used and data was collected for 3-10 minutes for each sample. The 2D image plate data was converted to intensity vs. angle using FIT2D program [38].

Rietveld refinement of the XRD patterns was performed using GSAS program. Figure 3.15 (a) and (b) show the plot of XRD pattern along with refined pattern generated using GSAS program [29] for $BaFe_{1.45}Ru_{0.55}As_2$ and pristine $BaFe_2As_2$ samples. It can be seen from figure 3.15 that the error between experimental pattern and the refined pattern is very small. The refined Ru fraction in the samples was found to be near to the nominal concentrations used for sample synthesis. Shown in figure 3.16 is the variation of '*a*' and '*c*' lattice parameters as a function of Ru fraction.

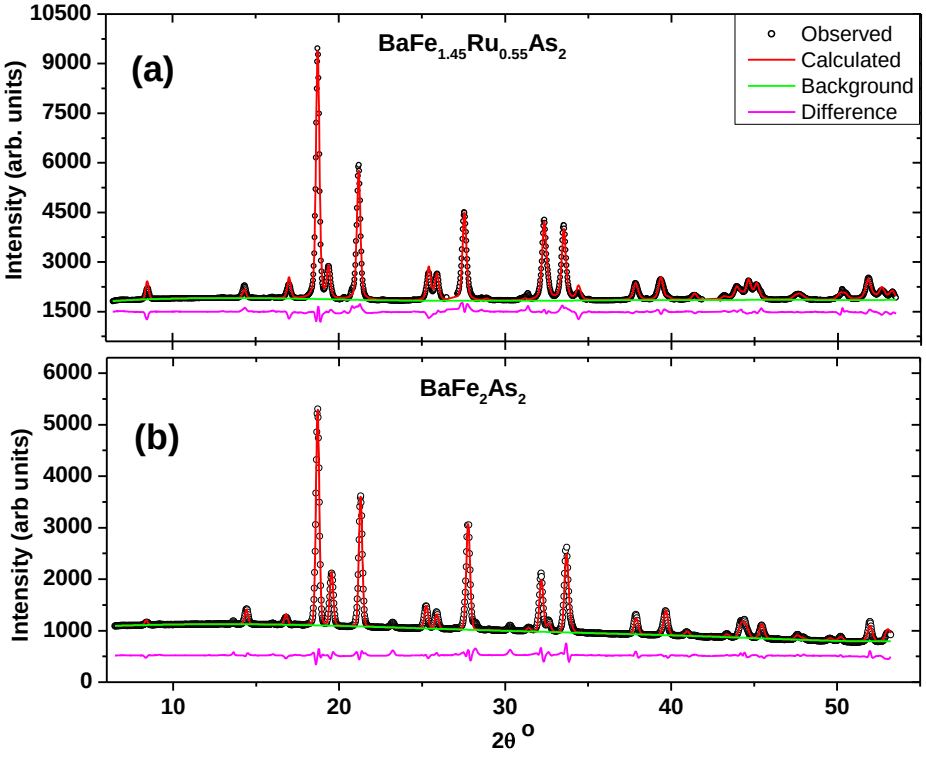

Figure 3.15 (a): Rietveld refinement of XRD pattern of $BaFe_{1.45}Ru_{0.55}As_2$ single crystalline sample shows no impurity peaks. The calculated intensity fits the observed data very well with very little errors. Calculated Ru fraction was found to be closer to nominal concentration. **(b):** Refinement of XRD pattern of pristine $BaFe_2As_2$ single crystals. All the peaks in the observed data fit well to I4/mmm space group with $ThCr_2Si_2$ structure.

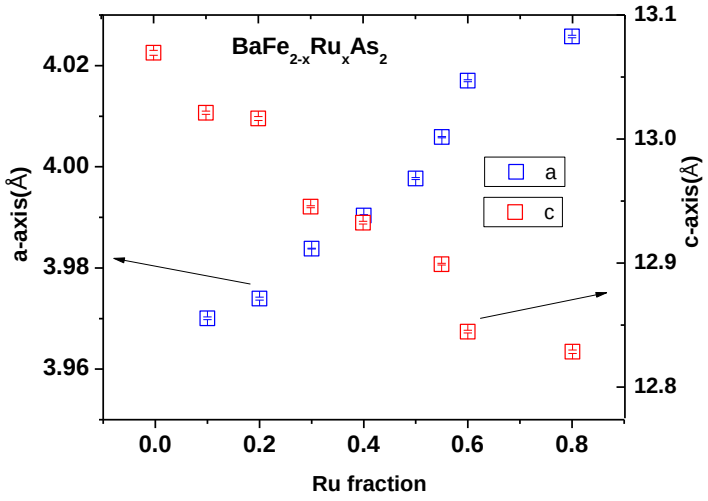

Figure 3.16: Variation of '*a*' and '*c*' lattice parameters found by Rietveld refinement of XRD data for powdered single crystals. The '*a*' lattice parameter was found to increase while the '*c*' lattice constant decreases with the increase of Ru content in the samples.

Figure 3.17 (a)-(d) presents the variation of arsenic fractional co-ordinate, height of As atoms in $FeAs_4$ tetrahedra, variation of tetrahedron angles, and Fe-As bond length respectively as a function of Ru content in the samples. With the increase in Ru fraction in the samples, the height of As atoms in the tetrahedron is seen to decrease whereas the fractional coordinate of arsenic (z_{As}) in unit cell was found to increase. The iron-arsenic bond length also decreases with the increase in Ru fraction. These effects on structure of $FeAs_4$ tetrahedra are arising due to larger size of Ru ion getting substituted at Fe site and distorting the tetrahedra as evident from the plot of As-Fe-As bond angle versus Ru fraction (see figure 3.17 (c)).

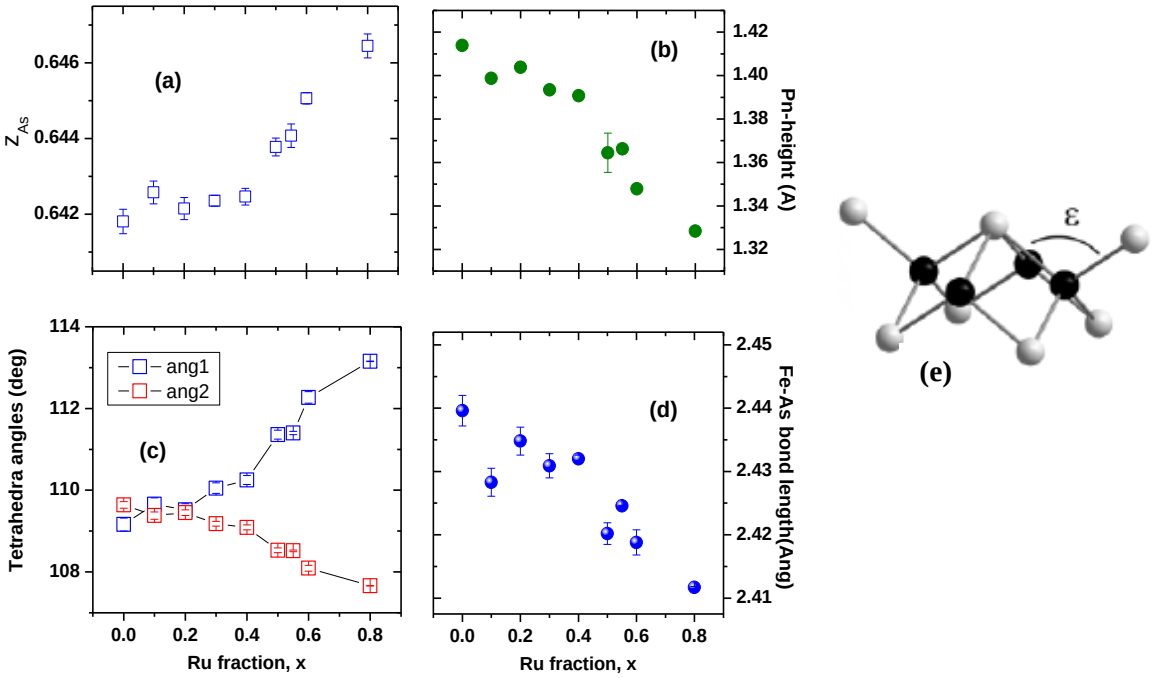

Figure 3.17 (a): The fractional co-ordinate of As atom in FeAs tetrahedron is found to increase with Ru fraction, **(b)** height of As atom from the Fe plane decreases as the Ru content increases in the samples. **(c)** the tetrahedron angles shows a distortion of tetrahedron upon Ru-substitution, **(d)** Fe-As-Fe bond length decrease as the Ru fraction increases. **(e)** $FeAs_4$ tetrahedra showing the two fold angles.

Shown in figure 3.18 (a) is the plot of T_C versus the twofold As-Fe-As angle for the superconducting $BaFe_{2-x}Ru_xAs_2$ system (see figure 3.17 (e)). For comparison, the data of our Ru-substituted samples is plotted along with the similar data taken from Johnston *et al.* [19]. Each point in the plot corresponds to the samples for which both structural properties data and transition temperature were known. From figures it is clear that a peak in T_C can be observed near 109.47° for nearly all the samples. Similar peak in Ru-substituted $BaFe_2As_2$ single crystals is slightly shifted to 111.4°. This however shows that for a higher T_C, the undistorted $FeAs_4$ tetrahedron can be one requirement.

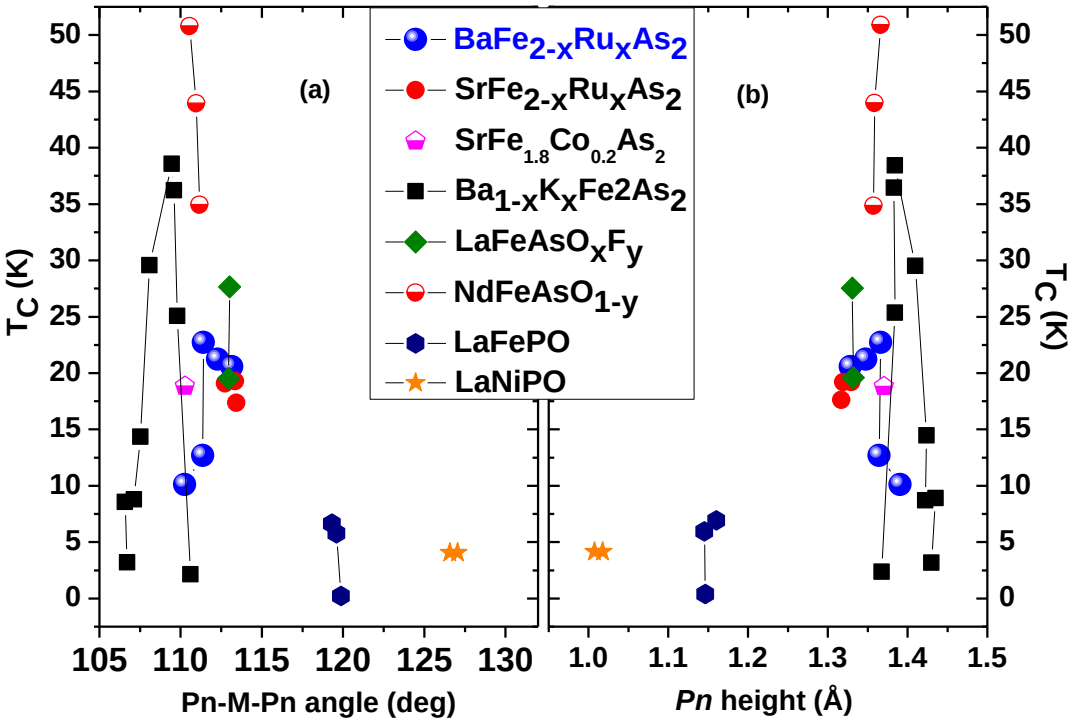

Figure 3.18 (a): Variation of T_C as a function of As-Fe-As tetrahedra two fold angle plotted alongside the similar data for other iron arsenide based superconductors compiled in Johnston *et al.* [19]. Other than a peak in T_C occurring for 109.47° there is no unique correlation between T_C and the two fold Fe-As-Fe angles. The peak in T_C for the K-doped compound occurs at the undistorted tetrahedron angle. **(b):** Variation of T_C with pnictogen height also shows correlation but the peak in transition temperature for the Ru-substituted samples is around 1.36 Å, which is closer to the As height ~1.38 Å in K-doped sample showing highest T_C.

Figure 3.19 (b) presents a similar plot showing T_C versus pnictogen (As) height. The peak for Ru-substituted samples occurs at 1.36 Å as compared to 1.38 Å for K-doped samples. Thus it is clear that similar to other doped $BaFe_2As_2$ superconductors, the superconductivity in Ru-substituted system is closely linked to its structural properties.

3.8.2 Low temperature crystal XRD: Temperature evolution of structural-magnetic phase transition

One of the points of interest in the $BaFe_2As_2$ based superconductors is the occurrence of a structural and magnetic transition (spin density wave) around 140 K [3, 19]. The high temperature tetragonal phase transforms to low temperature orthorhombic phase alongside with the high temperature paramagnetic phase getting ordered antiferromagnetically at low temperatures [19]. In the case of electron doped $BaFe_2As_2$, there is a small region of dopant fraction '*x*', where superconductivity and orthorhombic structural distortion coexist at low temperatures [19]. Since the magnetic (SDW) phase having orthorhombic symmetry coexists with superconductivity, it is evident that both orthorhombic and tetragonal phases support superconductivity in the FeAs based systems. It was seen that the orthorhombic distortion $\delta = (a-b)/(a+b)$ is influenced by superconductivity i.e. δ gets suppressed upon cooling below T_C [39]. A similar suppression in orthorhombic distortion upon cooling below T_C was found in single crystals of Rh-doped $BaFe_2As_2$ [40]. For both electron doped (Co, Rh) [39] and P-substituted [41] $BaFe_2As_2$, a splitting between structural and magnetic transition was found. In the case of Ru-substituted $BaFe_2As_2$, it was however reported by Thaler *et al*. [27] and Kim *et al.* [42] that similar to pristine and hole doped $BaFe_2As_2$ system, the structural-magnetic transitions are coincident in temperature. From the careful

experiments of neutron diffraction, AC susceptibility and resistivity [3, 33], it was shown that the anomalies in the resistivity can provide signatures of both the magnetic and structural phase transitions [39]. In fact, the *dR/dT* shows two distinct peak features which can be used to pin point the phase transitions.

To look for features due to the magnetic and structural transitions, resistivity as function of temperature was recorded for all the Ru- substituted samples. Figure 3.19 presents the variation of resistivity with temperature for Ru-substituted $BaFe_2As_2$ samples. A broad peak like feature associated with structural and magnetic phase transition is evident in the under-doped samples (up to $x = 0.5$). The peak like features in the resistivity keeps shifting to lower temperature with the increase in the Ru content in the samples and finally gets fully suppressed beyond $x = 0.5$ Ru fraction. Superconductivity onset is seen to co-exist with the SDW ground state in sample with $x = 0.3$ onwards. Figure 3.20 shows a plot of derivative of resistivity as a function of temperature along with the resistivity for one representative composition. It is clear from the plot that there is only one peak like feature in the derivative of resistivity of Ru-substituted samples. This indicates that the structural and magnetic transitions in the under-doped $BaFe_{2-x}Ru_xAs_2$ samples occur at same temperature, as reported previously [27]. The anomaly in the resistivity for under-doped samples points to a coincident structural and magnetic phase transitions. The investigation of correlation between the orthorhombic distortion and superconductivity in these compounds has been attempted. Similar to under-doped Co or Rh $BaFe_2As_2$ systems [39, 40], the temperature dependence across T_{SDW} and T_C of orthorhombic distortion was studied in the under substituted $BaFe_{2-x}Ru_xAs_2$ single crystals using high resolution single crystal XRD.

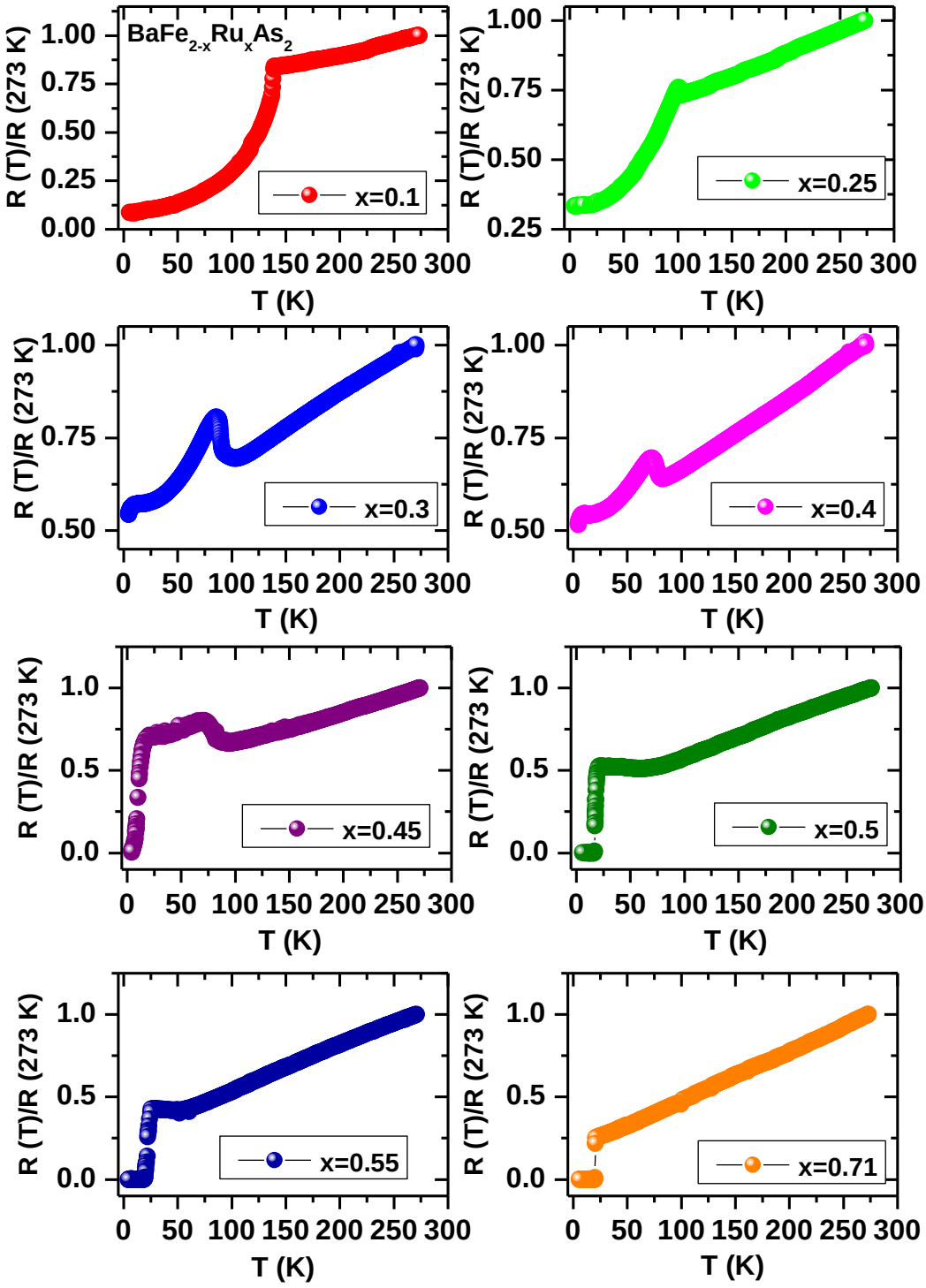

Figure 3.19: Plot showing variation of in-plane resistivity as a function of temperature for $BaFe_{2-x}Ru_xAs_2$ single crystal samples. The broad feature corresponding to the structural-magnetic transition is clearly seen for under substituted samples (0.25-0.45). The feature due to SDW/structural transition gets suppressed towards lower temperatures due to increasing Ru content in the crystals and finally superconducting transition is only seen for x = 0.5 onwards.

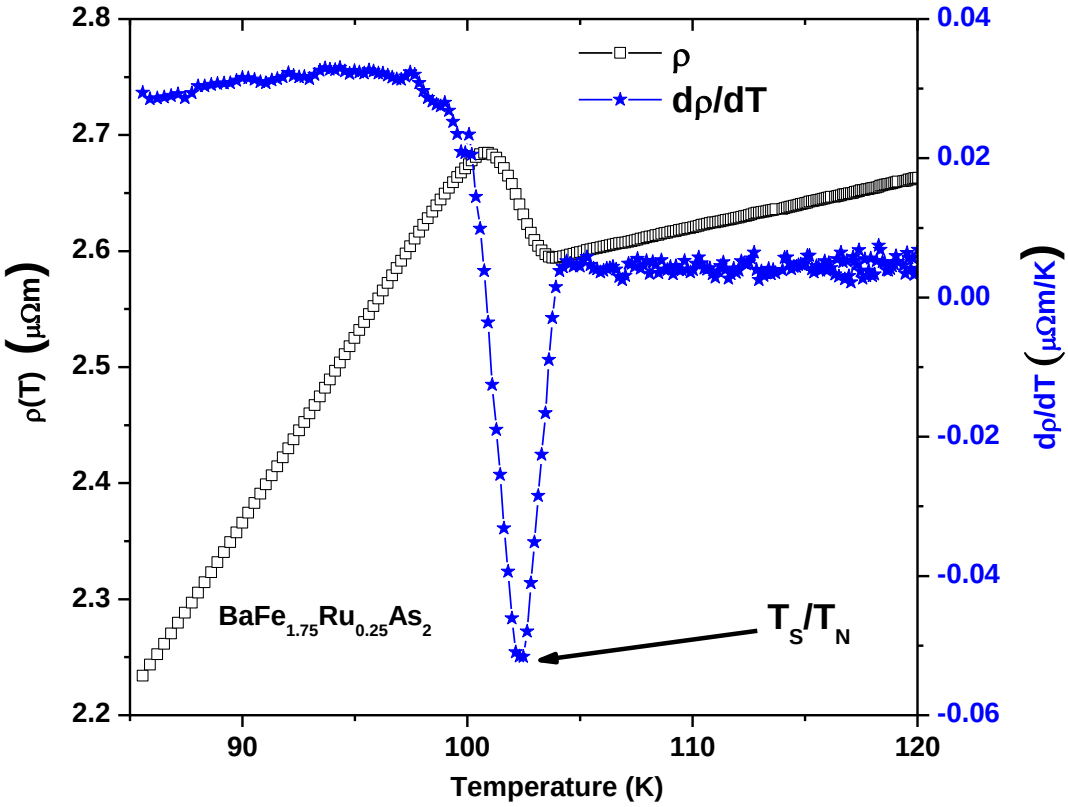

Figure 3.20: Plot of resistivity and derivative of resistivity in the structural-magnetic transition region for x = 0.25 sample. It can be seen that there is only one peak feature associated with the SDW/structural transition pointing to the fact that the structural and magnetic phase transitions occurs at the same temperature in the Ru-substituted samples.

The high resolution single crystal XRD was performed at P08 high resolution XRD beam line of PETRA-3 synchrotron, Hamburg, Germany. Beam energy of 10 keV was used to perform the experiment and the data was collected for 10 seconds in a Mythen line detector. Angle step size was ~0.003^o/step. The change in orthorhombicity indicating a structural phase transition was studied by mounting the single crystals on a six circle diffractometer and the (1, 1, 0) and/or (1, 1, 10) diffraction line was tracked as a function of temperature across the structural-magnetic phase transition. Instead of the (1, 1, 10) line, study of (1, 1, 0) line is better because the prior knowledge of temperature variation of '*c*'-lattice parameter is not required to estimate the orthorhombicity.

Upon cooling the sample below the SDW transition temperature (1, 1, 0) line of tetragonal crystals symmetry (I4/mmm) splits into two lines: (2, 0, 0) and (0, 2, 0) for the orthorhombic (Fmmm) crystal symmetry. Splitting of (1, 1, 0) peak into two (2, 0, 0) and (0, 2, 0) peak of orthorhombic phase is shown in figure 2.4 in Chapter 2. The plots of orthorhombic distortion as a function of temperature for samples containing x = 0.0, 0.1, 0.2, 0.4, 0.5, and 0.55 Ru fraction are shown in figure 3.21 panel (a) to (f). Orthorhombic distortion was not plotted for x = 0.0 and 0.2 samples, since for these samples the (1, 1, 10) peak was followed across the SDW phase transition and thus it was not possible to estimate '*a*' and '*b*' lattice parameters in the absence of reliable '*c*' lattice parameter variation as function of temperature. For all other samples, (1, 1, 0) peak was used to track the orthorhombic phase transition and thus the orthorhombic distortion δ as a function of temperature could be estimated and shown in figure 3.21. It is evident from the figure that the orthorhombic distortion shifts to lower temperatures with increasing Ru fraction in the samples. The degree of orthorhombicity defined as *(a-b)/(a+b)* increases with decrease in temperature for a given Ru content. At the lowest temperature the degree of orthorhombicity decreases with increase in Ru content and for superconducting sample (x = 0.55) the orthorhombic distortion was suppressed. It can be seen from figure 3.21 (f) that unlike the Co- and Rh- doped single crystals [39, 40], change in orthorhombicity below T_C is not discernable for this sample. The structural phase transition was found to be continuous in the case of splitting of (1, 1, 10) line whereas it is very sharp when the transition was tracked using (1, 1, 0) line of tetragonal phase.

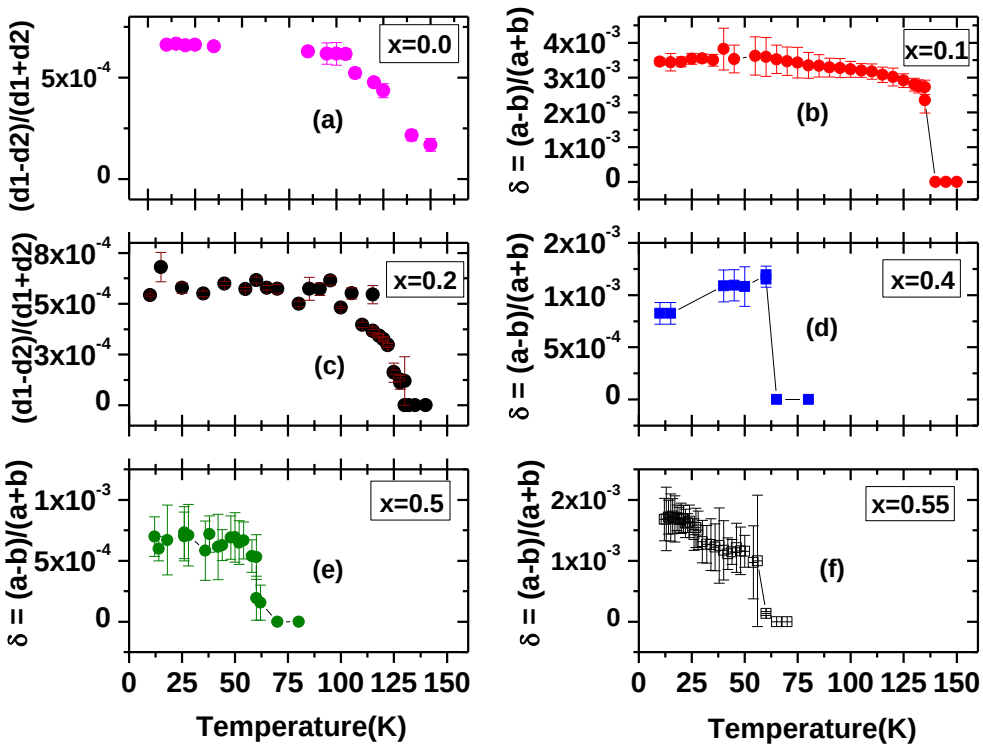

Figure 3.21 (a) to (f): Plots of the orthorhombic distortion as a function of temperature across the structural phase transition in several of the Ru-substituted single crystals. (1, 1, 0) peak of tetragonal crystal structure splits into (2, 0, 0) and (0, 2, 0) peaks of orthorhombic crystal symmetry. The orthorhombicity was estimated by fitting the splitted (2, 0, 0) and (0, 2, 0) peaks to multiple Lorentzian peaks. The structural phase transition was found to shift to lower temperatures with increasing Ru content. In **panel (f),** the orthorhombic distortion in x=0.55 sample; change in orthorhombicity below T_C is not discernable for this sample.

3.8.3 Phase diagram from measurements on single crystals

The T_C vs. x phase diagram proposed on the basis of the anomalies at SDW (T_{SDW}) and superconducting transitions (T_C) in the resistivity and magnetization data was found to be slightly shifted towards lower 'x' values in the case of single crystals reported elsewhere [26, 27]. Since the polycrystalline samples were synthesized at a lower temperature as compared to the single crystals, unreacted RuAs may remain as impurity phase in the case of polycrystalline samples. This may be the reason for the lesser Ru content then the nominal in polycrystalline samples. Subsequently, using the resistivity

versus temperature plots shown in figure 3.19, a new T_C versus '*x*' phase diagram shown in figure 3.22 was proposed. The phase diagram contains points till $x = 0.8$, the highest Ru fraction studied by us. It is seen from the new phase diagram, that the spin density wave and structural transitions gets suppressed faster with increases in Ru content as compared to the suppression rate found in the case of phase diagram obtained using polycrystalline samples.

The new phase diagram for our single crystals matches with the reported phase diagrams for $BaFe_{2-x}Ru_xAs_2$ samples [26, 27]. Ru content was estimated from the Rietveld refinement of the powder diffraction data and T_C/T_{SDW} was estimated from the resistivity versus temperature plots. Paramagnetic (PM), antiferromagnetic (AF) and superconducting (SC) states are marked.

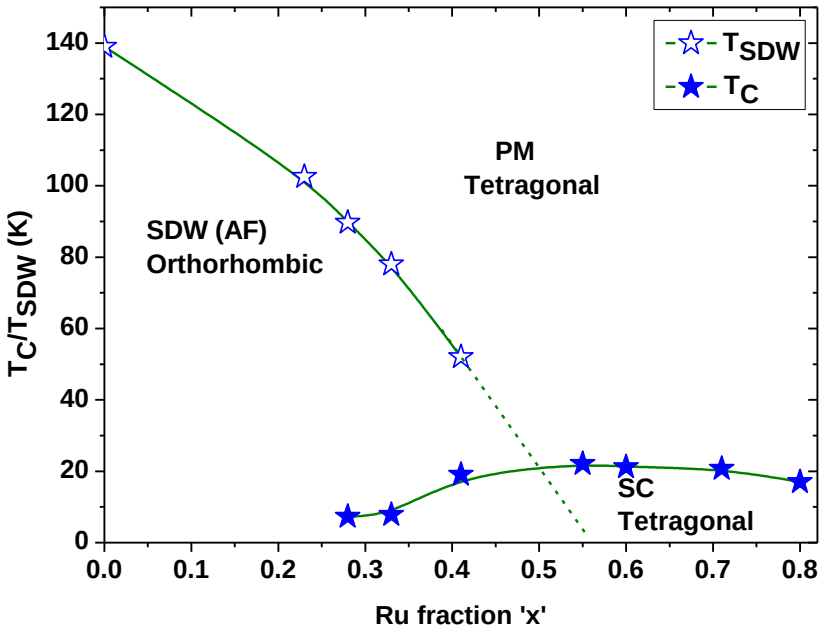

Figure 3.22: T_{SDW}/T_C vs. '*x*' phase diagram for $BaFe_{2-x}Ru_xAs_2$ single crystals estimated from the Rietveld refinement of XRD data and resistive superconducting transitions. The maximum T_C was found for the $x = 0.55$ sample and shows a domelike feature around it. The SDW was found to fully suppress around $x = 0.6$ sample. The above phase diagram matches well with the reported phase diagrams for Ru-substituted $BaFe_2As_2$ system reference [26, 27].

3.9 Conclusions

The first observation of superconductivity in Ru-substituted $BaFe_2As_2$ system is a significant work of the present thesis. Polycrystalline samples of $BaFe_{2-x}Ru_xAs_2$ samples have been synthesized. Having seen superconductivity in the system, through measurements of resistivity and magnetization a *T-x* phase diagram is proposed that indicates that the spin density wave ground state gives way to the occurrence of superconductivity in the range of x = 0.75 to 1.125. Hall coefficient and Mossbauer measurements were employed to characterize the physical properties of these superconductors. Mossbauer results indicate a systematic suppression of the low temperature magnetic state with increase in Ru content. Detailed band structure calculations were performed and an increased electron count and magnetic moment suppression with Ru substitution are borne out by band structure calculations.

Subsequently single crystals were synthesized using high temperature melt growth from stoichiometric precursor powders. Small flat crystals grown with *c*-axis orientation were used to study the effect and correlation of structural parameters with superconductivity in the system. The room temperature powder XRD measurements were performed at INDUS II synchrotron, Indore. From the Rietveld refinement of XRD data, estimations of the cell parameters, As height, As-Fe-As tetrahedra bond angles were performed. From these studies, it is pointed out that the superconductivity in Ru-substituted $BaFe_2As_2$ system is also correlated to its structural properties. Low temperature high resolution crystal XRD measurements were performed at PETRA-3 synchrotron, Germany, to study the structural phase transition in under doped crystals. The Orthorhombic distortion due to tetragonal to orthorhombic transition in pristine

$BaFe_2As_2$ system was found to get suppressed by Ru-substitution. No significant change in the orthorhombic distortion below T_C was discerned in the x = 0.55 sample. A modified phase diagram based on the Rietveld refined Ru fraction '*x*' and T_C/T_{SDW} from the anomalies in the resistivity is established.

References

[1] Kamihara Y, Hiramatsu H, Hirano M, Kawamura R, Yanagi H, Kamiya T and Hosono H 2006 Iron-Based Layered Superconductor: LaOFeP *Journal of the American Chemical Society* **128** 10012-3

[2] Kamihara Y, Watanabe T, Hirano M and Hosono H 2008 Iron-Based Layered Superconductor $La(O_{1-x}F_x)FeAs$ (x = 0.05−0.12) with T_C = 26 K *Journal of the American Chemical Society* **130** 3296-7

[3] Rotter M, Tegel M, Johrendt D, Schellenberg I, Hermes W and Pöttgen R 2008 Spin-density-wave anomaly at 140 K in the ternary iron arsenide $BaFe_2As_2$ *Physical Review B* **78** 020503

[4] Rotter M, Tegel M and Johrendt D 2008 Superconductivity at 38 K in the Iron Arsenide $Ba_{1-x}K_xFe_2As_2$ *Physical Review Letters* **101** 107006

[5] Ni N, Bud'ko S L, Kreyssig A, Nandi S, Rustan G E, Goldman A I, Gupta S, Corbett J D, Kracher A and Canfield P C 2008 Anisotropic thermodynamic and transport properties of single-crystalline $Ba_{1-x}K_xFe_2As_2$ (x=0 and 0.45) *Physical Review B* **78** 014507

[6] Sefat A S, Jin R, McGuire M A, Sales B C, Singh D J and Mandrus D 2008 Superconductivity at 22 K in Co-Doped $BaFe_2As_2$ Crystals *Physical Review Letters* **101** 117004

[7] Patricia L A, Ko Y T C, Jack G, Chiara M P, Jacqueline M C, Gilbert G L and Suchitra E S 2009 Superconductivity Up To 29 K in $SrFe_2As_2$ and $BaFe_2As_2$ at High Pressures *Journal of Physics: Condensed Matter* **21** 012208

[8] Awadhesh M and *et al*. 2009 Pressure-induced superconductivity in $BaFe_2As_2$ single crystal *EPL (Europhysics Letters)* **87** 17004

[9] Huiqian L, Zhaosheng W, Huan Y, Peng C, Xiyu Z and Hai-Hu W 2008 Growth and characterization of $A_{1-x}K_xFe_2As_2$ (A = Ba, Sr) single crystals with x = 0–0.4 *Superconductor Science and Technology* **21** 125014

[10] Vinod K, Satya A T, Sharma S, Sundar C S and Bharathi A 2011 Upper critical field anisotropy in $BaFe_{2-x}Co_xAs_2$ single crystals synthesized without flux *Physical Review B* **84** 012502

[11] Li L J, Luo Y K, Wang Q B, Chen H, Ren Z, Tao Q, Li Y K, Lin X, He M, Zhu Z W, Cao G H and Xu Z A 2009 Superconductivity induced by Ni doping in $BaFe_2As_2$ single crystals *New Journal of Physics* **11** 025008

[12] Ni N, Thaler A, Yan J Q, Kracher A, Colombier E, Bud'Ko S L, Canfield P C and Hannahs S T 2010 Temperature Versus Doping Phase Diagrams For $Ba(Fe_{1-x}TM_x)_2As_2$(TM=Ni,Cu,Cu/Co) Single Crystals *Physical Review B* **82** 24519

[13] Torikachvili M S, Bud'ko S L, Ni N and Canfield P C 2008 Pressure Induced Superconductivity in $CaFe_2As_2$ *Physical Review Letters* **101** 057006

[14] Colombier E, Bud'ko S L, Ni N and Canfield P C 2009 Complete Pressure-Dependent Phase Diagrams For $SrFe_2As_2$ and $BaFe_2As_2$ *Physical Review B* **79** 224518

[15] Kim J S, Blasius T D, Kim E G and Stewart G R 2009 Superconductivity In Undoped Single Crystals Of $BaFe_2As_2$: Field and Current Dependence *Journal of Physics: Condensed Matter* **21** 342201

[16] Duncan W J, Welzel O P, Harrison C, Wang X F, Chen X H, Grosche F M and Niklowitz P G 2010 High Pressure Study of $BaFe_2As_2$ —The Role Of Hydrostaticity And Uniaxial Stress *Journal of Physics: Condensed Matter* **22** 052201

[17] Mizuguchi Y, Hara Y, Deguchi K, Tsuda S, Yamaguchi T, Takeda K, Kotegawa H, Tou H and Takano Y 2010 Anion height dependence of T_C for the Fe-based superconductor *Superconductor Science and Technology* **23** 054013

[18] Ishida K, Nakai Y and Hosono H 2009 To What Extent Iron-Pnictide New Superconductors Have Been Clarified: A Progress Report *Journal of the Physical Society of Japan* **78**

[19] Johnston D 2010 The puzzle of high temperature superconductivity in layered iron pnictides and chalcogenides *Advances in Physics* **59** 803-1061

[20] Kimber S A J, Kreyssig A, Zhang Y-Z, Jeschke H O, Valenti R, Yokaichiya F, Colombier E, Yan J, Hansen T C, Chatterji T, McQueeney R J, Canfield P C, Goldman A I and Argyriou D N 2009 Similarities between structural distortions under pressure and chemical doping in superconducting $BaFe_2As_2$ *Nat Mater* **8** 471-5

[21] Shuai J and et al. 2009 Superconductivity up to 30 K in the vicinity of the quantum critical point in $BaFe_2(As_{1-x}P_x)_2$ *Journal of Physics: Condensed Matter* **21** 382203

[22] Ren Z, Tao Q, Jiang S, Feng C, Wang C, Dai J, Cao G and Xu Z a 2009 Superconductivity Induced by Phosphorus Doping and Its Coexistence with Ferromagnetism in $EuFe_2(As_{0.7}P_{0.3})_2$ *Physical Review Letters* **102** 137002

[23] Klintberg L E, Goh S K, Kasahara S, Nakai Y, Ishida K, Sutherland M, Shibauchi T, Matsuda Y and Terashima T 2010 Chemical Pressure and Physical Pressure in $BaFe_2(As_{1-x}P_x)_2$ *Journal of the Physical Society of Japan* **79** 12

[24] Sharma S, Bharathi A, Chandra S, Reddy V R, Paulraj S, Satya A T, Sastry V S, Gupta A and Sundar C S 2010 Superconductivity in Ru-substituted polycrystalline $BaFe_{2-x}Ru_xAs_2$ *Physical Review B* **81** 174512

[25] Schnelle W, Leithe-Jasper A, Gumeniuk R, Burkhardt U, Kasinathan D and Rosner H 2009 Substitution-induced superconductivity in $SrFe_{2-x}Ru_xAs_2$ ($0 \leq x \leq 2$) *Physical Review B* **79** 214516

[26] Rullier-Albenque F, Colson D, Forget A, Thuéry P and Poissonnet S 2010 Hole and electron contributions to the transport properties of $Ba(Fe_{1-x}Ru_x)_2As_2$ single crystals *Physical Review B* **81** 224503

[27] Thaler A, Ni N, Kracher A, Yan J Q, Bud'Ko S L and Canfield P C 2010 Physical and magnetic properties of $Ba(Fe_{1-x}Ru_x)_2As_2$ single crystals *Physical Review B* **82** 014534

[28] Ni N, Tillman M E, Yan J Q, Kracher A, Hannahs S T, Bud'ko S L and Canfield P C 2008 Effects Of Co Substitution On Thermodynamic And Transport Properties And Anisotropic H_{C2} In $Ba(Fe_{1-x}Co_x)_2As_2$ single crystals *Physical Review B* **78** 214515

[29] Toby B 2001 EXPGUI, a graphical user interface for GSAS *Journal of Applied Crystallography* **34** 210-3

[30] Zentile C L, Gillette J, Sebastian S E and Cooper J R 2009 Measurement and analysis of the Hall effect of A-Fe_2As_2 single crystals with A = Ba, Ca or Sr. In: *arXiv: 0911.1259*,

[31] Schwarz K, Blaha P and Madsen G K H 2002 Electronic structure calculations of solids using the WIEN2k package for material sciences *Computer Physics Communications* **147** 71-6

[32] Singh D J 2008 Electronic structure and doping in $BaFe_2As_2$ and LiFeAs: Density functional calculations *Physical Review B* **78** 094511

[33] Huang Q, Qiu Y, Bao W, Green M A, Lynn J W, Gasparovic Y C, Wu T, Wu G and Chen X H 2008 Neutron-Diffraction Measurements of Magnetic Order and a Structural

Transition in the Parent $BaFe_2As_2$ Compound of FeAs-Based High-Temperature Superconductors *Physical Review Letters* **101** 257003

[34] Brand R A 1990 NORMOS. (Universitaaet Duisburg)

[35] Nowik I and Felner I 2009 Mössbauer spectroscopy studies of oxypnictides superconductors *Physica C: Superconductivity* **469** 485-90

[36] Felner I, Nowik I, Lv B, Tapp J, Tang Z and Guloy A 2009 Determination of foreign phases in Fe–As based superconducting systems *Hyperfine Interact* **191** 61-5

[37] Vinod K, Sharma S, Satya A T, Sundar C S and Bharathi A 2012 Phase diagram of Ru doped $BaFe_2As_2$ *AIP Conference Proceedings* **1447** 889-90

[38] Hammersley A P, Svensson S O, Hanfland M, Fitch A N and Hausermann D 1996 Two-dimensional detector software: From real detector to idealised image or two-theta scan *High Pressure Research* **14** 235-48

[39] Nandi S, Kim M G, Kreyssig A, Fernandes R M, Pratt D K, Thaler A, Ni N, Bud'ko S L, Canfield P C, Schmalian J, McQueeney R J and Goldman A I 2010 Anomalous Suppression of the Orthorhombic Lattice Distortion in Superconducting $Ba(Fe_{1-x}Co_x)_2As_2$ Single Crystals *Physical Review Letters* **104** 057006

[40] Kreyssig A, Kim M G, Nandi S, Pratt D K, Tian W, Zarestky J L, Ni N, Thaler A, Bud'Ko S L, Canfield P C, McQueeney R J and Goldman A I 2010 Suppression of antiferromagnetic order and orthorhombic distortion in superconducting $Ba(Fe_{0.961}Rh_{0.039})_2As_2$ *Physical Review B* **81** 134512

[41] Kasahara S, Shibauchi T, Hashimoto K, Ikada K, Tonegawa S, Okazaki R, Shishido H, Ikeda H, Takeya H, Hirata K, Terashima T and Matsuda Y 2010 Evolution from non-Fermi- to Fermi-liquid transport via isovalent doping in $BaFe_2(As_{1-x}P_x)_2$ superconductors *Physical Review B* **81** 184519

[42] Kim M G, Pratt D K, Rustan G E, Tian W, Zarestky J L, Thaler A, Bud'ko S L, Canfield P C, McQueeney R J, Kreyssig A and Goldman A I 2011 Magnetic ordering and structural distortion in Ru-doped $BaFe_2As_2$ single crystals studied by neutron and x-ray diffraction *Physical Review B* **83** 054514

Chapter 4

Upper Critical Field of $BaFe_{2-x}Ru_xAs_2$ Superconductors

This chapter presents the anisotropy in upper critical field ($\mu_0 H_{C2}$) as a function of temperature for various Ru-substitutions in $BaFe_2As_2$ single crystals. $\mu_0 H_{C2}$ is estimated from the shift of resistive transition temperature under different fields. Based on the in-field resistance measurements $\mu_0 H$-T phase diagrams including irreversibility fields of superconducting single crystals of $BaFe_{2-x}Ru_xAs_2$ are presented. The anisotropy in the upper critical field shows anomalous temperature dependence with a peak near T_C. The peak in anisotropy was also found to depend upon the Ru concentration.

4.1 Introduction

The upper critical field ($\mu_0 H_{C2}$) is one of the fundamental characteristics of a type II superconductor. It provides useful insights into the pair breaking mechanisms and underlying electronic structure in a superconductor [1]. Other important parameters like coherence length and mass anisotropy ratio can be derived using the upper critical field for the different crystallographic orientation like along *ab-plane* or *c-axis.* Since the iron-pnictide (Fe-Pn) based superconductors have layered structure (see chapter 1) it can be expected that their electronic structure are anisotropic [2].

Soon after the discovery of the iron based superconductors, several experimental studies on in-field transport measurements were performed to ascertain the upper critical field ($\mu_0 H_{C2}$) value and the associated anisotropy [3-7]. These studies have been motivated by the need for an understanding of superconductivity and their potential applications. It was found that the iron based superconductors possess large upper critical field (~ 40 – 50 T) [8]. Estimations using single band Werthamer, Helfand and Hohenberg (WHH) model [9] and the slope of $\mu_0 H$-T curves at $T = T_C$, give a value as high as 100 T-300 T [10-12]. For many of the iron-arsenide based superconductor families, $\mu_0 H_{C2}(T)$ shows an upward curvature implying a multiband superconductivity in the system [1, 6, 13-15]. In contrast to HTSCs which show very large anisotropy, the upper critical fields of iron based superconductors are found to be temperature dependent and have very low values of anisotropies. The anisotropy ratio $\gamma = \frac{H_{C2}^{ab}}{H_{C2}^{c}}$ has been found to decrease with the decrease in the temperature and the 122 type of FeAs superconductors become nearly isotropic at low temperatures [7, 13, 16, 17]. Similar anisotropy ratio of upper critical field was also found using bulk specific heat measurements on electron doped $Ba(Fe_{1-x}Co_x)_2As_2$ superconductors [18]. A nearly isotropic shape of upper critical field was found for the hole doped $(Ba_{1-x}K_x)Fe_2As_2$ and the orbital limiting pair breaking was found to be dominant at all the field angles [17]. All these studies of upper critical field and its anisotropy were mostly performed in charge doped FeAs systems. As described in chapter 3, Ru-substituted $BaFe_2As_2$ is a new superconducting system without charge doping. A systematic study of the upper critical field and anisotropy ratio as a function of Ru fraction in $BaFe_{2-x}Ru_xAs_2$ superconductor is required to see the effect of

Ru on the anisotropic upper critical field in isovalent substituted $BaFe_2As_2$ superconductors.

In this chapter we present in-field anisotropic electrical resistance measurements on single crystalline Ru-substituted $BaFe_2As_2$ superconductors in fields up to 12 T applied parallel and perpendicular to *c-axis* of the crystals. Resistivity measurements were performed for samples with different Ru concentration to cover the full T_C vs. x phase diagram, described in chapter 3. Investigations of the upper critical field $\mu_0 H_{C2}$, and its anisotropy in single crystals of Ru substituted $BaFe_{2-x}Ru_xAs_2$ superconductors are presented as a function of Ru-fraction. Irreversibility fields ($\mu_0 H_{irr}$) [19] at which critical current density due to flux pinning vanishes were estimated and presented in the $\mu_0 H$-T plots.

4.1.1 Pair breaking induced by magnetic field

It is well known [20] that the application of external magnetic field destroys the Cooper pair bound state by following two processes: (i) The orbital pair breaking due to the opposite Lorentz force acting on the two bounded electrons having opposite momenta, known as orbital limit and (ii) The Pauli paramagnetic pair breaking, as a result of the Zeeman effect which aligns the spins of two electrons with the applied field direction, known as Pauli paramagnetic limit.

In the case of type II superconductors, the temperature and impurity dependence of the upper critical field is explained by Werthamer, Helfand and Hohenberg (WHH) model [9]. The effect of both Pauli paramagnetic pair breaking and spin-orbital scattering

is included in this model. In the dirty limit, orbital effects limited upper critical field at zero temperature is given by [9]

$$\mu_0 H_{C2}^{orb}(0) = -0.69 T_C \left(\frac{d\mu_0 H_{C2}}{dT}\right)|_{T=T_C} \qquad (4.1)$$

In the case of unconventional superconductors like FeAs based superconductors the upper critical fields are expected to be anisotropic since the distinctive hole and electron Fermi surfaces are known to be responsible for superconductivity [21]. The electronic structure of the normal state of these superconductors that is anisotropic leads to anisotropy in the superconducting properties. The anisotropy ratio γ [22] is defined as $\gamma = \sqrt{\frac{m_c}{m_{ab}}} = \frac{H_{C2}^{ab}}{H_{C2}^{c}}$, where m_{ab} and m_c are the effective masses of electrons for the in-plane and out of plane motion, respectively. The knowledge of anisotropy is very important for both understanding superconductivity and for the technological applications of superconductors.

4.2 In-field resistivity measurements

Resistance as a function of temperature under the applied magnetic fields up to 12 T was measured for the superconducting single crystals of $BaF_{2-x}Ru_xAs_2$ (x=0.5, 0.55, 0.6, 0.71, 0.8). These samples span the T_C vs. x phase diagram discussed in chapter 3. Measurements were performed in the Van-der Pauw geometry for magnetic field applied parallel and perpendicular to the crystallographic c-axis. Proper care was taken to measure the resistance with current flowing perpendicular to field direction. T_C for all the samples was estimated using the criterion that the value of resistance falls to 90% of its normal state value prior to superconducting transition.

4.2.1 Anisotropic upper critical field of $BaFe_{1.5}Ru_{0.5}As_2$

The plots of resistance as a function of temperature under magnetic fields up to 12 T applied perpendicular and parallel to *c*-axis are shown in figure 4.1(a) and 4.1(b) respectively.

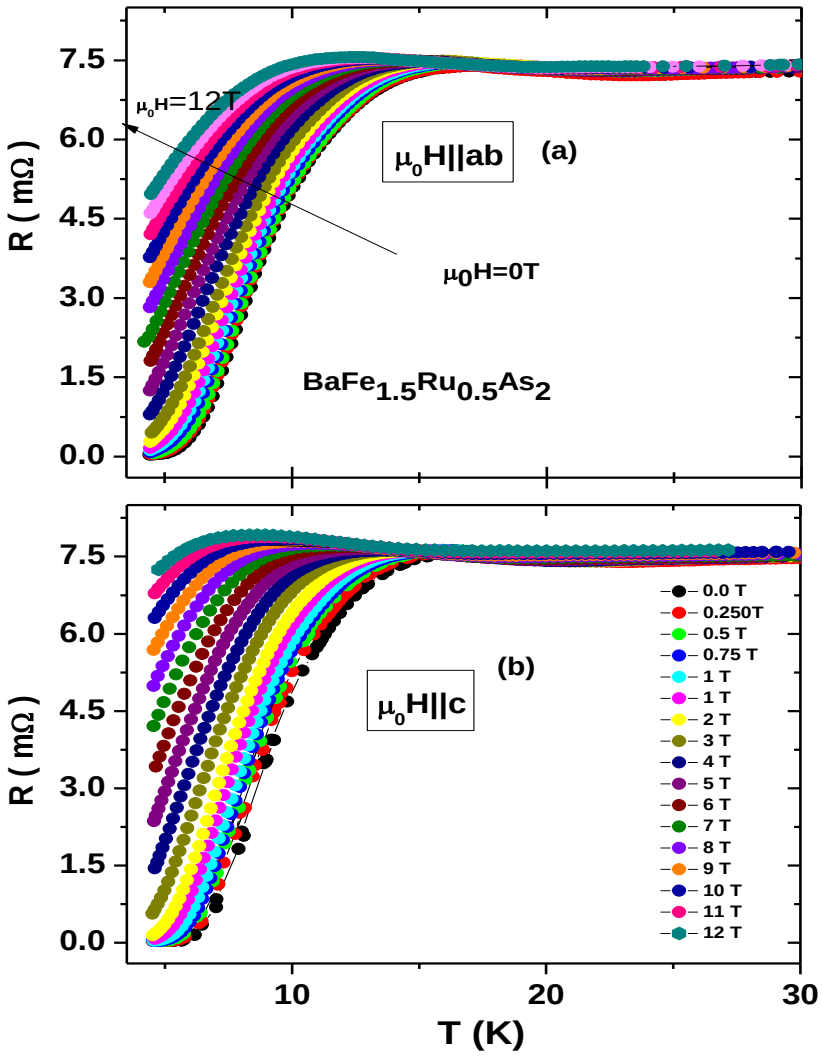

Figure 4.1 (a): Resistance vs. temperature plots for magnetic fields up to 12 T applied parallel to *ab*-plane of the crystals. Transitions are seen to become broad with increase in the field. A small positive MR can be observed in the normal state along with a hump that becomes more pronounced with the increasing field. **(b):** *R(T)* plots under fields applied parallel to c-axis. The broad hump prior to superconducting transition is more pronounced in this direction.

A broad peak prior to the onset of superconducting transition was observed in all the *R(T)* plots. The peak was seen to become more prominent with increasing field and a positive magneto-resistance (MR) was found in normal state of the single crystalline samples. Transition temperature of the superconducting compound $BaFe_{1.5}Ru_{0.5}As_2$, as estimated by the 90% fall in normal state resistance criterion, was found to be 11.8 K with a transition width of around 6-7 K. The resistive transitions to superconducting state were found to shift to lower temperatures remaining nearly parallel to each other. A field induced broadening of the transitions can be observed in both the field directions, and the resistive transitions in $H||c$ direction show more in-field broadening than $H||ab$ direction.

The temperature dependence of upper critical field in the *ab-plane* and along *c-axis* is shown in main panel of figure 4.2. Upper critical field along *c-axis* shows an upward curvature whereas $\mu_0 H_{C2}$ in *ab-plane* shows nearly linear temperature dependence after an initial upward curvature at high temperatures. This upward curvature of $\mu_0 H_{C2}(T)$, also observed for other superconductors like MgB_2 [22], $Ba(Fe,Co)_2As_2$ [6] and $(Sr,Eu)(Fe,Co)_2As_2$ [1], has been explained within multiband BCS model by taking into account the inter- and intra-band scattering interactions [22]. We refrain from using the single band WHH extrapolation to estimate $\mu_0 H_{C2}(0)$, since the FeAs based superconductors are multiband systems and the values obtained are over-estimated. To get the correct value of zero temperature upper critical field using the WHH model fitting, experiments under fields as high as 40-60 T are required. The unavailability of the low temperature data (below 4 K) restricted us from estimating irreversibility field for this compound.

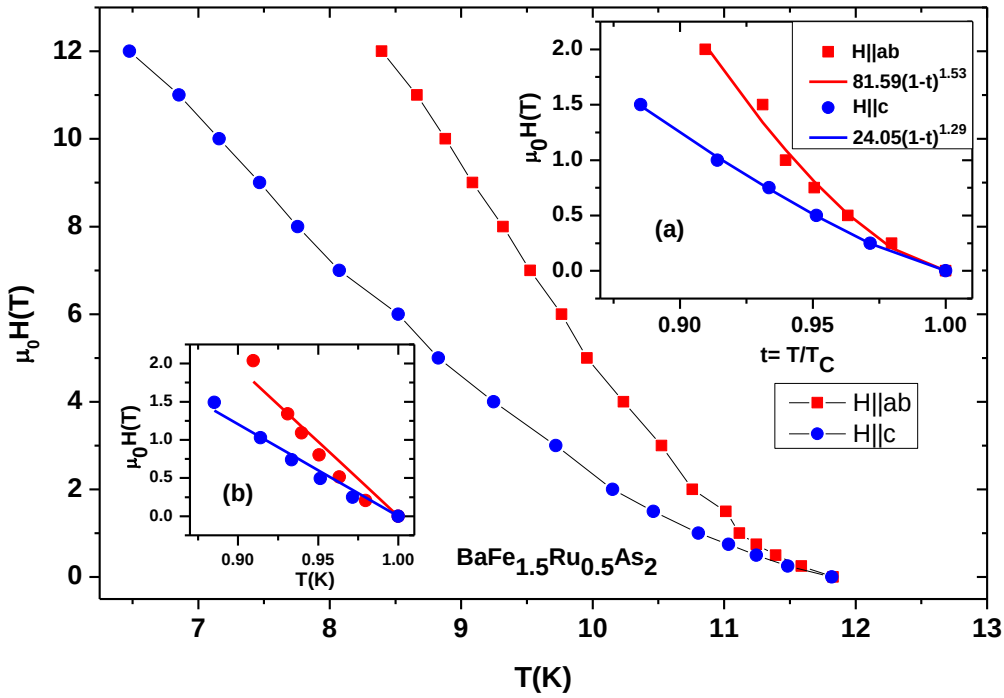

Figure 4.2: The temperature dependence of upper critical fields in the *ab-plane* and along *c-axis* are shown in main panel. Upper critical field in both the directions show a negative curvature in the high temperature regime near to T_C. Later at low temperatures, the upper critical field in *ab-plane* shows nearly linear temperature dependence but the upper critical field along *c*-axis shows negative curvature up to the highest field studied. **Inset (a):** shows the fitting of upper critical field data near T_C to $H_0(1-t)^n$, **(b):** $H_{C2}(T)$ fit to (T_C-T).

It was shown by Gurevich [23], that in the case of multiband superconductors like FeAs based superconductors, the upper critical field close to T_C show a linear dependence on $(T_C - T)$ i.e., $H_{C2} \propto (T_C - T)$, changing to $H_{C2} \propto \sqrt{(T_C - T)}$ as T is decreased. It is seen from the inset (b) that the linear variation $H_{C2} \propto (T_C - T)$, provides a reasonable fit. Inset (a) of figure 4.2 shows the fit to $H_0(1-t)^n$, , that appears to give a better fit with an exponent n = 1.5 and 1.3 for $H||ab$ and $H||c$ direction respectively.

In the multiband superconductors, there exist strong differences in the pairing interactions for different Fermi-surface sheets and diffusion constant anisotropies for different bands, these influence the in-plane $\mu_0 H_{C2}$ in a different way at high and low

temperatures. This results in a temperature dependent $\mu_0 H_{C2}$ anisotropy [24]. The temperature variation of anisotropy ratio $\left(\gamma = \frac{H_{C2}^{ab}}{H_{C2}^{c}}\right)$ of upper critical field, plotted in figure 4.3, shows a decrease with decrease in the temperature. This temperature dependence is qualitatively similar to most of the FeAs based superconductors [5, 17, 25]. An unusual feature of $\gamma(t)$ plot is a peak near 0.9-0.95T_C, which is consistent with theoretical results for the two band model [24] that expect to have the peak in anisotropy vs. temperature at 0.9T_C.

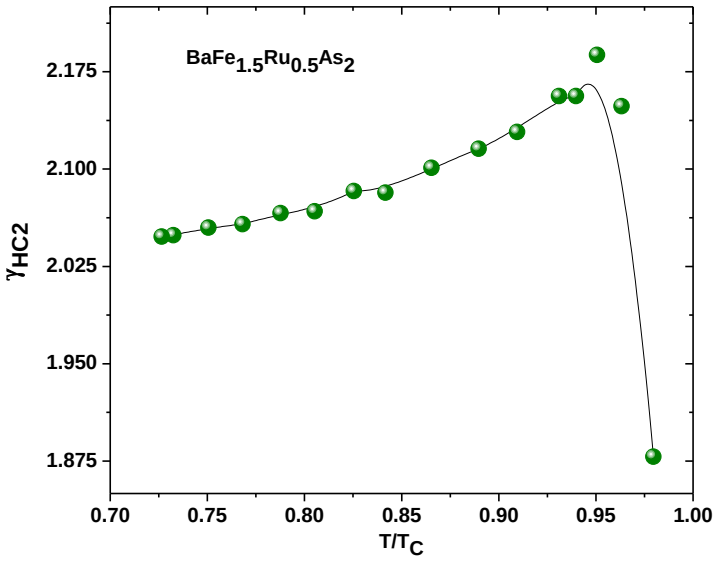

Figure 4.3: Anisotropy ratio as a function of reduced temperature T/T_C. Anisotropy in upper critical field shows a peak near 0.9T_C: a known feature of multi-band systems. It can also be seen that the anisotropy decreases towards 1 with decrease in temperature.

4.2.2 Upper critical field and irreversibility field of $BaFe_{1-x}Ru_xAs_2$

In the following, we present the results of the in-field transport measurements and estimation of upper critical field on other single crystals with varying Ru content. *R(T)* plots of resistive transitions to superconducting state under different magnetic fields for

x = 0.55 sample are shown in figure 4.4 (a) and (b). The magnetic field was applied parallel to *ab-plane* and *c-axis*. The zero-field superconducting transition temperature estimated using criterion of 90% fall in resistance from its normal state value just prior to transition, is 22.1 K from both the set of measurements. The field induced broadening of the resistive transitions is less in both the directions of applied field and the $R(T)|_H$ plots shift to lower temperature remaining parallel to each other. The shift of *R(T)* transitions towards lower temperatures is seen to be more in the case of *c-axis* oriented field direction and thus anisotropy in the upper critical field is clearly visible from figure 4.4. No magneto-resistance was observed in normal state of the compound.

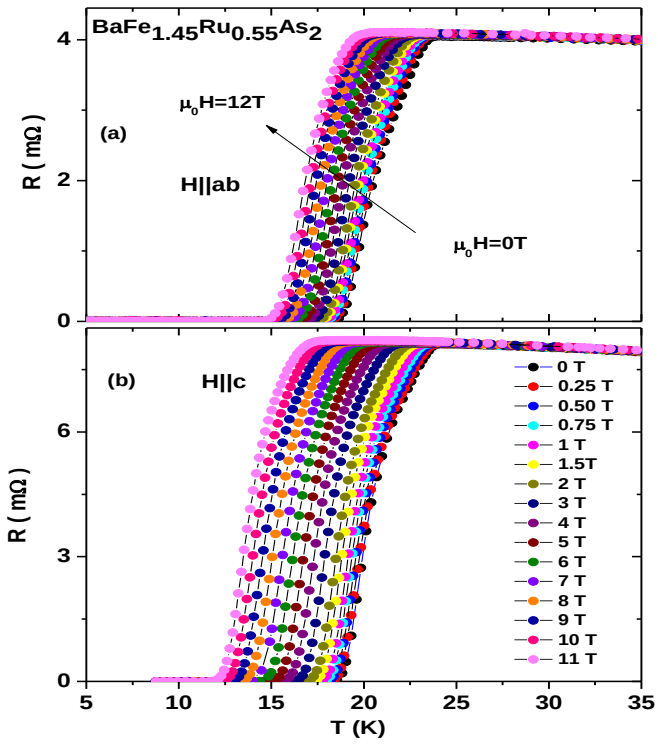

Figure 4.4 (a): Superconducting transitions measured using resistance as a function of temperature up to 75 K (shown up to 45 K) in external magnetic fields applied along *ab-plane*. Transitions shift parallel towards low temperature with increasing field. No magneto-resistance was observed in normal state. **(b):** transitions in external fields applied along *c-axis* show a larger shift towards lower temperatures as compared to that along *ab-plane*. No magneto-resistance in normal state was observed in any field direction.

In figure 4.5, upper critical field in *ab-plane* and along *c-axis* are presented. Here again an upward (negative) curvature in upper critical field for both the directions was observed near to T_C but as the temperature is lowered further, the upper critical fields show a nearly linear behavior in T.

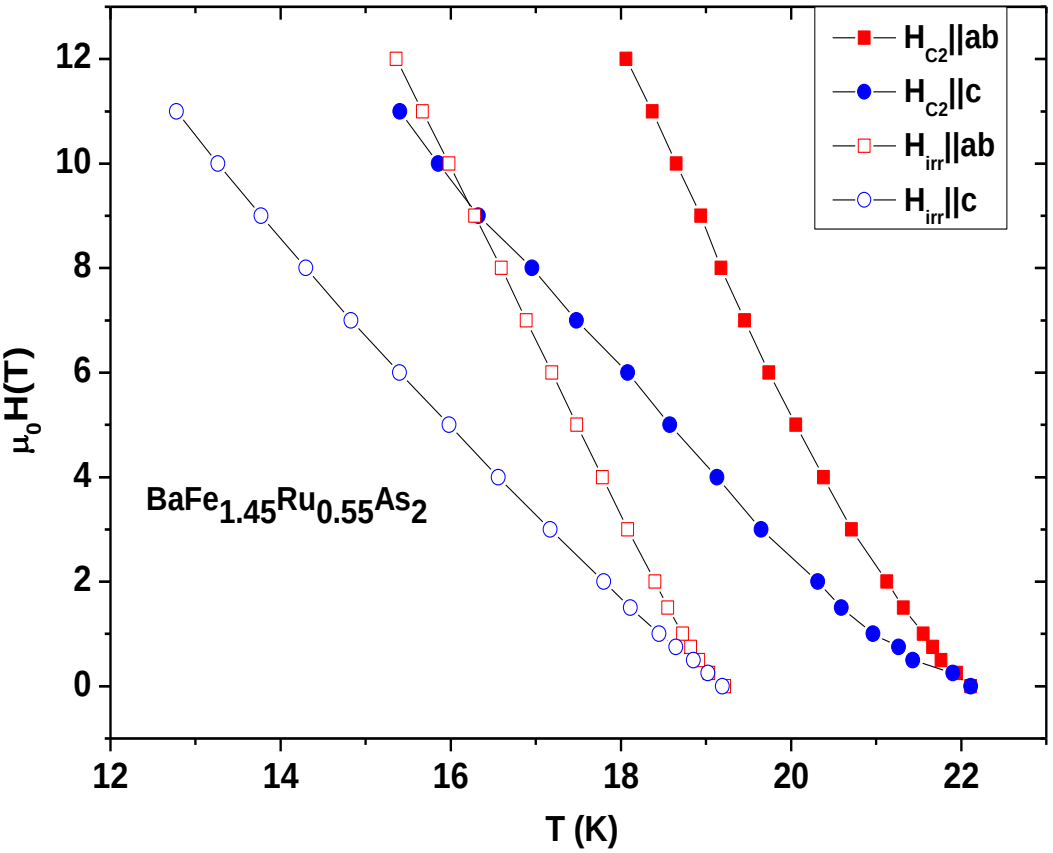

Figure 4.5: Upper critical field as a function of temperature estimated along *ab-plane* and *c*-direction (solid symbols). In both the directions $\mu_0 H_{C2}(T)$ shows upward curvature near T_C but becomes nearly linear in T at low temperatures. Open symbols show the variation of irreversibility field along two directions. A substantial difference in H_{C2} and H_{irr} is observed.

Figure 4.5 also presents the variation of irreversibility field ($\mu_0 H_{irr}$) as a function of temperature for the two perpendicular field directions. The irreversibility field curves were defined at 10% of R_n [19] i.e $R(T,H_{irr}) = 0.1R_n$; R_n being the normal state resistance. A very small difference between upper critical fields and irreversibility fields was

observed and thus a high pinning potential and large critical current density are expected in this system. Upper critical field in the vicinity of the transition temperature fits to the equation $H_0(1-t)^n$, with n=1.26 along *ab-plane* and 1.35 along *c-axis*. The fitted values of $\mu_0 H_0(ab)$ and $\mu_0 H_0(c)$ are 98.40 T and 57.05 T respectively.

The in-field resistance as a function of temperature was also measured for $BaFe_{2-x}Ru_xAs_2$ (x = 0.6, 0.71, 0.8) single crystals and the plots of *R(T)* under different magnetic fields are presented in figure 4.6 (a)-(f) . T_C ~ 21 K, 20.7 K and 20.4 K were found for x = 0.6, 0.71, 0.8 samples respectively. Temperature variation of upper critical field along *ab*-plane and c-axis for x=0.6, 0.71, 0.8 sample are shown in figure 4.7 (a)-(f) respectively (filled circles). It is noticed that the upper critical field along *c*-axis for all these samples show a negative curvature in the full temperature range studied.

The irreversibility field along *ab-plane* and *c-axis* as shown in figure 4.7 (a), (c) and (e) (open circles) for x=0.6, 0.71 and 0.8 samples, are found to be very close to upper critical field in the respective field directions. Figure 4.7 (b) (d) and (e) shows the fitting of upper critical field as a function of reduced temperature to the function $H_0(1-t)^n$. The value of exponent '*n'* is found to vary between 1.18 to 1.34 for magnetic field applied along *ab-plane* and 1.17 to 1.37 for field along *c-axis*. For x=0.71 sample, the value of 'n' is 1.07 for field along *ab-plane*. The separation of the irreversibility field from the upper critical field can be seen to decrease as the Ru fraction increases in the samples.

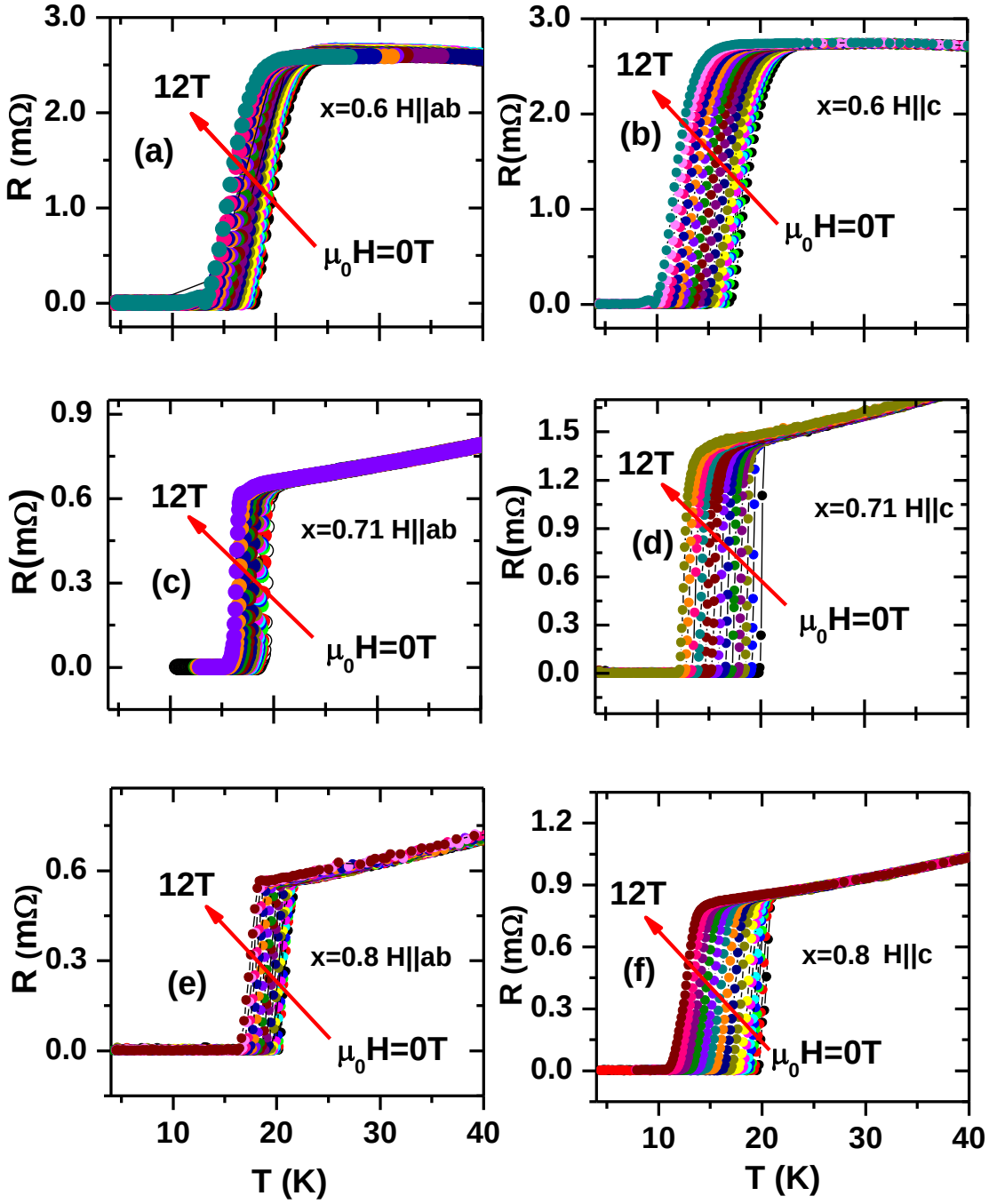

Figure 4.6 (a), (b): Resistance vs. temperature plots for *x*=0.6 sample shows no broadening of the superconducting transition under fields up to 12 T applied parallel *to ab-plane* and *c-axis*. The shift of superconducting transitions for *H||c* is more than when the field is oriented along *ab-plane*. **(c), (d):** *R(T)* plots for *x*=0.71 sample also show similar behavior and zero magneto-resistance in the normal state. No features associated with spin density wave were observed. **(e), (f):** In-field resistance as a function of temperature for *x*=0.8 sample.

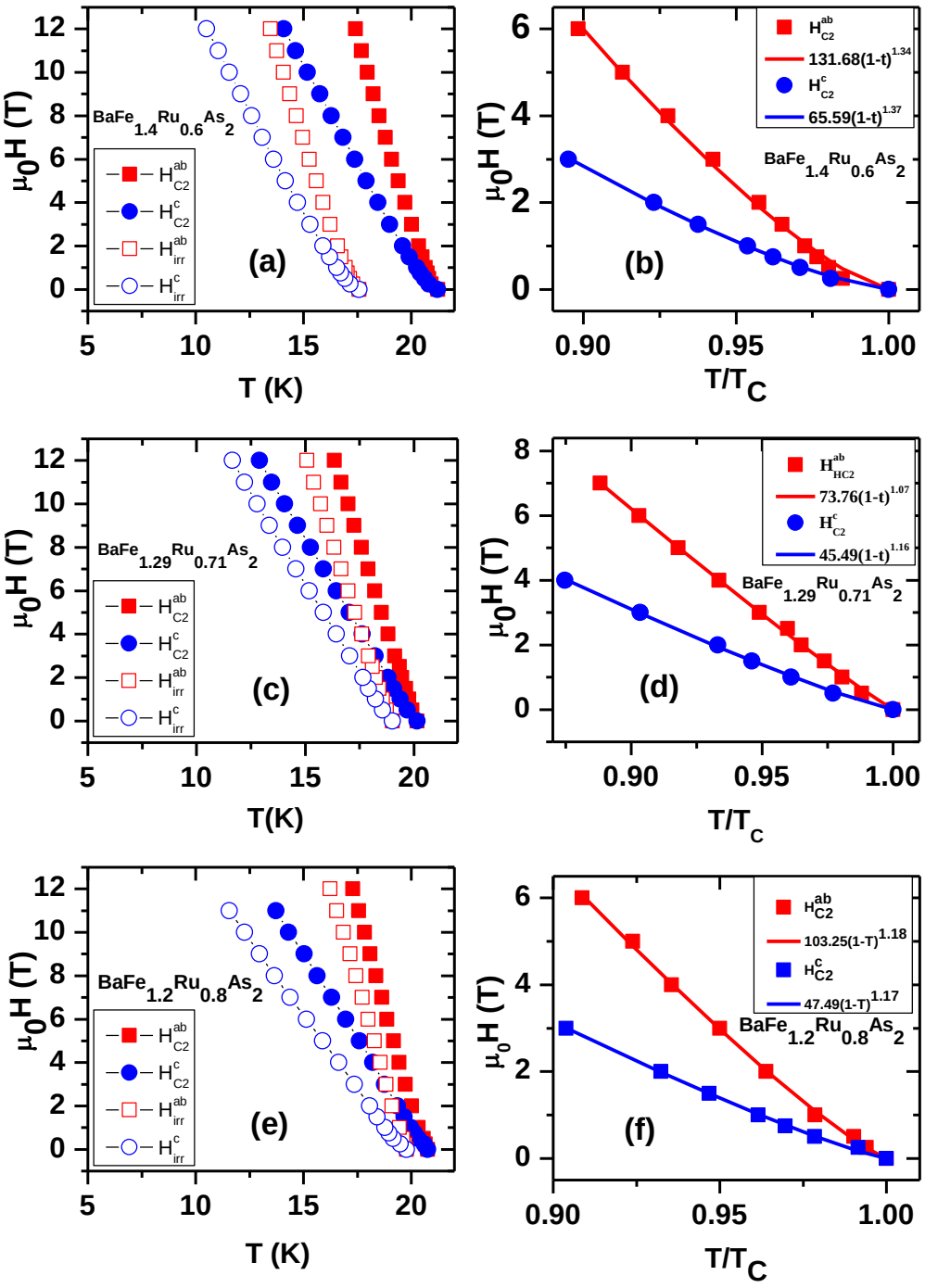

Figure 4.7 (a), (c), (e): The temperature variation of $\mu_0 H_{C2}$ and $\mu_0 H_{irr}$ for x=0.6, 0.71, 0.8 sample, estimated using 90% and 10% of R_n criterion. It can be noticed that the difference between $\mu_0 H_{C2}$ and $\mu_0 H_{irr}$ decreases as the Ru fraction increases. **(b), (d), (f):** Fitting of upper critical field near T_C to $H_0(1-t)^n$. The values of H_0 are found to increase with Ru fraction but the exponent n remains nearly same ~1.17-1.3 for all the samples in both the field directions.

4.3 Anisotropy in upper critical field

From the above results of upper critical fields in two perpendicular directions, the anisotropy in upper critical field has been evaluated and the results are shown in figure 4.8 (a) to (d) for x=0.55, 0.6, 0.71 and 0.8 samples respectively. Even though, the average value of the anisotropy remains nearly 2.2-2.3 but the peak in the anisotropy around $0.9T_C$ can be seen to become more pronounced for x=0.71 and 0.8 samples. Table 4.1 presents the comparison of T_C, $\left(\frac{dH_{C2}}{dT_C}\right)$ along both the field directions, and anisotropy ratio (γ) for all the Ru substituted samples studied.

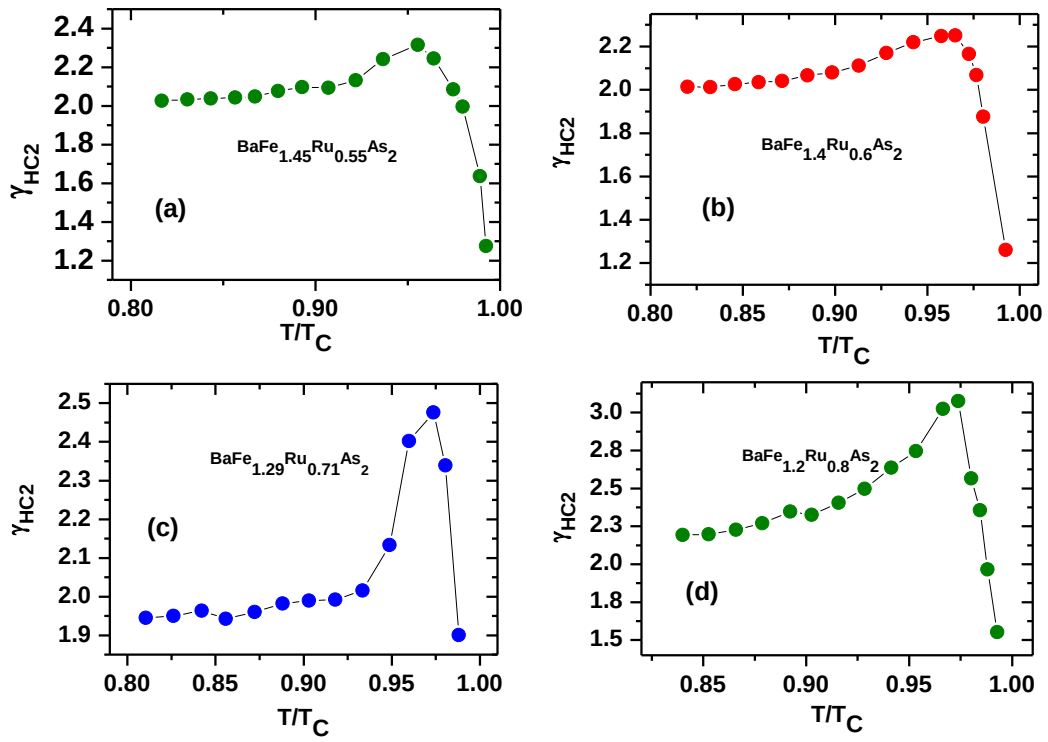

Figure 4.8 (a) (b) (c) (d): Temperature variation of the anisotropy ratio of upper critical fields for the x=0.6, 0.71, 0.8 single crystals. Although the average value of the anisotropy remains nearly 2.2-2.3 but the peak in the anisotropy around $0.9T_C$ can be seen to become more pronounced for x=0.71 and 0.8 samples. The peak anisotropy is highest for x=0.8 sample with a value 3.04 at $0.95T_C$. The anisotropy ratios for the over-substituted single crystals decrease with decreasing temperature and settles around 2 for the minimum temperature studied.

Ru fraction (x)	T_C (K)	$\left(\frac{dH_{C2}}{dT_C}\right)^{ab}_{T_C}$ (T/K)	$\left(\frac{dH_{C2}}{dT_C}\right)^{c}_{T_C}$ (T/K)	$\gamma_{mass} = \frac{H_{C2}^{ab}/dT}{H_{C2}^{c}/dT}$	$\gamma = \frac{H_{C2}^{ab}}{H_{C2}^{c}}$ (at $0.95T_C$)
0.5	11.8	-3.7 ± 0.1	-2.31 ± 0.09	1.6	2.2
0.55	22.1	-3.46 ± 0.05	-1.85 ± 0.02	1.9	2.3
0.6	21.2	-3.34 ± 0.03	-1.82 ± 0.01	1.8	2.2
0.71	20.7	-3.19 ± 0.02	-1.26 ± 0.04	2.5	2.1
0.8	20.4	-3.51 ± 0.05	-1.59 ± 0.01	2.2	2.6

Table 4.1: Superconducting parameters of different Ru fraction containing $BaFe_{2-x}Ru_xAs_2$ single crystals. The anisotropy in average mass of electrons, estimated by the ratio of slopes of upper critical field shows a maximum value of 2.5 for x=0.71 sample.

Figure 4.9 (a) shows the plots of the variation of the slope $\left(\frac{dH_{C2}}{dT_C}|_{T_C}\right)$ near the transition temperature, as a function of Ru fraction in the single crystals. It is seen from the figure that the slope for both the field directions goes through a maximum at Ru fraction of 0.71, higher than the optimal substitution ~ 0.55. It is known [26] that the value of $-dH_{C2}^{ab}/dT$ is proportional to $(m_{ab}.m_c)^{1/2}$, while $-dH_{C2}^{c}/dT$ is proportional to m_{ab}, (m_c and m_{ab} are the electron effective mass along *c-axis* and in *ab-plane*). Therefore the ratio of the slopes determined by $\frac{dH_{C2}^{ab}/dT}{dH_{C2}^{c}/dT}$ can reliably show the anisotropy of the averaged electron mass near the transition temperature [26]. Figure 4.9 (b) presents the anisotropy in the average mass of electrons as a function of Ru fraction in $BaFe_{2-x}Ru_xAs_2$ superconductors. It is clear from figure 4.9 (b) that the mass anisotropy in the Ru-substituted $BaFe_2As_2$ system is ~2. The anisotropy goes through a maximum value of around 2.5 for *x*=0.71 sample which is marginally higher than the optimal Ru fraction.

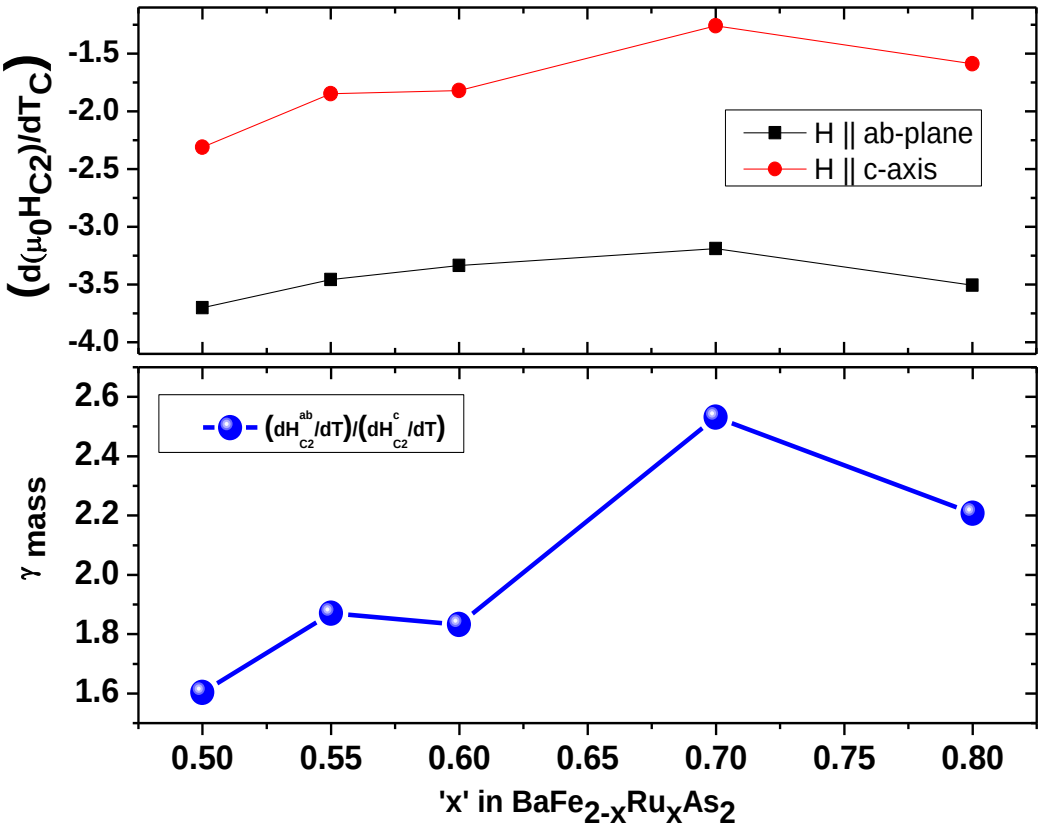

Figure 4.9 (a): The variation of slope of $\mu_0 H_{C2}(T)$ plots along *ab-plane* and *c-axis* near the transition temperature, as a function of Ru fraction in the single crystals. It is evident from the figure that the slope for both the field direction goes through a maximum around x=0.71 Ru fraction which is marginally higher than the optimal substitution. **(b):** Anisotropy in the average mass of electrons as a function of Ru fraction in $BaFe_{2-x}Ru_xAs_2$ superconductors. It is clear from figure that the mass anisotropy in the Ru substituted $BaFe_2As_2$ system is ~2. The anisotropy goes through a maximum value of around 2.5 for x=0.71 sample which is higher than the optimal Ru fraction.

Similar peak in anisotropy was reported in the anisotropy of Co-doped $BaFe_2As_2$ [25]. It is interesting to see that the anisotropy in Ru-doped system is similar to that of the Co-doped system, since the Co-doped sample has larger electron Fermi pocket whereas Ru-doped system is close to the case of isovalent doping and is a unique system without charge doping but double the number of both carriers with increased mobility.

4.4 Conclusions

The upper critical fields for the $BaFe_{2-x}Ru_xAs_2$ superconducting single crystals were studied using the in-field transport measurements. A small and temperature dependent anisotropy (γ~2-3) was found in the Ru-substituted $BaFe_2As_2$ system of superconductors, similar to other doped $BaFe_2As_2$ superconductors. The temperature dependence of anisotropy was found to be nearly independent of the Ru fraction but the peak in the anisotropy near $0.9T_C$ was found to increase with the increasing Ru concentration. The peak in the anisotropy is consistent with theoretical results for the two band model [24] that expects to have the peak in anisotropy vs. temperature at $0.9T_C$. Similar peaks in the anisotropy were found for the electron doped $Ba(Fe_{1-x}Co_x)_2As_2$ [6, 25, 27], hole doped $(Ba_{1-x}K_x)Fe_2As_2$ [7] superconductors for several doping levels under both high and low field measurements. Recently there was a report on measurement of $\mu_0 H_{C2}$ in $Ba(Fe_{0.75}Ru_{0.25})_2As_2$ superconducting single crystalline samples using temperature and angle dependent in-field transport measurements [26]. The anisotropy ratio in this study was also found to be small ~2. The variation of anisotropy as a function of Ru fraction goes through a maximum around x=0.71 Ru fraction.

$\mu_0 H$-T phase diagrams with the irreversibility field of the superconductor were also estimated for all the samples. These systems show that the irreversibility fields remain very close to the upper critical fields in both the crystallographic directions. Upper critical fields were found to show a negative or upward curvature for the lesser Ru fractions but became nearly linear in T for the samples with higher Ru concentrations. A

more detailed $\mu_0 H$-T vortex phase diagram is presented in next chapter where the results from the magnetization measurements are also included.

References

[1] Hu R, Mun E D, Altarawneh M M, Mielke C H, Zapf V S, Bud'ko S L and Canfield P C 2012 Upper critical fields and two-band superconductivity in $Sr_{1-x}Eu_x(Fe_{0.89}Co_{0.11})_2As_2$ (x=0.20 and 0.46) *Physical Review B* **85** 064511

[2] Johnston D 2010 The puzzle of high temperature superconductivity in layered iron pnictides and chalcogenides *Advances in Physics* **59** 803-1061

[3] Shahbazi M, Wang X L, Shekhar C, Srivastava O N, Lin Z W, Zhu J G and Dou S X 2011 Upper critical field and thermally activated flux flow in $LaFeAsO_{1-x}F_x$ *Journal of Applied Physics* **109** 07E162-3

[4] Senatore C, Flükiger R, Cantoni M, Wu G, Liu R H and Chen X H 2008 Upper critical fields well above 100 T for the superconductor $SmFeAsO_{0.85}F_{0.15}$ with T_C=46K *Physical Review B* **78** 054514

[5] Altarawneh M M, Collar K, Mielke C H, Ni N, Bud'ko S L and Canfield P C 2008 Determination of anisotropic H_{C2} up to 60 T in $Ba_{0.55}K_{0.45}Fe_2As_2$ single crystals *Physical Review B* **78** 220505

[6] Kano M, Kohama Y, Graf D, Balakirev F, Sefat A S, McGuire M A, Sales B C, Mandrus D and Tozer S W Anisotropy of the Upper Critical Field in a Co-Doped $BaFe_2As_2$ Single Crystal *Journal of the Physical Society of Japan* **78** 084719

[7] Ni N, Bud'ko S L, Kreyssig A, Nandi S, Rustan G E, Goldman A I, Gupta S, Corbett J D, Kracher A and Canfield P C 2008 Anisotropic thermodynamic and transport properties of single-crystalline $Ba_{1-x}K_xFe_2As_2$ (x=0 and 0.45) *Physical Review B* **78** 014507

[8] Jaroszynski J, Riggs S C, Hunte F, Gurevich A, Larbalestier D C, Boebinger G S, Balakirev F F, Migliori A, Ren Z A, Lu W, Yang J, Shen X L, Dong X L, Zhao Z X, Jin R, Sefat A S, McGuire M A, Sales B C, Christen D K and Mandrus D 2008 Comparative High-Field Magnetotransport Of The Oxypnictide Superconductors $RFeAsO_{1-x}F_x$ (R=La , Nd) and $SmFeAsO_{1-\delta}$ *Physical Review B* **78** 064511

[9] Werthamer N R, Helfand E and Hohenberg P C 1966 Temperature and Purity Dependence of the Superconducting Critical Field, H_{C2}. III. Electron Spin and Spin-Orbit Effects *Physical Review* **147** 295-302

[10] Sefat A S, McGuire M A, Sales B C, Jin R, Howe J Y and Mandrus D 2008 Electronic correlations in the superconductor $LaFeAsO_{0.89}F_{0.11}$ with low carrier density *Physical Review B* **77** 174503

[11] Chen G F, Li Z, Li G, Zhou J, Wu D, Dong J, Hu W Z, Zheng P, Chen Z J, Yuan H Q, Singleton J, Luo J L and Wang N L 2008 Superconducting Properties of the Fe-Based Layered Superconductor $LaFeAsO_{0.9}F_{0.1-\delta}$ *Physical Review Letters* **101** 057007

[12] Jia Y, Cheng P, Fang L, Luo H, Yang H, Ren C, Shan L, Gu C and Wen H-H 2008 Critical fields and anisotropy of $NdFeAsO_{0.82}F_{0.18}$ single crystals *Applied Physics Letters* **93** 032503

[13] Hunte F, Jaroszynski J, Gurevich A, Larbalestier D C, Jin R, Sefat A S, McGuire M A, Sales B C, Christen D K and Mandrus D 2008 Two-band superconductivity in $LaFeAsO_{0.89}F_{0.11}$ at very high magnetic fields *Nature* **453** 903-5

[14] Jaroszynski J, Hunte F, Balicas L, Jo Y-j, Raičević I, Gurevich A, Larbalestier D C, Balakirev F F, Fang L, Cheng P, Jia Y and Wen H H 2008 Upper critical fields and thermally-activated transport of $NdFeAsO_{0.7}F_{0.3}$ single crystal *Physical Review B* **78** 174523

[15] Baily S A, Kohama Y, Hiramatsu H, Maiorov B, Balakirev F F, Hirano M and Hosono H 2009 Pseudoisotropic Upper Critical Field in Cobalt-Doped $SrFe_2As_2$ Epitaxial Films *Physical Review Letters* **102** 117004

[16] Zhang J L, Jiao L, Balakirev F F, Wang X C, Jin C Q and Yuan H Q 2011 Upper critical field and its anisotropy in LiFeAs *Physical Review B* **83** 174506

[17] Yuan H Q, Singleton J, Balakirev F F, Baily S A, Chen G F, Luo J L and Wang N L 2009 Nearly isotropic superconductivity in $(Ba,K)Fe_2As_2$ *Nature* **457** 565-8

[18] Tanatar M A, Ni N, Martin C, Gordon R T, Kim H, Kogan V G, Samolyuk G D, Bud'ko S L, Canfield P C and Prozorov R 2009 Anisotropy of the iron pnictide superconductor $Ba(Fe_{1-x}Co_x)_2As_2$ (x=0.074, T_C=23 K) *Physical Review B* **79** 094507

[19] Gurevich A 2011 Iron-based superconductors at high magnetic fields *Reports on Progress in Physics* **74** 124501

[20] Fuchs G, Drechsler S L, Kozlova N, Bartkowiak M, Hamann-Borrero J E, Behr G, Nenkov K, Klauss H H, Maeter H, Amato A, Luetkens H, Kwadrin A, Khasanov R, Freudenberger J, Köhler A, Knupfer M, Arushanov E, Rosner H, Büchner B and Schultz L 2009 Orbital and spin effects for the upper critical field in As-deficient disordered Fe pnictide superconductors *New Journal of Physics* **11** 075007

[21] Dhaka R S, Liu C, Fernandes R M, Jiang R, Strehlow C P, Kondo T, Thaler A, Schmalian J, Bud'ko S L, Canfield P C and Kaminski A 2011 What Controls the Phase Diagram and Superconductivity in Ru-Substituted $BaFe_2As_2$? *Physical Review Letters* **107** 267002

[22] Gurevich A 2003 Enhancement of the upper critical field by nonmagnetic impurities in dirty two-gap superconductors *Physical Review B* **67** 184515

[23] Gurevich A 2010 Upper critical field and the Fulde-Ferrel-Larkin-Ovchinnikov transition in multiband superconductors *Physical Review B* **82** 184504

[24] Golubov A A and Koshelev A E 2003 Upper critical field in dirty two-band superconductors: Breakdown of the anisotropic Ginzburg-Landau theory *Physical Review B* **68** 104503

[25] Vinod K, Satya A T, Sharma S, Sundar C S and Bharathi A 2011 Upper critical field anisotropy in $BaFe_{2-x}Co_xAs_2$ single crystals synthesized without flux *Physical Review B* **84** 012502

[26] Xing J, Shen B, Zeng B, Liu J, Ding X, Wang Z, Yang H and Wen H 2012 Transport properties, upper critical field and anisotropy of $Ba(Fe_{0.75}Ru_{0.25})_2As_2$ single crystals *Sci. China Phys. Mech. Astron.* **55** 2259-63

[27] Ni N, Tillman M E, Yan J Q, Kracher A, Hannahs S T, Bud'ko S L and Canfield P C 2008 Effects Of Co Substitution On Thermodynamic And Transport Properties And Anisotropic H_{C2} In $Ba(Fe_{1-x}Co_x)_2As_2$ single crystals *Physical Review B* **78** 214515

Chapter 5

Critical Current Density, Flux Pinning and Magnetic Phase Diagram

This chapter presents the estimation of Critical Current Density (J_C) as a function of magnetic field for various Ru-substitutions in $BaFe_2As_2$ single crystals. $J_C(H)$ is estimated from isothermal magnetization loops using Bean's Critical State model. An attempt to understand the fish-tail effect has been made. Type of flux pinning have been elucidated using the scaling analysis of flux pinning force density (F_P). Results of magnetic relaxation studies points to a crossover behavior in flux dynamics, from collective to a plastic creep. Finally, based on the anomalies in M(H) loops, transition temperatures from M(T)/R(T) curves and magnetization relaxation with time, the irreversibility and critical fields are determined, leading the proposed μ_0H-T vortex phase diagram.

5.1 Introduction

For engineering applications of superconductors, the critical current density (J_C) is often the most important parameter [1]. It is defined as the maximum electrical transport current density that the superconductor can carry without resistance and hence the dissipation-less current. Along with the critical temperature (T_C) and critical magnetic fields (H_C), the critical current density (J_C) marks the applicability limit of the superconducting state [2]. A high critical current density is required for almost all the

applications, be it power transmission lines, electromagnets, transformers, fault current limiters, energy storage and production machines or even a small passive microwave devices.

In the case of iron arsenide based superconductors, short coherence lengths (ξ) make it possible to achieve strong pinning of vortices and high critical current densities [3]. The vortices in iron arsenide based superconductors can be pinned by natural crystalline disorder such as dislocations and grain boundaries [3]. This is possible since the size of non-superconducting defects approximately equals the diameter of vortex core (2ξ ~ 4-10 nm) thereby giving maximum pinning force density [3]. A pinning by charge impurities in FeAs based superconductors has been reported by Van der Beek *et al.* [4]. However, similar to cuprates, the FeAs based superconductors also suffer from poor grain connectivity and thus critical current densities can be reduced drastically in the polycrystalline materials [3, 5-7].

For single crystalline FeAs based superconductors, the critical current densities are found to be very high. At low fields and low temperature (~ 4 K), J_C of the order 10^4-10^6 A/cm^2 has been reported using magnetization and transport measurements [8-12]. High transport critical current densities are also reported for the metallic Sn added (Sr,K)Fe_2As_2 tapes [13]. The fine pattern of structural domains created by non-superconducting phases or heavy ion irradiation of pnictide superconductors have been shown to enhance critical current density [9, 14]. For the Co-doped $BaFe_2As_2$ single crystals, critical current density was found to follow the superconducting dome of doping (*T*-*x*) phase diagram but maximum J_C was found to occur for the slightly under-doped sample [9].

In the case of charge doped (K-doping at Ba, Co or Ni-doped at Fe site) in $BaFe_2As_2$ a generic feature is the occurrence of fish-tail effect [10] in the isothermal magnetization, which gives rise to a second broad hump in the critical current density [15, 16]. Due to the occurrence of fish-tail effect, the critical current densities remain very high even at fields as high as 9 T. Fish-tail effect also gives rise to a richer $\mu_0 H$-T phase diagram containing different vortex phases for doped $BaFe_2As_2$ superconductors [16, 17]. However, the fish-tail effect is not seen in isovalent *P*- substitution at As in $BaFe_2As_2$ [11] and $CaFe_2As_2$ based compounds [12]. Thus in order to understand if there is any difference in vortex structure of charge doped $BaFe_2As_2$ based superconductors from isovalent substitutions, it is important to study the critical current density and vortex dynamics of isovalent Ru substituted $BaFe_2As_2$ superconductors.

This chapter mainly presents the results of the isothermal magnetization measurements on $BaFe_{2-x}Ru_xAs_2$ superconductors and an estimation of the critical current density from it. Flux pinning properties including the flux pinning force density, is presented for samples with varying Ru content. The thermomagnetic history dependence of the critical current density is shown and results of the magnetization relaxation measurements are presented. The chapter ends with the presentation of a $\mu_0 H$-T vortex phase diagram for $BaFe_{2-x}Ru_xAs_2$ ($x = 0.71$) superconductor.

5.2 Critical current density of superconductors: An overview

In the BCS superconductors, the maximum critical current density is limited by the kinetic energy of the Cooper pairs participating in an electrical transport [1]. When the kinetic energy of these Cooper pairs increases beyond the energy gap, the Cooper

pairs break and form normal resistive quasiparticles. This sets the ultimate limit to J_C [1], the so called de-pairing critical current density $\boldsymbol{J_D = \frac{\emptyset_0}{3\sqrt{3}\pi\mu_0\lambda^2\xi}}$, which depends upon the penetration depth (λ) and coherence length (ξ) of the superconductor. ϕ_0 is the magnetic flux quantum. The de-pairing current densities at zero Kelvin and zero magnetic field are of the order of 10^{11} to 10^{12} A/m^2. In actual practice, these values of J_D are never attained because of other limitations such as self-field production on the surface of superconductors.

In type-II superconductors, for magnetic fields higher than $\mu_0 H_{C1}$, the magnetic free energy is minimized only if the magnetic field enters into the bulk of the superconductor in the form of quantized tubes of flux, each carrying exactly one quantum of flux (ϕ_0=2.0679x10^{-15} T-m^2). Each flux line carries a quantum of flux so in order to minimize the inter-flux interactions they distribute themselves into a periodic hexagonal or triangular lattice known as Abrikosov lattice. This gives rise to a richer mean field phase diagram with an additional "mixed phase" in between Meissner phase and normal metallic states [18].

In type-II superconductors, while the transition temperature and critical fields are the intrinsic properties, the critical current density has a strong dependence on the metallurgical state of the material as it depends upon the dynamics of the vortex system [2]. A Lorentz force is experienced by a vortex if a current flows in the mixed state of the superconductor. This force per unit volume is given by: $\boldsymbol{F_L = J \times B}$. If vortices are not pinned, they will move in the direction of this force, and this will in turn give rise to an electric field $= \boldsymbol{v \times B}$, where $\boldsymbol{v}$ is the velocity of vortices. Thus, the critical current is

that current at which a detectable voltage is generated due to motion of vortices. When the Lorentz force due to current and magnetic field exceeds the pinning force, the vortices start to move, and this defines the critical current density of a type II superconductor: $\boldsymbol{F_L = F_P}$; $\boldsymbol{J_C = \frac{F_P}{B}}$.

Measurement of J_C of a superconductor involves the tracing of current-voltage (*I-V*) curves and the current at which a measurable voltage first appears is considered as the engineering critical current density J_C [1]. To measure the critical current, following criteria are used: (i) *Electric field criterion*: The voltage levels measured at $J=J_C$ are of the order of 10^{-6} volts giving rise to electric field values of 10 μVm^{-1} and required current densities are around 10^5 amps/cm^2. (ii) *Resistivity criterion:* The standard criterion for qualifying any material for technological applications requires a flux-flow resistivity of 10^{-12} Ω-cm at $J=J_C$ [19]. (iii) *Offset criterion*: Critical current is measured using linear part of *I-V* curves and extrapolating it to cross zero-voltage line. The point on *I- axis* where tangential line to *I-V* curve crosses the zero voltage line defines the critical current density. It must be indicated that in presence of a large flux creep [20], a significant error arises in the measurement of critical current density, when the electric field and resistivity criterions are employed. The above measurements of J_C require properly shaped samples with known dimensions along with current sources capable of providing very large magnitudes of current. Making electrical contacts on the samples also pose difficulties as they should contribute very small contact resistances.

Alternatively, the critical current density of type-II superconductors can also be inferred from the hysteresis of magnetization versus field (*M-H*) measurements

[19, 21]. It is well known that external changes in the magnetic field set up screening currents in the superconductor, which shield the interior of the sample from the field. According to the Bean's critical state model [22] the current density at any instant in a superconductor is always equal to its critical current density [22] and the pinning force is constant in the critical state [21]. In the interior of a superconducting sample, the magnetic field and super current density are coupled through the Maxwell relation and various critical-state models [21] are based on a specific relationship between the internal field and critical current density. In the Bean's model the critical current density J_C remains independent of the internal field.

Using the Bean's critical state model the critical current density of samples with known geometries can be derived from the width (ΔM) of the hysteresis in the isothermal magnetization (M-H) curves and the sample dimensions. For a parallelepiped sample having dimensions a, b and c with field parallel to c-direction, the critical current density can be calculated using [16]:

$$\boldsymbol{J_C(H) = \frac{20 \times \Delta M}{a\left(1-\frac{a}{3b}\right)}} \qquad (5.1)$$

Where ΔM is the width of M-H loop in emu/cm^3, sample dimensions perpendicular to the field, a and b, are in cm, with a < b. The value of the critical current density by magnetization measurements are usually not similar to the J_C measured using transport method [9, 16], since the J_C inferred from magnetization does not reflect the weak links in the sample as current flowing across them does not persists for long times. In spite of this shortcoming, the method is extensively used to determine the orders of magnitude of J_C and its field dependence. In the present chapter we have employed Bean's critical state

model to determine critical current density of Ru- substituted superconducting $BaFe_2As_2$ single crystals using isothermal magnetization measurements as described in chapter 2.

5.3 Temperature dependent magnetization

The temperature dependent zero-field cooled magnetization measurements performed on $BaFe_{2-x}Ru_xAs_2$ (x = 0.5, 0.55, 0.6 and 0.71) single crystals under an applied magnetic field of 0.01T are shown in figure 5.1. The transition temperatures for various samples with different Ru content, found by resistivity measurements as described in chapter 4, were close to those measured by magnetization.

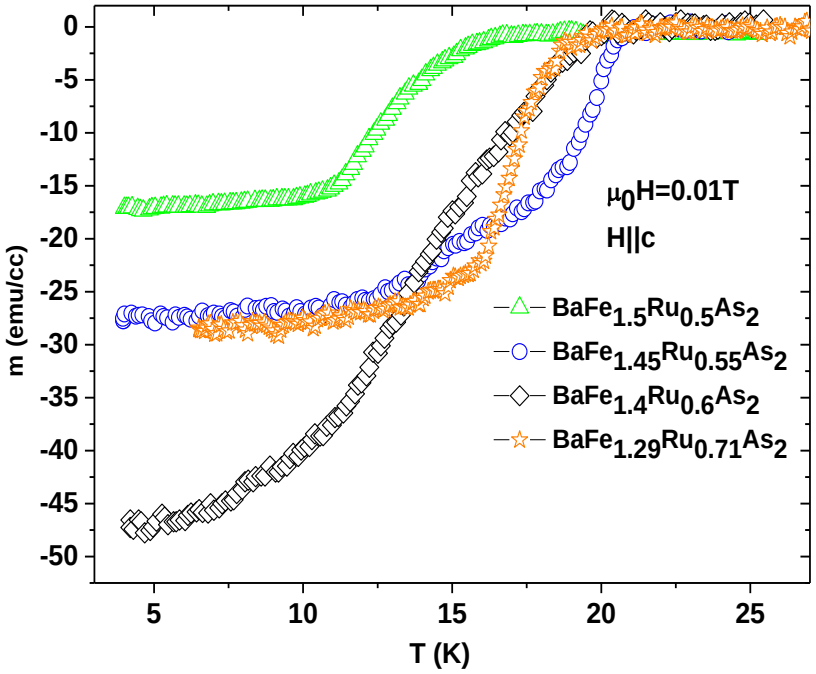

Figure 5.1: The temperature dependent magnetization measurements performed on $BaFe_{2-x}Ru_xAs_2$ (x = 0.5, 0.55, 0.6 and 0.71) single crystals in zero-field state under an applied magnetic field of 0.01 T. Superconducting transitions in zero-field cool protocol are very sharp.

Further, the superconducting volume fraction estimates to be ~ 90%, when compared with that obtained for the superconducting volume fraction obtained in a lead (*Pb*) sphere of ~ 1 mm diameter. This indicates that Ru-substituted single crystal exhibits bulk superconductivity, and the sharp superconducting transition implies that crystals are of good quality.

5.4 Isothermal magnetization (*M-H*) loops

Isothermal magnetization loops for the superconducting $BaFe_{2-x}Ru_xAs_2$ samples were measured on zero field cooled samples. To avoid errors due to demagnetization factors, single crystals, used to measure *M-H* loops, were shaped as parallelepiped with typical dimensions of 0.5-0.8 mm along *a* and *b* axes while the thickness of the crystals was around 0.01-0.02 mm. Samples were mounted in starch capsules sealed inside a non-magnetic plastic straw. The magnetization isotherms in fields up to 16 T applied parallel to *c-axis* were recorded. Field was ramped at 0.5 T/min, at several temperatures ranging from 2 K up to 15 K, as shown in Figure 5.2. The *M-H* curves are symmetric about field axis (see figure 5.2) which suggest that the bulk pinning instead of the surface barrier dominates in the samples [20].

A general feature of the *M-H* hysteresis loops is a broad second magnetization peak (SMP) or a clear fish-tail [10] for both the field directions. We observed similar fish-tail features in several different crystals from the same batch, cut with different aspect ratios, implying that the observed SMP is not an artifact of the sample geometry. It is also noteworthy that the observed fish-tail for $H||c$ direction in the

present Ru-doped single crystals is similar to that observed for Co- and K-doped $BaFe_2As_2$ single crystals [10, 16, 23].

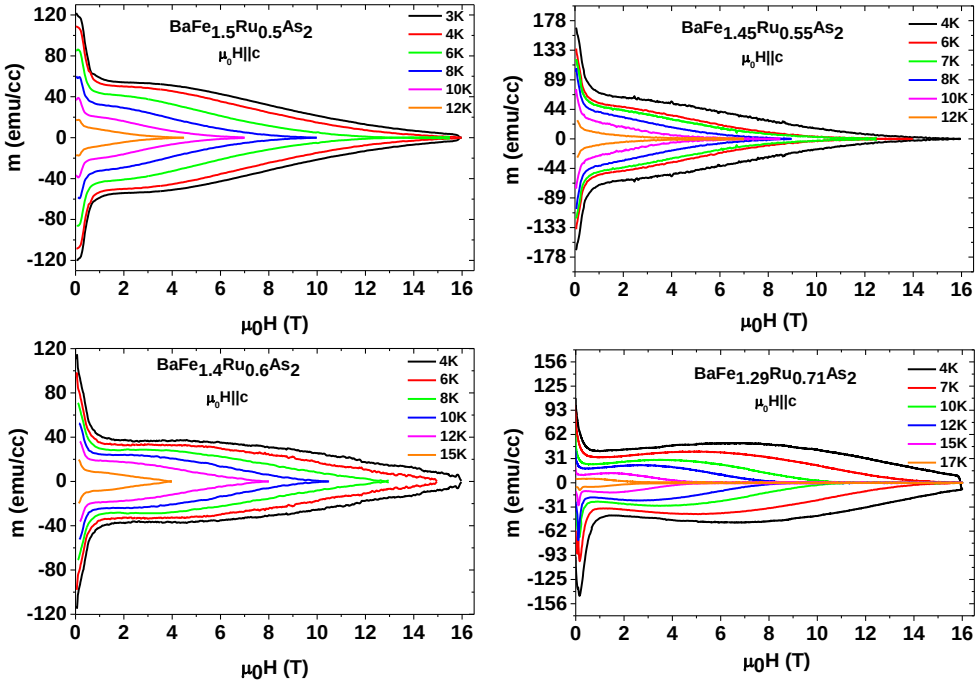

Figure 5.2: Magnetization hysteresis loops for 0.5, 0.55, 0.6 and 0.71 samples performed at different temperatures in field parallel and perpendicular to the c-axis. The single crystals used to measure *M-H* loops were shaped as parallelepiped with typical dimensions of 0.5-0.8 mm along *a* and *b* axes while the thickness of the crystals was around 0.01-0.02 mm. A fish-tail effect can be clearly seen from these figures.

In figure 5.3, we show the *M* versus $\mu_0 H$ loop for $H||ab$ direction recorded on x = 0.71 sample. The value of magnetization is lesser in this field direction when compared to the magnetization due to field applied along *c-axis*. It is observed from the figure that the SMP is seen in this field direction too, but is less pronounced as compared to that for $H||c$. For a particular temperature, the peak of the fish-tail effect shows up at a lower field for $H||c$ direction as compared to that along $H||ab$ direction. The occurrence of fish-tail effect was also found to depend on Ru concentration in samples. Implications of these on the critical current density are described subsequently.

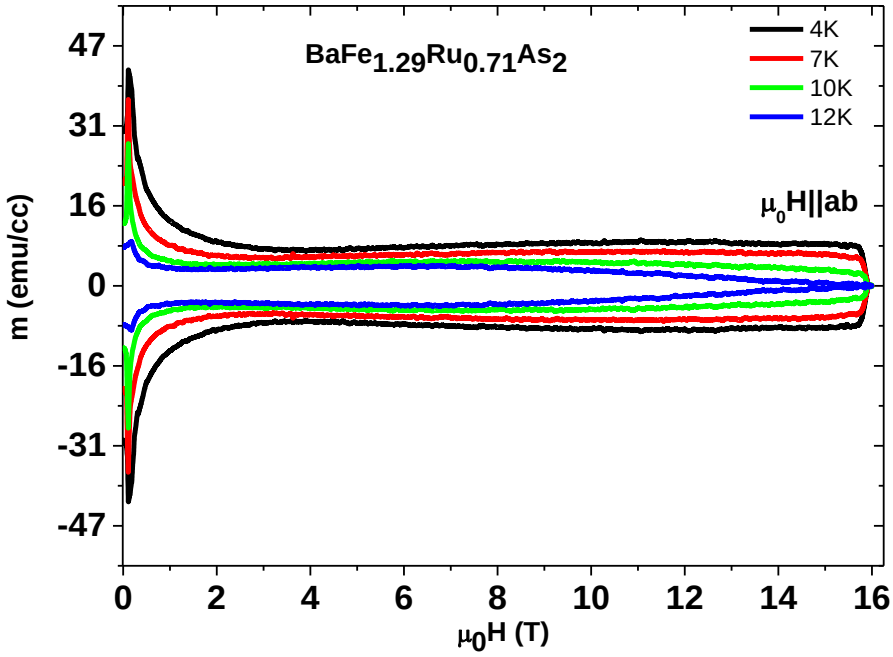

Figure 5.3: Magnetization hysteresis loops measured at 4 K, 7 K, 10 K and 12 K for x = 0.71 sample in field parallel to *ab-plane*. SMP is seen in this field direction too, but is less pronounced as compared to that for $H||c$. For a particular temperature the fish-tail effect peak shows up at a lower field for $H||c$ direction as compared to that along $H||ab$ direction.

5.5 Critical current density estimation

As discussed in section 5.2, the critical current density of the Ru-substituted $BaFe_2As_2$ samples was estimated using equation 5.1 derived from Bean's critical state model for parallelepiped sample geometry. Figure 5.4 shows the critical current density as a function of magnetic field for x = 0.71 sample in both $H||c$-axis and $H||ab$-plane direction. It should be borne in mind that for the field direction along *c-axis*, critical currents circulate in *ab-plane* (J_C^{ab}), while for the field applied parallel to *ab-plane*, the critical currents circulate both along *c-axis* (J_C^{c}) and *ab-plane*. Therefore, the critical current density measured with field parallel to *ab-plane*, which has contributions from both J_C^{ab} and J_C^{c} is thus an average of the critical current density in both directions.

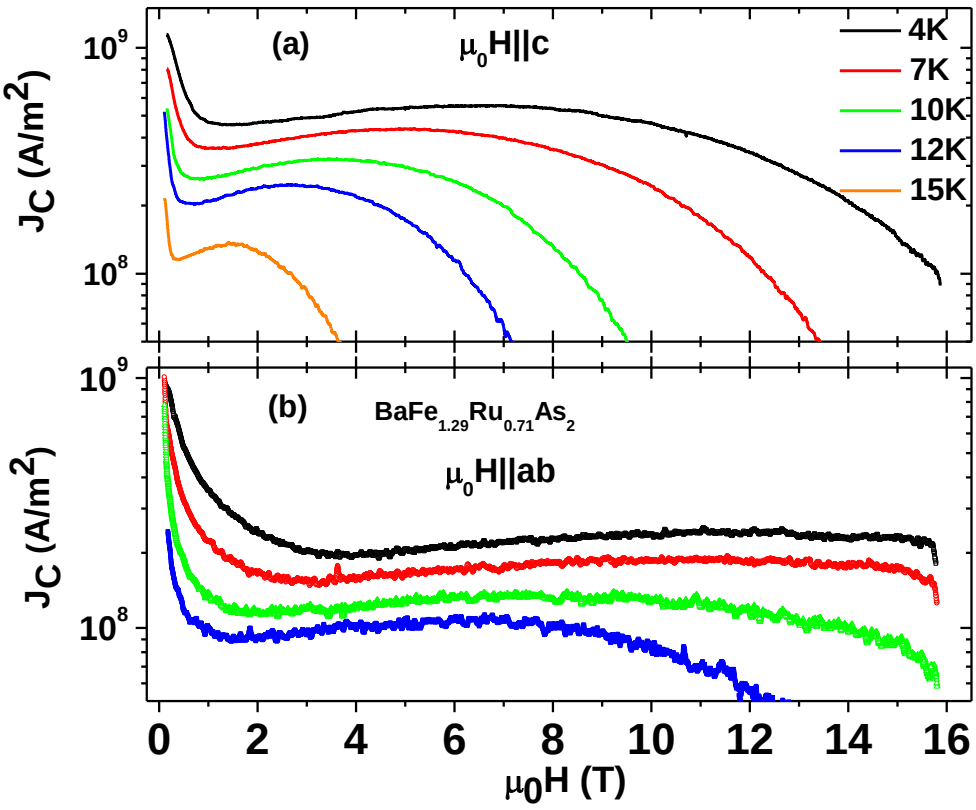

Figure 5.4: Critical current density as a function of magnetic field for x=0.71 sample in both $H||c$-axis and $H||ab$-plane direction. At 4 K and low fields the value of J_C is ~ 10^9 A/m^2.

It is seen from figure 5.4 that J_C is very large at very low fields which quickly decreases followed by a broad hump at intermediate fields as a consequence of the fish-tail effect in the *M-H* isotherm. At low temperatures, J_C remains nearly constant with increasing field up to 10 T. At 4 K and low fields the value of J_C is ~ 10^9 A/m^2, which is well above the value of 10^8 A/m^2 required for applications [1, 2]. We note that the low field J_C of the present Ru-doped sample is slightly lower as compared with that of the electron doped (Co- and Ni-doped) samples [10, 16, 23], the hole doped (K-doped) sample [10, 15] and isovalent Ru-substituted $BaFe_2As_2$ [24]. With increasing temperature, the SMP shifts to lower fields and becomes more pronounced (see figure 5.2 and 5.3), for both $H||ab$ and $H||c$. It is also evident from Figure 5.4 that the rate of

decrease of J_C at higher fields is lower for $H||ab$, compared with that in the $H||c$ configuration.

In figure 5.5, we compare $J_C(H)$ in two directions of applied field at 12 K. It is noted that the value of $J_C(H||c)$ is higher than $J_C(H||ab)$ up to a crossover field ($\mu_0 H_{cross\text{-}over}$), after which the $J_C(H||ab)$ takes over. This indicates better pinning strength for $H||ab$, compared to $H||c$, particularly at higher fields. This strange–behavior was found to exist at all the temperatures and a plot of cross-over field vs. temperature is shown in inset of figure 5.5. It is seen that with increase in the temperature, the cross-over field decreases monotonically.

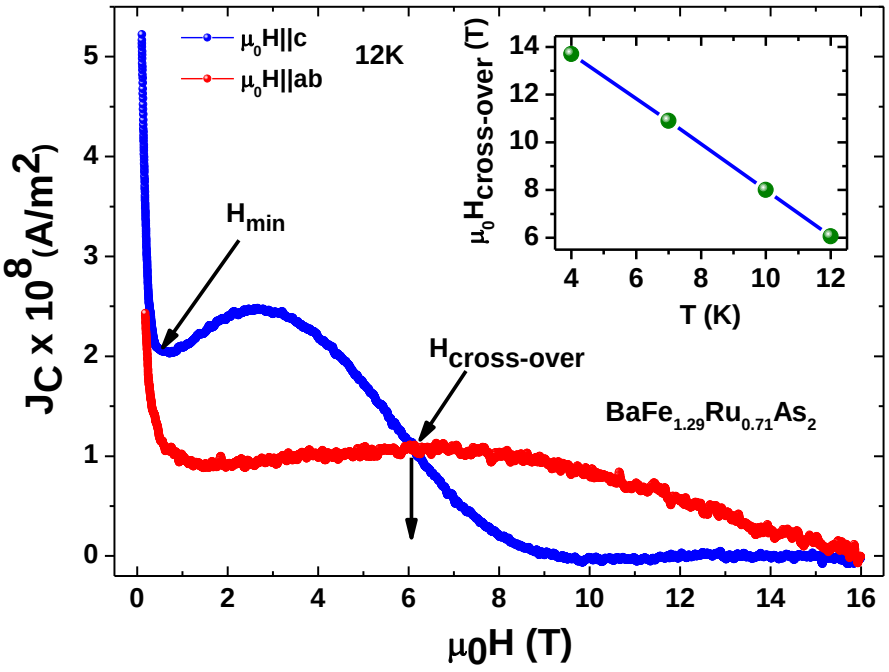

Figure 5.5: Comparison of $J_C(H)$ in two field direction measured at 12 K. For all the temperatures, value of $J_C(H||c)$ is higher than for $J_C(H||ab)$ up to a cross-over field ($\mu_0 H_{cross\text{-}over}$), after which the $J_C(H||ab)$ takes over the $J_C(H||c)$. This indicates better pinning strength for $H||ab$, compared to $H||c$, at higher fields. Inset: the filed at which $J_C(H||ab)$ crosses $J_C(H||c)$ decreases with increase in the field.

5.6 Compositional dependence of critical current density

To study the effect of Ru content on the critical current density of $BaFe_{2-x}Ru_xAs_2$ superconductors, variation of J_C as a function of applied field was investigated for several different samples with varying Ru contents. The isothermal magnetization loops for various compositions were shown in figure 5.2. Superconducting screening current density flowing in *ab-plane* of single crystals due to application of field along c-axis was calculated for x = 0.5, 0.55 and 0.6 single crystalline samples. The variation of superconducting current density as a function of applied field along *c-axis* on different samples is shown in various panels of figure 5.6. Current densities at low field and temperatures are of the order of 10^9 A/m^2 for all the Ru-substituted $BaFe_2As_2$ single crystals. Since for field parallel to *ab*-plane the J_C has contributions from current densities along *c*-axis and *ab*-plane so $J_C(H||ab)$ has not been estimated for these samples.

The critical current density of a superconductor depends upon three parameters namely: critical temperature of the superconductor, its upper critical field and pinning arising due to intrinsic and extrinsic pinning sites [19]. In figure 5.7 we compare the critical current density of different samples (x = 0.5, 0.55, 0.6, and 0.71) at 4 K and 8 K. It is seen that the zero field critical current at lowest measured temperature is the highest for the $BaFe_{1.45}Ru_{0.55}As_2$ system, which has a T_C ~ 22 K.

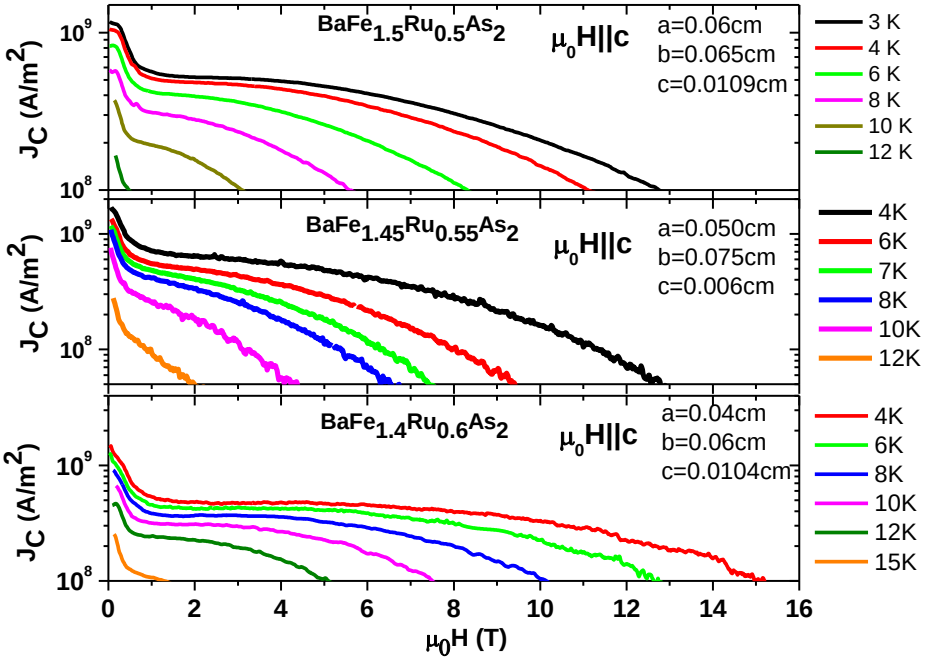

Figure 5.6: Superconducting screening current density flowing in *ab*-plane of single crystals due to an application of field along *c*-axis obtained for *x*=0.5, 0.55 and 0.6 samples using Bean critical state model. Sample dimensions are given. Current densities at low field and temperatures are of the order of 10^9 A/m^2 for all the Ru-substituted $BaFe_2As_2$ single crystals.

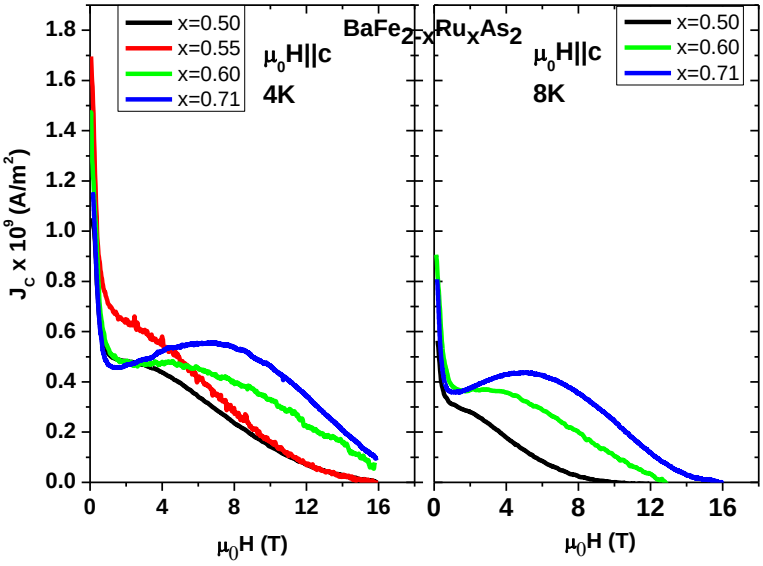

Figure 5.7: Comparison of $J_C(H)$ for several compositions of $BaFe_{2-x}Ru_xAs_2$ single crystals. The zero field critical current at lowest measured temperature is the highest for the $BaFe_{1.45}Ru_{0.55}As_2$ system as the T_C ~ 22 K for this compound is the highest in the T_C *vs. x* phase diagram (chapter 3). The low field and low temperature J_C follows the T_C vs. *x* phase diagram. The fish tail effect is pronounced for higher Ru-substituted system and gradually decreases with decrease in the Ru-content of the system.

In figure 5.8, we present the variation of critical current as a function of Ru fraction, estimated for fields below and within the fish-tail region (see figure 5.7). It is seen that $J_C(H)$ at low field and low temperature follows the T_C *vs.* x phase diagram (see figure 3.22) of $BaFe_{2-x}Ru_xAs_2$ system. In the fish-tail region, J_C is seen to increase monotonically with increase in the Ru content of $BaFe_{2-x}Ru_xAs_2$ superconducting sample

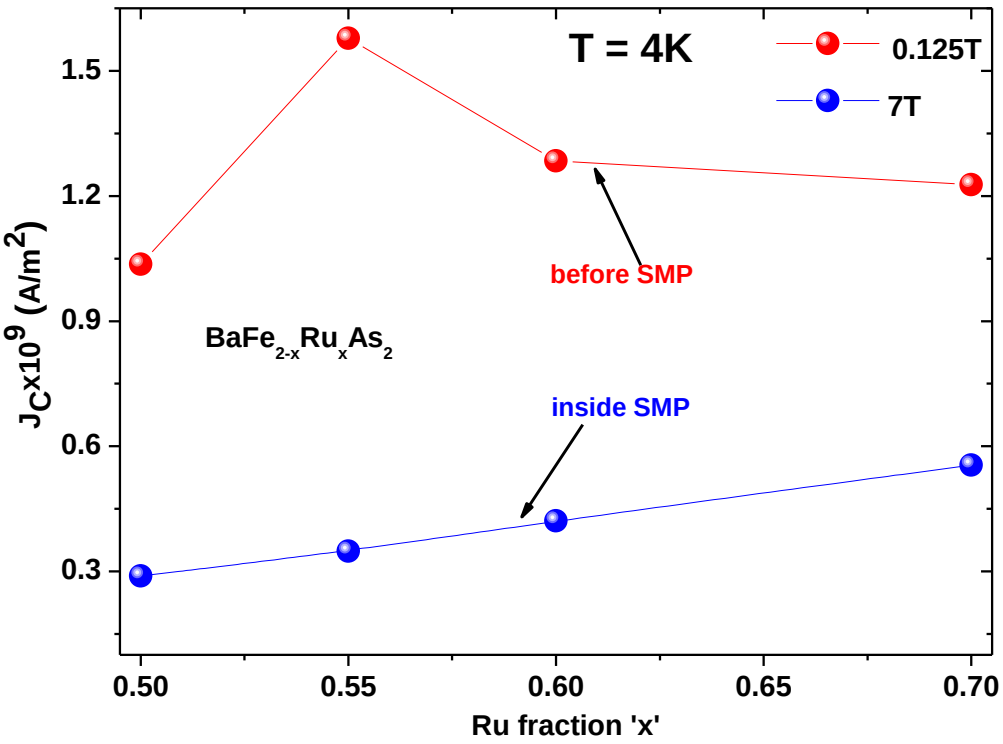

Figure 5.8: Variation of J_C at 4 K as a function of Ru fraction, for fields before fish-tail effect and well within fish-tail region (7 T). Below fish-tail region, J_C follows the phase diagram of the of $BaFe_{2-x}Ru_xAs_2$ superconductor with the maximum for x=0.55 sample having the highest T_C ~22 K. Above fish-tail region, J_C increases monotonically with increase in the Ru content of $BaFe_{2-x}Ru_xAs_2$ superconducting sample.

As seen in Fig. 5.7, the $BaFe_{2-x}Ru_xAs_2$ compounds show a pronounced fish-tail effect in the critical current density. The peak effect in the current density of a superconductor is an unusual pinning phenomenon [20] and is believed to arise because of an underlying phase transition in the flux line lattice [16]. The peak effect has been

observed in both metallic superconductors and HTSCs. The peak effect is close to upper critical field for superconductors with small Ginzburg-Landau (GL) parameter κ and shifts to lower fields as the GL parameter increases [20]. In the case of HTSCs, the GL parameter is very high and the peak effect occurs at a low value of applied magnetic field.

In $BaFe_{2-x}Ru_xAs_2$ system, the fish tail effect is more pronounced for higher Ru concentration. This gives a higher critical current density at intermediate fields due to increased pinning, possibly due to Ru. It is seen from figure 5.8 that inside the SMP, the critical current density increases with Ru content. As the Ru content increases the fish-tail effect increases and critical current density in the intermediate field regions also follows the same trend. Such an increase in the critical current density in the fields as high as ~ 10 T is advantageous for technological applications requiring high critical current densities at high fields. Similar trends have been observed at all the temperatures.

5.7 Thermomagnetic history dependence: Understanding fish-tail effect

It must be mentioned that using field cooled magnetization measurements close to the peak effect in $CeRu_2$ and $NbSe_2$ [25, 26], it was shown that the peak effect arose as a consequence of a first order phase transition [27]. History effects in the superconducting current density have been observed in the field range spanning the peak or SMP region [28] : The critical current density is not uniquely determined by the final condition of field and temperature but depends also on the path through which the final state is reached [29]. Taking cue from these studies, here we investigate, if the SMP in $BaFe_{2-x}Ru_xAs_2$ system too can arise from a first order transition in underlying vortex lattice. Superconducting samples $x = 0.71$ showing maximum second magnetization peak and $x =$

0.5 showing least SMP (see figure 5.7) were subjected to a series of field cooled magnetization measurements at 12 T. The measurement protocol involved field cooling the sample from 25 K to measurement temperature (12 K) under different applied fields and then isothermally measuring magnetization upon reducing the field to zero. It is seen from the figure 5.9 (a) that for field cooling the sample under 6 T to 2.5 T, the magnetization curves merge into one curve. For lower fields the M versus H curves follow a different envelop curve. All *M(H)* curves however merge together below H_{min}. It is noted that for a given field below fish-tail region, sample has two different thermo-magnetic history dependent J_C.

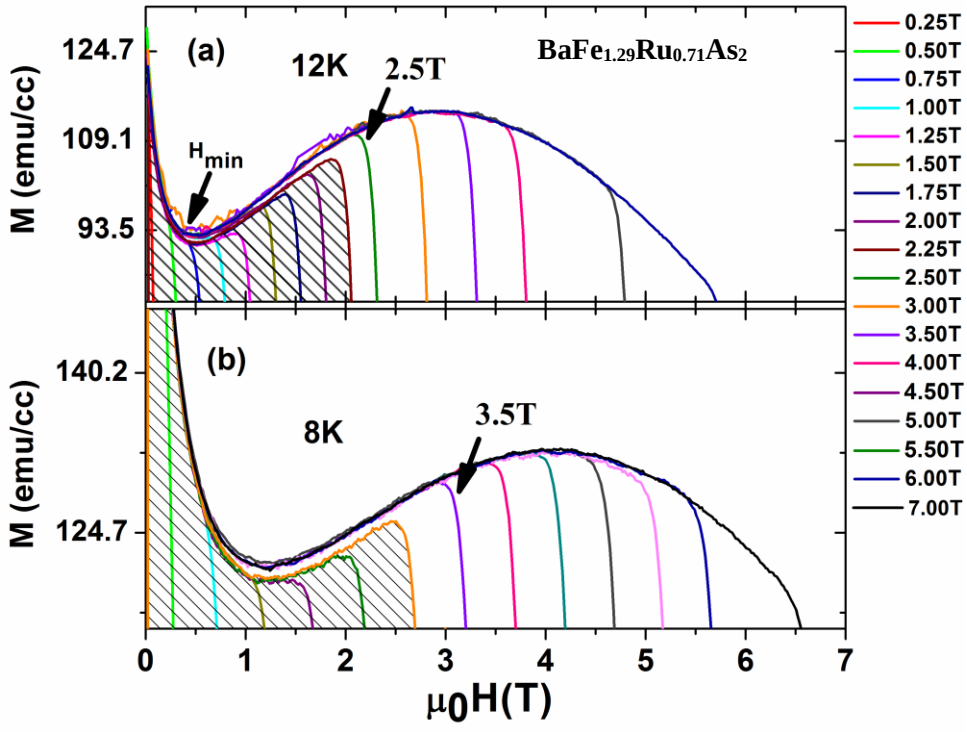

Figure 5.9 (a): *M(H)* curves recorded upon field reversal from different vortex states obtained by field cooling from normal state (25 K) down to 12 K under different external magnetic fields indicated. It is noted that for a given field below fish-tail region (shaded area), sample has two different thermo-magnetic history dependent J_C. **(b):** Similar thermo-magnetic history dependence of $J_C(H)$ at 8 K shows that the sample has two different $J_C(H)$ below 3.5 T

To substantiate the above results, we show the results of similar measurements carried out at 8 K, in figure 5.9 (b). Here again, we observe that for cooling the sample from fields higher than SMP field down to 3.5 T , the *M(H)* curves merge onto one another. However, for cooling the sample in fields between 3.5 T and onset of SMP, *M(H)* curves merge onto a different envelop curve (shown by shaded area). This history dependent magnetization, seen from figure 5.9 (a) and (b) suggests the presence of a field driven metastability [27] in the Ru-doped crystals.

In Figure 5.10, we show the results of field cooled isothermal magnetization measurements at 7 K for x = 0.55 sample, that shows minimum fish-tail effect. In this case, the critical current density in this sample was found not to depend upon the thermo-magnetic history of the sample within the limits of resolution of our magnetometer.

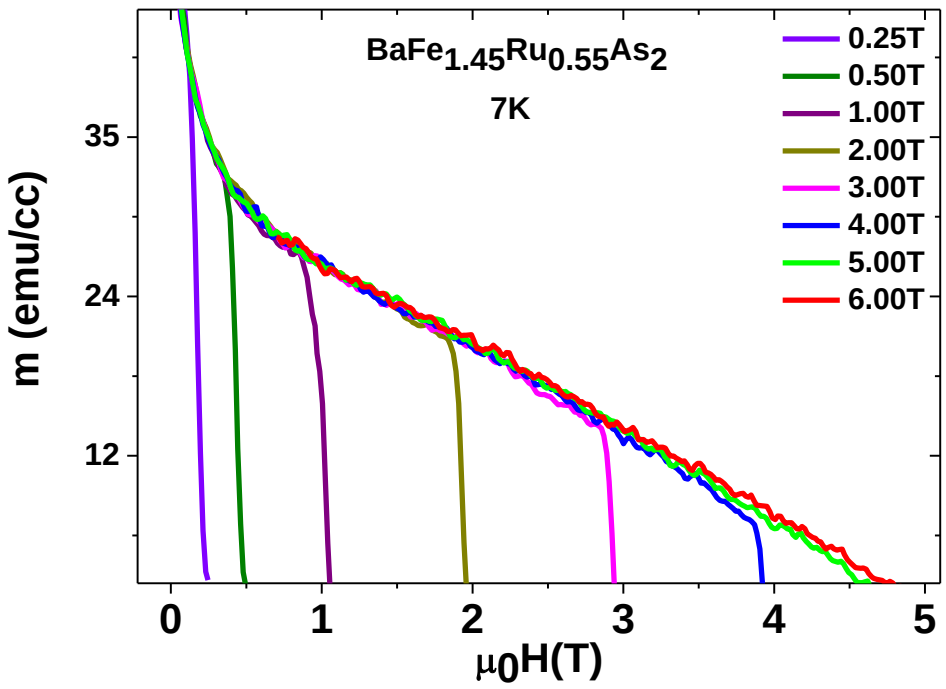

Figure 5.10: Field cooled isothermal magnetization measurements at 7 K for x = 0.55 samples that show least fish-tail effect. The critical current density in this sample in the intermediate field region was not found to depend upon the thermo-magnetic history of the sample within the limits of resolution of our magnetometer.

5.8 Pinning force density (F_P) and determination of type of pinning centers

The substantially high value of critical current density in the Ru-substituted $BaFe_2As_2$ superconductor points to a high flux pinning force density in these compounds. Pinning force per unit volume or flux pinning force density [30] is given by $F_p(H) \propto H_{C2}^n(T) fn(h)$, where the value of n and the form of $fn(h)$ are characteristics of the pinning mechanism, h is the reduced field (H/H^*) and $\mu_0 H^*$ is the field at which J_C becomes zero. For conventional type II superconductors like NbTi and Nb_3Sn, $\mu_0 H^*$ is the same as $\mu_0 H_{C2}$ of the superconductor. In the case of HTSCs, where the fluxons starts flowing above irreversibility line and J_C reduces to zero much below the actual upper critical field, irreversibility field $\mu_0 H_{irr}$ is used for $\mu_0 H^*$. Pinning force density ($\mu_0 H J_C$) was analyzed using Dew-Hughes methodology [30]. If the spacing between the pinning centers is much larger than the flux line spacing, the Kramer's function [31] $\mu_0 J_C^{0.5} H^{0.25}$ is a linear function of $\mu_0(H^*-H)$. The temperature dependent irreversibility field $\mu_0 H_{irr}$ was determined by linearly extrapolating the Kramer's function $\mu_0 J_C^{0.5} H^{0.25}$ at high fields to $J_C=0$.

It is instructive to plot the normalized pinning force density versus reduced magnetic field to understand the vortex pinning mechanism. This will help to ascertain whether the type of pinning centers that exist in samples showing fish-tail effect are different from those without fish-tail effect. Normalized pinning force density $f_p=F_p/F_{pmax}$ plotted as a function of reduced field $h=H/H_{irr}$ at different temperatures for the x = 0.71 sample are shown in figure 5.11.

It is seen from the figure 5.11 that for $H||c$, the normalized curves of $Fp(h,T)$ collapse on to a single curve. This when fitted with the Dew-Hughes function [30], $h^p(1-h)^q$ results in p~1.95 and q~2.5 . The temperature independent Fp scaling and symmetric $Fp(h)$ curves with a peak at h_{max}~0.45 indicates a dense vortex pinning nano-structure for x = 0.71 system. The dense vortex structure could result from inhomogeneous distribution of Ru ions, which in turn could produce a locally varying order parameter [23].

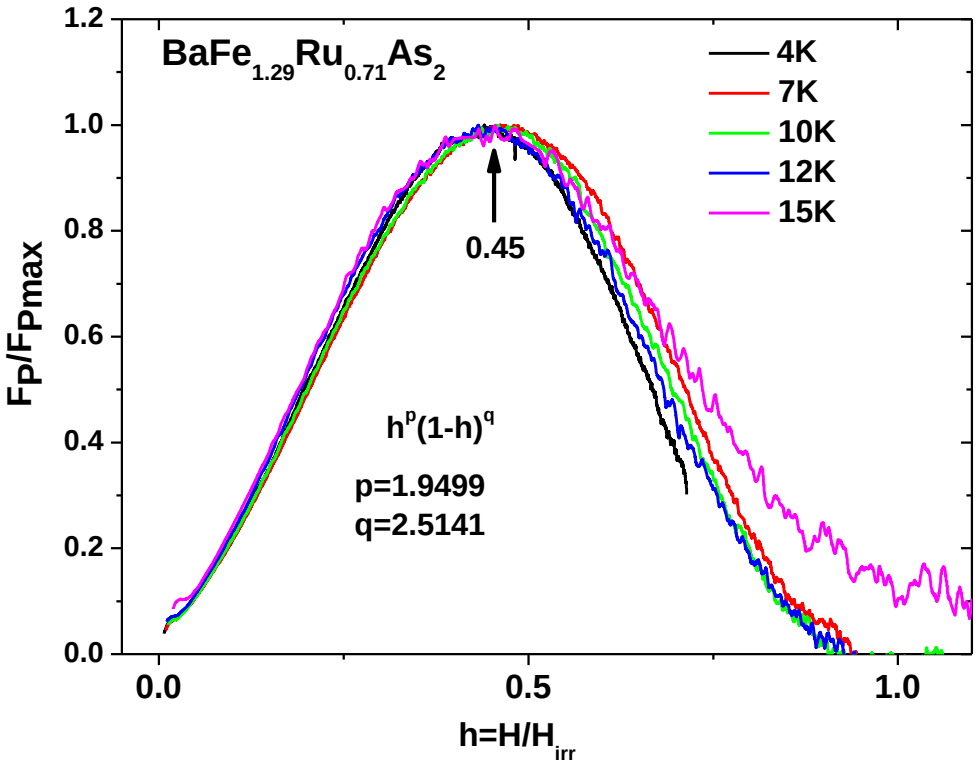

Figure 5.11: Temperature independent scaling analysis of normalized pinning force density for x=0.71 sample. Scaling on a single curve and peak at h~0.45 is suggestive of the presence of dense pinning centers [23] due to inhomogeneous Ru ion distribution.

In figure 5.12, a plot of the normalized pinning force density as a function of reduced magnetic field for x = 0.5 sample is presented. We have chosen this particular sample for analysis because the fish-tail effect is very less in this superconducting

sample. It is clear from the plot shown in figure 5.12, that for the x = 0.55 sample also, the normalized curves of $fp(h,T)$ collapse on to a single curve except for the position of peak now shifts to h_{max} = 0.33 and a fit with the Dew-Hughes function, $h^p(1-h)^q$ results in p~1.32 and q~2.74. According to Dew-Hughes [30], the peak position at h_{max} = 0.33 implies normal point pinning due to core interaction in lower Ru containing samples. Thus there is a marked difference between the nature of pinning mechanism that exists in composition showing fish-tail peak as compared to that without fish-tail effect.

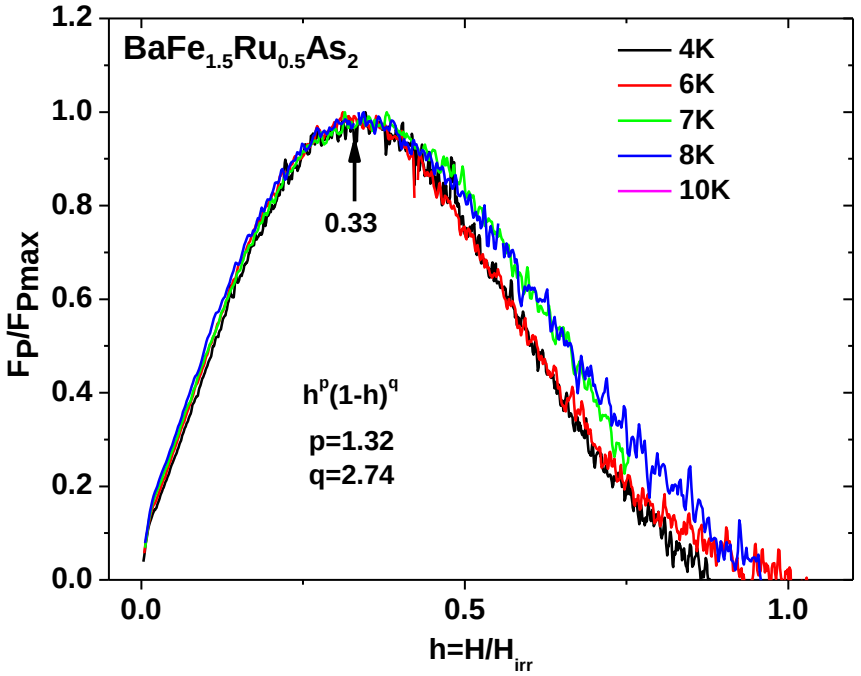

Figure 5.12: Temperature independent scaling analysis of normalized pinning force density for x=0.5 sample. The peak position at h=0.33 of the scaled normalized F_P plots shows that the pinning in the sample can be ascribed to normal point pinning due to core interaction in lower Ru containing samples.

5.9 Magnetization relaxation measurements

Anderson and Kim [32, 33] introduced the concept of thermally activated flux motion out of the pinning sites. This flux flow continues at a rate proportional to

$exp(-U_0/k_BT)$, with U representing an activation energy, k_B is Boltzmann constant and T the absolute temperature. Due to flux motion, a redistribution of flux profile takes place inside the superconductor and as a result the current loops associated with the flux also changes. These redistributions of flux and current loops thereby change the magnetic moment with time leading to the phenomenon of magnetization relaxation. The Anderson-Kim phenomenon is also known as Flux Creep, an important property of the mixed state of type-II superconductor. The motion of flux lines can not only be initiated due to thermal excitations but also due to quantum mechanical tunneling of flux line from the pinning sites at low temperature. Since the relaxation depends upon the limiting current density, the barrier height U_0 and attempt time for flux jumps, an analysis of the relaxation phenomenon can help us to understand the vortex dynamics and pinning properties [18].

To understand the kind of vortex dynamics above and below fish-tail effect, the critical state magnetic relaxation over a period of time for different fields was studied at 12 K for $x = 0.71$ sample. Figure 5.13 shows a plot of $ln\ m$ vs $ln\ t$ for different magnetic fields applied parallel to c-axis. In all the measurements, the zero field cooled sample was subjected to a high magnetic field (~7 T) much higher than the field corresponding to the SMP. After forming the vortex state at higher field the relaxation in magnetization was studied for different fields above and below the fish-tail region. Figure 5.13 shows relaxation in the magnetization recorded over a period of ~10000 seconds at several measuring fields spanning from below the fish-tail effect to 4T. Inset of figure 5.13 shows a typical relaxation measurement at 0.5 T field recorded up to 10000 seconds.

In the collective creep model [16], the time dependent magnetization is given by

$$m(t) = m_c\left(1 + \frac{\alpha T}{U_0}\ln\frac{t}{t_0}\right)^{-1/\alpha} \qquad (5.2)$$

where t_0 is the macroscopic relaxation time and α is dependent on the nature of pinning. Positive value of α describes collective creep barriers [18]. The relaxation data shown in inset of figure 5.13 has been fitted to equation 5.2 and the fitting was found reasonably well. It was seen that up to 1 T field, the magnetization relaxation data fits very well to small-bundle collective creep model. At 1 T, values of fit parameters t_0 = 2 μs, α = 1.26 and U_0 = 1058 meV are reasonable within the collective creep model. Above 1 T, M(t) data was not fitting to above (cf. Eq. 5.2) form of M(t), thereby pointing to a change in the flux dynamics.

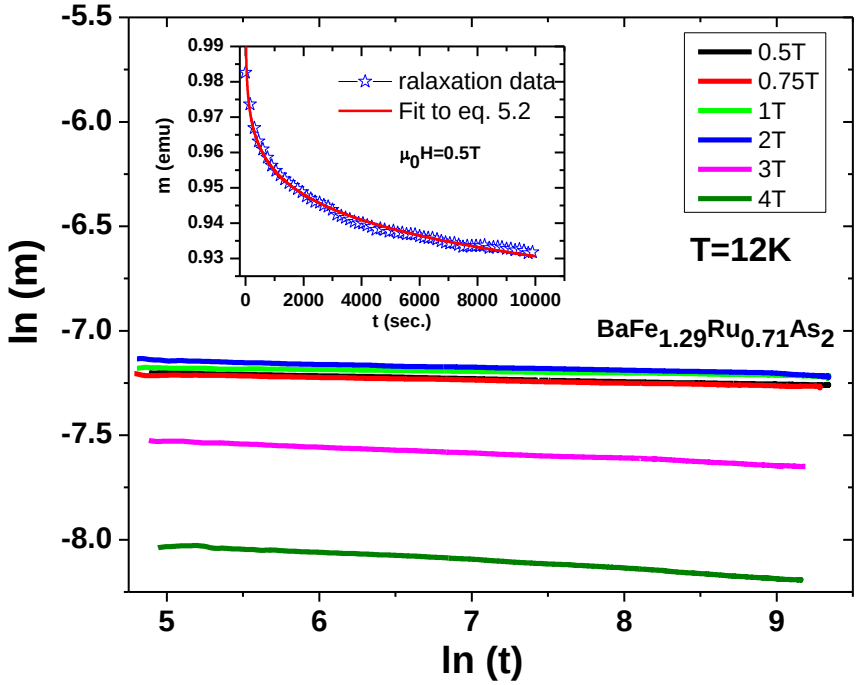

Figure 5.13: log-log plot of magnetization vs. time (t) for the x = 0.71 sample, indicates that the moments are relaxing from their critical state value over a period of time. The relaxation in magnetization was recorded for 10000 seconds at different measuring fields reached after reducing the field from much above fishtail peak. The sample was zero field cooled in all the measurements. **Inset** of the figure shows one typical relaxation curve measured at 0.5 T field and fit to equation (5.2).

A logarithmic relaxation rate **S = -[d ln |m|/d ln t]** describes the flux creep [16]. Figure 5.14 shows the field dependence of relaxation rate *S*, measured at 12 K above and below the fish-tail region. In figure 5.14, *S(H)* plot is superposed on *M(H)* loop recorded at the same temperature. As seen from figure 5.14, *S(H)* initially decreases with increasing field up to fish-tail maxima H_{SP} and thereafter increases with field. Initial fall of *S* with increasing field is in agreement with weak collective pinning creep model [18] but its subsequent increase with field cannot be explained using this model.

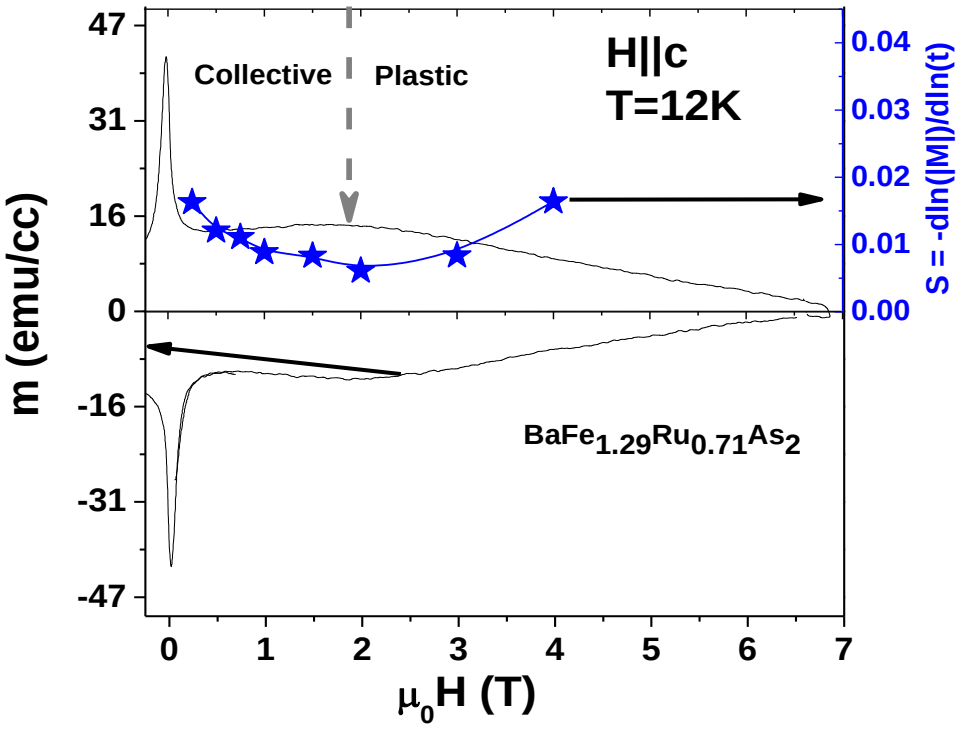

Figure 5.14: Field dependence of magnetization relaxation rate '*S*' (stars) measured below and above fish-tail region, superposed on the *M(H)* loop measured at 12 K for *H* parallel to *c-axis*. The arrow indicates the peak that delimits the collective and plastic pinning regimes in the $\mu_0 H$-*T* phase diagram.

Thus, the collective creep model is not applicable above fish-tail effect peak. It has been suggested that an increase in the relaxation rate with field can be explained by plastic creep model [16, 34] in which the thermally activated creep is not due to jump of

vortex bundles, but to sliding of dislocations in vortex lattice. Similar results have been found for $Ba(Fe_{0.93}Co_{0.07})_2As_2$ single crystals [16]. It was shown that in crystals with moderate pinning, a crossover from elastic to plastic creep is always accompanied by the fish-tail feature in M(H) isotherms [16]. The barrier for the plastic creep (U_{pl}) decreases with increase in the field $U_{pl}(H) = \frac{1}{\sqrt{H}}$ whereas the barrier for collective creep (U_c) increases with the field. In low fields, the vortex dynamics (creep) takes place through collective pinning channel, however as the field increases, the crossover from collective to plastic channel of vortex dynamics occurs when U_{pl} becomes smaller then U_c.

From similar trends of *S(H)* and occurrence of fish-tail effect in M(H) isotherms, it is inferred that a change from collective to plastic creep [16] is taking place in the fish-tail region of the isothermal M(H) loops of our $BaFe_{2-x}Ru_xAs_2$ samples also.

5.10 Vortex phase diagram

Based on the above studies comprising of transport and magnetization measurements, pinning mechanism and vortex dynamics, a vortex phase diagram of $BaFe_{2-x}Ru_xAs_2$ (x = 0.71) for $H||c$ direction is shown in figure 5.17. The phase diagram is plotted for x = 0.71 sample, that shows a pronounced second magnetization peak (see figure. 5.2). Here $\mu_0 H_{min}$ represent the field values at valley after low field peak and $\mu_0 H_{SP}$ represents a fish-tail peak at higher fields in the magnetization isotherms (see figure 5.2). Resistive transitions as a function of temperature under different magnetic fields, shown in chapter 4, (figure 4.6 (d)) were used to calculate upper critical field ($\mu_0 H_{C2}$) and irreversibility field ($\mu_0 H_{irr}$). $\mu_0 H_{C2}$ and $\mu_0 H_{irr}$ were defined by 90% and 10% of normal state resistivity criterion respectively. The curves for $\mu_0 H_{SP}$ and $\mu_0 H_{min}$ fit very well to

power law of the form $\mu_0 H_{SP}$, $H_{min} = \mu_0 H_{SP}(0)$, $H_{min}(0)\ (1-T/T_C)^n$, with $\mu_0 H_{SP}(0)$=8.27 T and $\mu_0 H_{min}(0)$=1.63 T. The value of exponent n is found to be 1.27 and 1.24 for H_{SP} and H_{min} respectively. These values of exponent 'n' are similar to those found for $Ba(Fe_{0.93}Co_{0.07})_2As_2$ by Prozorov *et al.* [16].

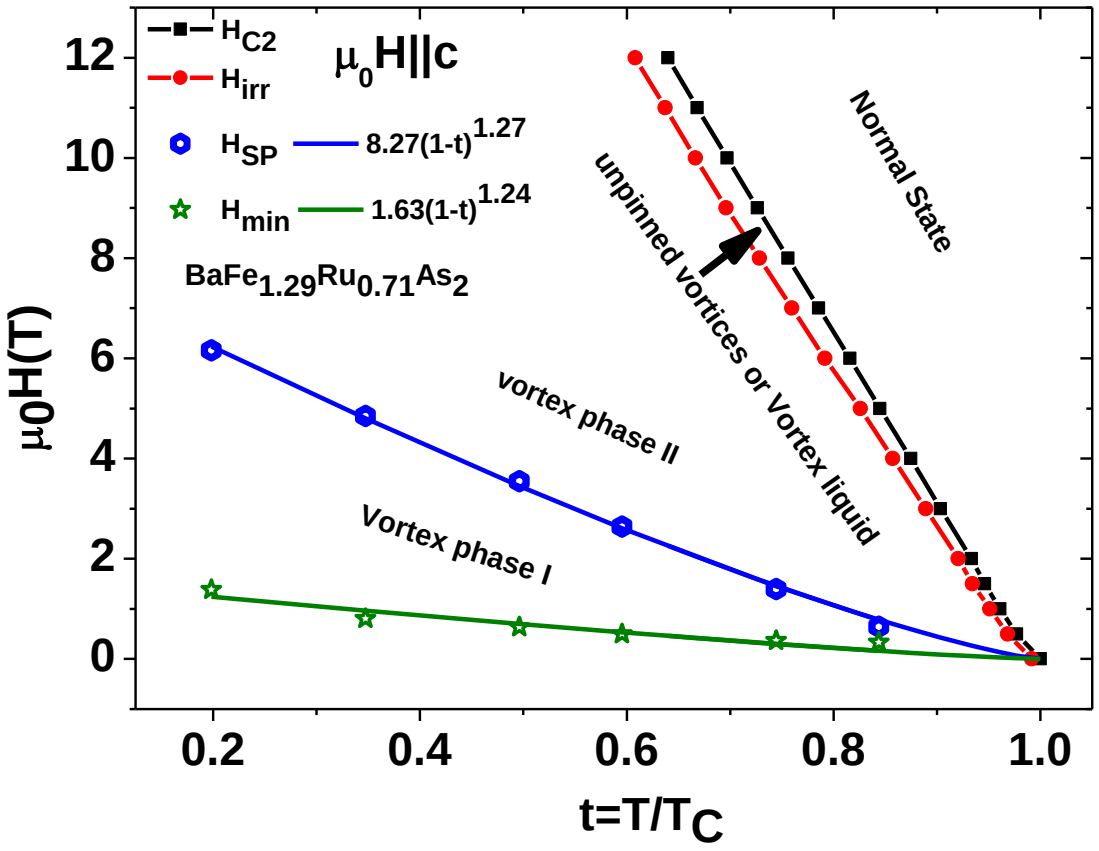

Figure 5.15: Detailed vortex phase diagram for $BaFe_{2-x}Ru_xAs_2$ (x=0.71) superconducting single crystal shows a very small region of unpinned vortices. Delineation between two different regimes of vortex dynamics [16] marked as phase I (collective creep) and phase II (plastic creep) can be seen separated by the H_{SP} line in the phase diagram.

Another noteworthy feature of the phase diagram shown in figure 5.17 is that the irreversibility line is very close to the H_{C2} curve. The irreversibility line being very close to H_{C2} is an important feature for a material to be technology-worthy as irreversibility line demarcates the field at which vortex flow is unpinned and magnetic irreversibility sets in.

A delineation between two different regimes of vortex dynamics [16] marked as phase I (collective creep) and phase II (plastic creep) can be seen separated by the H_{SP} line in the phase diagram.

5.11 Conclusions

A detailed study of the magnetic properties, critical current density, flux pinning, flux dynamics and magnetic phase diagram in $BaFe_{2-x}Ru_xAs_2$ superconducting single crystals has been presented in this chapter. The salient findings are listed below

a) The typical values of J_C are around ~10^9 A/m^2, which is comparable to that in other electron doped systems [16] of nearly same T_C. High critical current density found in these compounds making them suitable candidate for applications.
b) A fish-tail peak was observed in *M(H)* isotherms in both the directions of applied field. The presence of a fish-tail effect helps the superconductors to have high critical current densities even at high magnetic fields.
c) Thermo-magnetic history dependence in the isothermal magnetization loops was found in the samples showing pronounced fish-tail effect.
d) The thermo-magnetic cycle dependent critical current density suggests that a phase change in underlying vortex lattice which could be first order, with associated hysteresis.
e) The temperature-independent scaling behavior of the normalized pinning force density suggests one dominant pinning mechanism that is operative at all the temperatures. The symmetric $F_p(h)$ curves with a peak at h~0.45 for x = 0.71 sample may imply a dense vortex pinning structure whereas for x = 0.5 sample the peak in

normalized pinning force density is around ~0.33 and is assigned to normal core pinning.

f) Finally a $\mu_0 H-T$ vortex phase diagram is presented for $BaFe_{1.29}Ru_{0.71}As_2$ that shows different regions of vortex lattice in the superconducting phase.

References

[1] William W H 2001 *Engineering Superconductivity*, ed L J Peter: John Wiley & Sons.) pp 91-107

[2] Dew-Hughes D 2001 The critical current of superconductors: an historical review *Low Temperature Physics* **27** 713-22

[3] Gurevich A 2011 Iron-based superconductors at high magnetic fields *Reports on Progress in Physics* **74** 124501

[4] van der Beek C J, Konczykowski M, Kasahara S, Terashima T, Okazaki R, Shibauchi T and Matsuda Y 2010 Quasiparticle Scattering Induced by Charge Doping of Iron-Pnictide Superconductors Probed by Collective Vortex Pinning *Physical Review Letters* **105** 267002

[5] Shilpam S and *et al*. 2011 Superconducting And Critical Properties of $PrOFe_{0.9}$ $Co_{0.1}As$: Effect of P Doping *Superconductor Science and Technology* **24** 065020

[6] Yamamoto A, Polyanskii A A, Jiang J, Kametani F, Tarantini C, Hunte F, Jaroszynski J, Hellstrom E E, Lee P J, Gurevich A, Larbalestier D C, Ren Z A, Yang J, Dong X L, Lu W and Zhao Z X 2008 Evidence for two distinct scales of current flow in polycrystalline Sm and Nd iron oxypnictides *Superconductor Science and Technology* **21** 095008

[7] Lee S, Jiang J, Weiss J D, Folkman C M, Bark C W, Tarantini C, Xu A, Abraimov D, Polyanskii A, Nelson C T, Zhang Y, Baek S H, Jang H W, Yamamoto A, Kametani F, Pan X Q, Hellstrom E E, Gurevich A, Eom C B and Larbalestier D C 2009 Weak-link behavior of grain boundaries in superconducting $Ba(Fe_{1-x}Co_x)_2As_2$ bicrystals *Applied Physics Letters* **95** 212505-3

[8] Fang L, Jia Y, Chaparro C, Sheet G, Claus H, Kirk M A, Koshelev A E, Welp U, Crabtree G W, Kwok W K, Zhu S, Hu H F, Zuo J M, Wen H H and Shen B 2012 High, magnetic field independent critical currents in $(Ba,K)Fe_2As_2$ crystals *Applied Physics Letters* **101** 012601-5

[9] Prozorov R, Tanatar M A, Ni N, Kreyssig A, Nandi S, Bud'ko S L, Goldman A I and Canfield P C 2009 Intrinsic pinning on structural domains in underdoped single crystals of $Ba(Fe_{1-x}Co_x)_2As_2$ *Physical Review B* **80** 174517

[10] Sun D L, Liu Y and Lin C T 2009 Comparative study of upper critical field H_{C2} and second magnetization peak H_{SP} in hole- and electron-doped $BaFe_2As_2$ superconductor *Physical Review B* **80** 144515

[11] Chong S V, Hashimoto S and Kadowaki K 2010 Upper critical fields and critical current density of $BaFe_2(As_{0.68}P_{0.32})_2$ single crystal *Solid State Communications* **150** 1178-81

[12] Pramanik A K, Harnagea L, Singh S, Aswartham S, Behr G, Wurmehl S, Hess C, Klingeler R, uuml and chner B 2010 Critical current and vortex dynamics in single crystals of $Ca(Fe_{1-x}Co_x)_2As_2$ *Physical Review B* **82** 014503

[13] Gao Z, Wang L, Yao C, Qi Y, Wang C, Zhang X, Wang D, Wang C and Ma Y 2011 High transport critical current densities in textured Fe-sheathed $Sr_{1-x}K_xFe_2As_2$ + Sn superconducting tapes *Applied Physics Letters* **99** 242506-4

[14] Nakajima Y, Tsuchiya Y, Taen T, Tamegai T, Okayasu S and Sasase M 2009 Enhancement of critical current density in Co-doped $BaFe_2As_2$ with columnar defects introduced by heavy-ion irradiation *Physical Review B* **80** 012510

[15] Yang H, Luo H, Wang Z and Wen H-H 2008 Fishtail effect and the vortex phase diagram of single crystal $Ba_{0.6}K_{0.4}Fe_2As_2$ *Applied Physics Letters* **93** 142506-3

[16] Prozorov R, Ni N, Tanatar M A, Kogan V G, Gordon R T, Martin C, Blomberg E C, Prommapan P, Yan J Q, Bud'ko S L and Canfield P C 2008 Vortex phase diagram of $Ba(Fe_{0.93}Co_{0.07})_2As_2$ single crystals *Physical Review B* **78** 224506

[17] Shilpam S, Vinod K, Sundar C S and Bharathi A 2013 Critical current density and magnetic phase diagrams of $BaFe_{1.29}Ru_{0.71}As_2$ single crystals *Superconductor Science and Technology* **26** 015009

[18] Blatter G, Feigel'man M V, Geshkenbein V B, Larkin A I and Vinokur V M 1994 Vortices in high-temperature superconductors *Reviews of Modern Physics* **66** 1125

[19] Chaddah P 2003 Critical current densities in superconducting materials *Sadhana* **28** 273-82

[20] Matsushita T 2007 *Flux Pinning in Superconductors*: Springer Berlin Heidelberg)

[21] Poole C P, Farach H A, Creswick R J and Prozorov R 2007 *Superconductivity* (Netherlands: Academic Press)

[22] Bean C P 1964 Magnetization of High-Field Superconductors *Reviews of Modern Physics* **36** 31

[23] Yamamoto A, Jaroszynski J, Tarantini C, Balicas L, Jiang J, Gurevich A, Larbalestier D C, Jin R, Sefat A S, McGuire M A, Sales B C, Christen D K and Mandrus D 2009 Small anisotropy, weak thermal fluctuations, and high field superconductivity in Co-doped iron pnictide $Ba(Fe_{1-x}Co_x)_2As_2$ *Applied Physics Letters* **94** 062511-3

[24] Ishibashi T, Nakajima Y and Tamegai T 2012 Irreversible magnetization in isovalently doped $Ba(Fe_{1-x}Ru_x)_2As_2$ *Physics Procedia* **27** 104-7

[25] Ravikumar G, Sahni V C, Mishra P K, Chandrasekhar Rao T V, Banerjee S S, Grover A K, Ramakrishnan S, Bhattacharya S, Higgins M J, Yamamoto E, Haga Y, Hedo M, Inada Y and Onuki Y 1998 Manifestation of history-dependent critical currents via dc and ac magnetization measurements in single crystals of $CeRu_2$ and 2H-$NbSe_2$ *Physical Review B* **57** R11069

[26] Banerjee S S, Patil N G, Saha S, Ramakrishnan S, Grover A K, Bhattacharya S, Ravikumar G, Mishra P K, Chandrasekhar Rao T V, Sahni V C, Higgins M J, Yamamoto E, Haga Y, Hedo M, Inada Y and Onuki Y 1998 Anomalous peak effect in $CeRu_2$ and 2H-$NbSe_2$: Fracturing of a flux line lattice *Physical Review B* **58** 995

[27] Chaddah P, Chaudhary S, Roy S B, Babu P K, Nagarajan R and Gupta L C 2000 Are history effects common to all peak effects in superconductors? *Solid State Communications* **115** 445-8

[28] Ravikumar G, Bhagwat K V, Sahni V C, Grover A K, Ramakrishnan S and Bhattacharya S 2000 Phenomenological model for history effects and metastability in weakly pinned superconductors *Physical Review B* **61** R6479

[29] Chaddah P, Bhagwat K V and Ravikumar G 1989 Magnetisation hysteresis and critical current density *Physica C: Superconductivity* **159** 570-6

[30] Dew-Hughes D 1974 Flux pinning mechanisms in type II superconductors *Philosophical Magazine* **30**

[31] Kramer E J 1973 Scaling laws for flux pinning in hard superconductors *Journal of Applied Physics* **44** 1360-70

[32] Anderson P W 1962 Theory of Flux Creep in Hard Superconductors *Physical Review Letters* **9** 309-11

[33] Anderson P W and Kim Y B 1964 Hard Superconductivity: Theory of the Motion of Abrikosov Flux Lines *Reviews of Modern Physics* **36** 39-43

[34] Abulafia Y, Shaulov A, Wolfus Y, Prozorov R, Burlachkov L, Yeshurun Y, Majer D, Zeldov E, uuml, hl H, Geshkenbein V B and Vinokur V M 1996 Plastic Vortex Creep in $YBa_2Cu_3O_{7-x}$ Crystals *Physical Review Letters* **77** 1596

Chapter 6

Critical Fluctuations in $BaFe_{2-x}Ru_xAs_2$ Superconductors

In this chapter we present the dimensional scaling analysis of excess magnetization ($\Delta M(T,H)$) and excess-conductance ($\Delta\sigma(T,H)$) of Ru-substituted superconducting single crystals. Scaling analysis of the para-conductance in fields up to 11 T, performed for $BaFe_{1.2}Ru_{0.8}As_2$ also points to the three dimensional critical fluctuations. Similar analysis of the temperature dependent excess magnetization in the region of reversible magnetization of the $BaFe_{2-x}Ru_xAs_2$ (x=0.55 and 0.71) superconductors also suggest 3D nature of critical fluctuations.

6.1 Introduction

In the case of low T_C superconductors, the superconducting transition in zero field is very well described by the mean-field theory [1, 2]. This is so because the characteristic correlation lengths in such low T_C superconductors are very large, thereby making the thermodynamic fluctuations very small [1]. The temperature range ΔT around T_C, where critical phenomenon occur is given by Ginzburg criterion $G = \Delta T/T_C$ [2]. Usually G is very small ~10^{-5} to 10^{-9} for low T_C compounds and fluctuation effects are negligible [3]. The effect of thermodynamic critical fluctuations in the vicinity of superconducting transition was later on explored in reduced dimensionality systems like

amorphous thin films of Bi [4]. Further stimulus in the field came with the advent of high T_C superconductors (HTSCs) where the fluctuation effects were very pronounced due to layered structures, high superconducting transition temperatures and short *c-axis* coherence lengths. In the case of HTSCs, the Ginzburg number is large ($\sim 10^{-2}$) and thus pronounced effects of fluctuations are seen in these systems. HTSCs also show a crossover behaviour from two dimensional at high fields to three dimensional fluctuation regime at low fields [5].

Since like HTSCs, iron-pnictide superconductors have a high T_C, a layered structure and small *c-axis* coherence lengths, an enhanced fluctuation effect is also expected in FeAs based superconductors [6]. There have been several investigations on the nature of superconducting fluctuations in different FeAs based superconductors, for example in $Ba(Fe_{1-x}Co_x)_2As_2$ [7], $SmFeAs(O_{1-x}F_x)$ [8], $NdFeAs(O_{1-x}F_x)$ and $(Ba_{1-x}K_x)Fe_2As_2$ [9]. Having reported the upper critical fields, irreversibility field, critical current density and vortex structure in chapters 4 and 5, herein we explore the nature of critical fluctuations in the $BaFe_{2-x}Ru_xAs_2$ superconducting system. The nature of fluctuations in excess conductance and magnetisation prior to superconducting transition was studied using in-field transport and magnetisation measurements as a function of temperature.

6.2 Fluctuation effects in superconductors

Before, we present the experimental results, we provide a brief overview of fluctuations in superconductors and various models used to analyse them. Since the most important and very well studied phenomenon in superconductors is the observation of

zero DC resistivity, the initial progress [4, 10] in the understanding of fluctuations was made by study of excess conductivity arising due to fluctuation above the superconducting transition temperature. In the absence of an applied magnetic field, generally there are two processes that contribute for the para (excess) conductivity. The first one is the Aslamasov-Larkin (AL) contribution [11], also known as direct contribution, to the enhancement of conductivity due to acceleration of superconducting pairs. The other contribution known as indirect or Maki-Thompson (MT) [12-14] contribution, arises because of the interaction between the fluctuations and the normal quasiparticles [1].

After the first observation of fluctuation effects in the amorphous Bi film by Glover [4], the theoretical explanation was provided by Aslamasov and Larkin [11]. A more thorough treatment of the subject can be found in references [1, 15, 16]

The fluctuation conductivity in three dimensions is given by

$$\boldsymbol{\sigma_{AL}^{3D}} = \frac{\boldsymbol{e^2}}{\boldsymbol{32\hbar\xi(0)}}\frac{\boldsymbol{1}}{\sqrt{\boldsymbol{\varepsilon}}} \tag{6.1}$$

Here, $\xi(0)$ is the coherence length and $\varepsilon = ln\frac{T}{T_C} \approx \frac{T-T_C}{T_C}$.

Para-conductivity in one and two dimensions is given by [1, 15, 16]

$$\boldsymbol{\sigma_{AL}^{2D}} = \frac{\boldsymbol{e^2}}{\boldsymbol{16\hbar d}}\boldsymbol{\varepsilon^{-1}} \tag{6.2}$$

$$\boldsymbol{\sigma_{AL}^{1D}} = \frac{\boldsymbol{\pi e^2\xi(0)}}{\boldsymbol{16\hbar S}}\boldsymbol{\varepsilon^{-3/2}} \tag{6.3}$$

Wherein the thickness $d << \xi$, and cross-sectional area $S << \xi^2$.

In some cases, the observed magnitude of excess conductivity in thin films was up to an order larger than expected from AL process [1]. This additional conductivity was understood as an effect of fluctuations on the normal quasiparticles conductivity. The Maki-Thompson theory [12-14] considers the interaction of quasiparticles with superconducting fluctuations. This process is also called as the indirect contribution to the excess conductivity. When an accelerating fluctuation pair breaks into normal quasiparticles, the individual particles possess nearly opposite momentum. After scattering from impurities the quasiparticles together, tend to have a small total momentum in the direction of acceleration of original fluctuating pair, and they continue to move in the original direction [1]. However, the quasiparticles ultimately decay back into a superconducting fluctuation again, much the same way as a fluctuating pair decays back to normal quasiparticles [1].

The contributions to excess conductivity due to MT process in different dimensions are [10]:

$$\boldsymbol{\sigma_{MT}^{3D}} = \frac{\boldsymbol{e^2}}{\boldsymbol{8\hbar\xi}} \frac{\boldsymbol{1}}{\boldsymbol{\sqrt{\varepsilon}+\sqrt{\delta}}} \tag{6.4}$$

$$\boldsymbol{\sigma_{MT}^{2D}} = \frac{\boldsymbol{e^2}}{\boldsymbol{8\hbar d}} \frac{\boldsymbol{1}}{\boldsymbol{\varepsilon-\delta}} \boldsymbol{ln} \frac{\boldsymbol{\varepsilon}}{\boldsymbol{\delta}} \tag{6.5}$$

$$\boldsymbol{\sigma_{MT}^{1D}} = \frac{\boldsymbol{\pi e^2 \xi}}{\boldsymbol{4\hbar S}} \frac{\boldsymbol{1}}{\boldsymbol{\varepsilon^{3/2}}} \frac{\boldsymbol{\sqrt{\varepsilon/\delta}}}{\boldsymbol{1+\sqrt{\delta/\varepsilon}}} \tag{6.6}$$

Here δ is the reduced shift of T_C caused by the pair breaking [1]. It is clear from above equations that the MT contributions for two and one dimensions are divergent for $\delta = 0$

but the samples with finite resistance will always have some internal pair breaking, resulting in a finite value of δ [17].

In addition to AL and MT terms the excess conductivity sometimes has a contribution from fluctuations in the density of states (DOS) of normal quasiparticles. This term originates because the density of states of normal quasiparticles is affected by the formation of superconducting pairs [18]. The contribution of fluctuations in DOS has opposite sign as compared to AL and MT processes and thus decreases the conductivity.

The reduction in conductivity due to fluctuations in DOS can be written as [18]

$$\boldsymbol{\sigma^{DOS}} = \frac{\boldsymbol{\Delta n_e e^2 \tau}}{\boldsymbol{m}} = -\frac{\boldsymbol{2 n_{pair} e^2 \tau}}{\boldsymbol{m}} \qquad (6.7)$$

Where Δn_e is the change in the density of normal state carriers and n_{pair} is the density of superconducting pairs.

From all the above contributions, the excess conductivity in the regime of critical fluctuations is given by

$$\boldsymbol{\Delta\sigma^{fl}} = \boldsymbol{\sigma^{AL} + \sigma^{MT} + \sigma^{DOS}} \qquad (6.8)$$

In the case of HTSCs the MT contribution remains absent while inclusion of DOS fluctuations explains most of the puzzling features like peak in c-axis resistivity [19] and change of sign in magneto-conductivity [20].

Having provided an overview of critical fluctuations in superconductors, we now turn to the results in arsenide superconductors.

6.3 Excess conductance of $BaFe_{1.2}Ru_{0.8}As_2$ in zero magnetic field

Figure 6.1 shows the excess conductance vs. reduced temperature, ε, in a log-log plot. The excess conductance $\Delta\sigma$ was evaluated using $((R_N-R)/RR_N)$, here R_N is the normal state resistance and R is the resistance at a temperature T. The normal state resistance R_N for our single crystals was determined by fitting the $R(T)$ data (chapter 4 figure 4.6 (f)) of $BaFe_{1.2}Ru_{0.8}As_2$ superconductor (see inset 6.1) to an expression $R_N = AT+BT^{-n}$, where A, $B$and n are the fitting parameters [21]. A satisfactory fitting of the data was found in the temperature range from about 2 K above T_C (20.57 K) to ~2.5 T_C (55 K). The reduced chi square was 0.9998 and RMS error in fitting was $8.38\text{x}10^{-7}$.

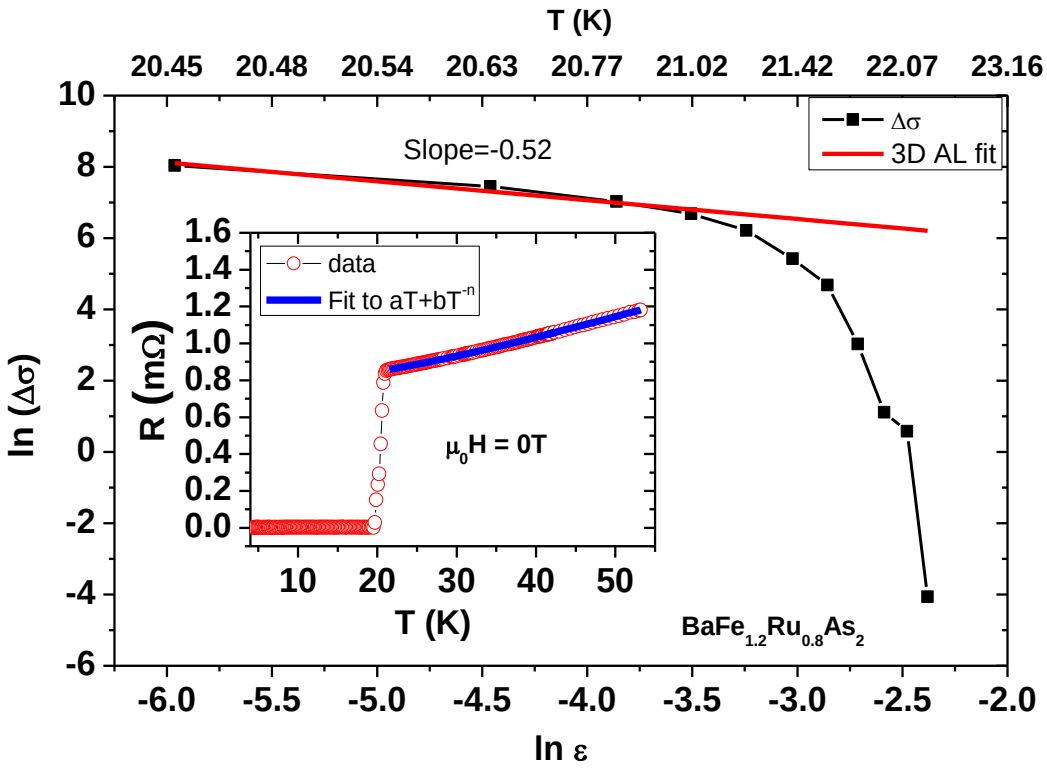

Figure 6.1: Excess conductance due to critical fluctuations near T_C in $BaFe_{1.2}Ru_{0.8}As_2$ sample. The excess conductance in zero magnetic field fits to 3D AL formula given by equation 6.1. Slope of the $\ln(\Delta\sigma)$ vs. $\ln(\varepsilon)$ plot is found to be ~ -1/2 from $\ln(\varepsilon) = 6.0$ up to 3.75 after which curve deviates from the 3D AL formalism. Inset: shows the resistance vs. temperature data in zero magnetic field. The normal state resistance was fitted to a function of the form $AT+BT^{-n}$

The excess conductance was fitted to three dimensional AL equation (6.1), and is seen to fit the data till ε = -3.5. The exponent of reduced temperature ε is found to be near to -0.53 (~ -1/2) giving a strong indication for 3D fluctuations in the Ru-substituted $BaFe_2As_2$ single crystals. The three dimensional nature of fluctuations is consistent with the low anisotropy in the system, as indicated in chapter 4. Here in the fitting of excess conductance, Maki Thompson contribution is not considered because its effect in 3D systems is expected to be small [2].

6.4 Fluctuations under magnetic field

AL theory considers the effect of fluctuations on the conductivity of superconductors in zero magnetic fields and assumes that the fluctuations in the critical region don't interact among themselves [1]. Dimensionality dependent scaling analysis of the nature of critical fluctuations developed by Ullah and Dorsey [22] is a useful tool to analyse the effect of magnetic field in the critical region around the vicinity of $\mu_0 H_{C2}(T)$. For application of the dimensionality dependent scaling analysis of critical fluctuations in thermodynamic quantities, the Lowest Landau Level (LLL) approximation is made [23]. If the magnetic field is sufficiently strong, the paired quasiparticles remain effectively confined in their Lowest Landau Level due to orbital motion around an axis along the field direction; this limits the spatial correlations transverse to the field. Due to this, the superconducting fluctuations in bulk superconductor start acquiring an effective one dimensional character along the field direction [24, 25]. The reduction of dimensionality also increases the effect of the fluctuations, resulting in fluctuation region around $T_C(H)$ which grows with the increasing field according to Ginzburg criterion [6]

$$\boldsymbol{G(H) = \frac{8\pi\kappa^2 k_B T_C H}{\phi_0 \xi_c H_{C2}^2}} \qquad (6.9)$$

where ϕ_0 is the flux quantum, κ is the Ginzburg Landau (GL) parameter, ξ_c is the *c-axis* coherence length and $\mu_0 H_{C2}$ is the upper critical field.

The scaling property of Ginzburg Landau-LLL theory for a superconductor implies [25, 26] that the free energy $F(T,H)$ near T_C must be of the form $F(T,H)=THf(At)$, where $f(At)$ is a scaling function of variable $t = [T-T_C(H)]/(TH)^{(D-1)/D}$ and D is the dimensionality of the system. The scaling forms for magnetisation and conductivity derived by Ullah *et al.* [22, 25] are:

$$\Theta = \left(\frac{T^2}{H}\right)^{1/3} F_{3D}\left(A \frac{1}{(HT)^{2/3}} \varepsilon_H\right) \qquad \text{for 3D} \qquad (6.10)$$

$$\Theta = \left(\frac{T}{H}\right)^{1/2} F_{2D}\left(B \frac{1}{(HT)^{1/2}} \varepsilon_H\right) \qquad \text{for 2D} \qquad (6.11)$$

Here Θ represents the measured quantities like excess M/H or σ, and With $\varepsilon_H = T-T_C(H)$. The values of A and B are temperature and field independent appropriate constants characterizing the materials. F_{3D} and F_{2D} are the scaling functions for three and two dimensional systems and are difficult to be determined. Tesanovic *et al.* [26] have found exact scaling function using GL formalism in the extreme high field regime of a two dimensional system. Analyses of the dimensionality of the superconducting fluctuations in the critical region of $BaFe_{2-x}Ru_xAs_2$ superconducting single crystals are presented for excess conductance and magnetism in the subsequent sections.

6.4.1 Scaling analysis of excess conductance

The resistance vs. temperature data for $BaFe_{1.2}Ru_{0.8}As_2$ single crystal, measured under several magnetic fields applied parallel to *c*-axis is presented in main panel of figure 6.2 (see also chapter 4). The fluctuations in the conductance are reflected as a small broadening near the superconducting transition (marked by square in figure 6.2).

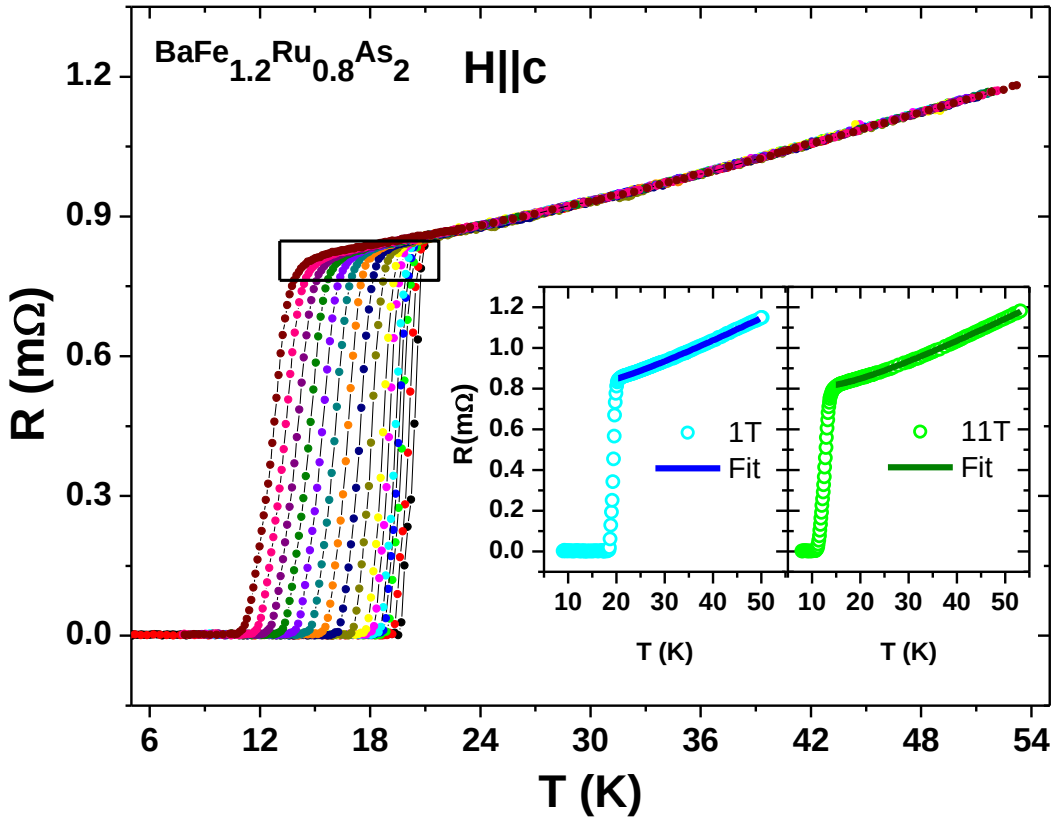

Figure 6.2: The *R(T)* plot for $BaFe_{1.2}Ru_{0.8}As_2$ superconducting single crystals under magnetic field applied parallel to *c-axis* shows broadening of the transition region near the T_C. **Inset:** Fitting of normal state resistance of the compound under field of 1 T and 11 T, to the polynomial of the form $AT+BT^{-n}$.

Shown in inset is the fitting of normal state resistance (R_N) to a polynomial of the form $AT+BT^{-n}$ for *R(T)* data at 1 T and 11 T. The same functional form is seen to fit for all *R(T)* data at all fields, and no magneto-resistance is seen in the normal state. To

unambiguously extract the contribution of excess conductance, the fitting in the normal state was carried out over a temperature range T_C+2 K to 2.5 times T_C, viz., 55 K.

The excess conductance estimated from ($1/R_N$-$1/R$) is shown in figure 6.3. Plots for excess conductance vs. reduced temperature 'ε' clearly show the broadening as a function of magnetic field. The dimensional scaling of excess conductance in terms of 3D and 2D functions are presented in figure 6.4 and 6.5 respectively. It is seen from figure 6.4 that a plot of $\Delta\sigma(H^{1/3}/T^{2/3})$ *vs.* $[(T-T_C(H))/(TH)^{2/3}]$ collapse on to a single curve, indicating the 3D nature of fluctuations. The mean field transition temperatures $T_m(H)$ have been used for scaling the excess conductance data. In contrast, as seen from figure 6.5, the plots of $\Delta\sigma(H/T)^{1/2}$ *vs.* $[(T-T_C(H))/(TH)^{1/2}]$, corresponding to 2D fluctuations do not collapse into a single curve.

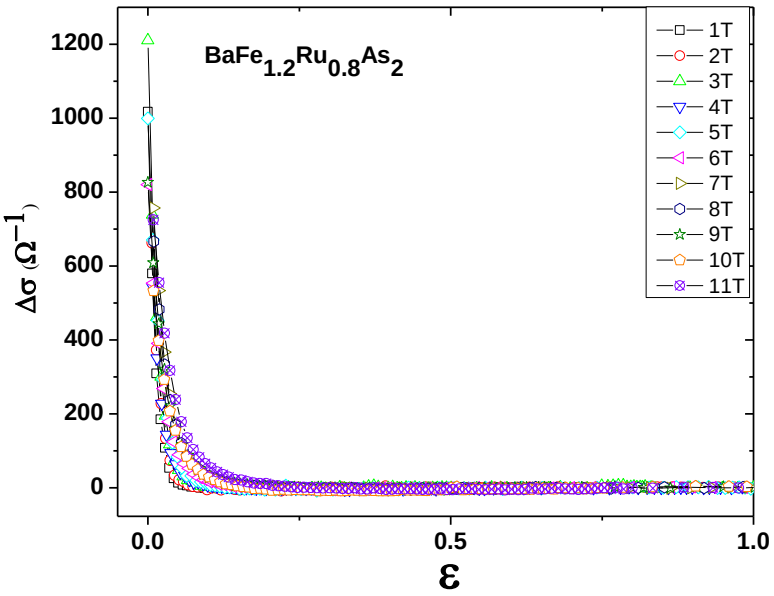

Figure 6.3: Excess conductance as a function of reduced temperature 'ε' for several magnetic fields applied parallel to c-axis. The excess conductivity was estimated using ($1/R_N$-$1/R$) where R_N was determined by fitting normal state resistance as described in figure 6.2. Broadening due to field dependent fluctuation effects is seen to increase with field.

It is thus clear that the nature of the superconducting critical fluctuations in the presence of magnetic field is three dimensional. This is consistent with the low anisotropy ~2 in the $BaFe_{2-x}Ru_xAs_2$ superconductors as found in chapter 4.

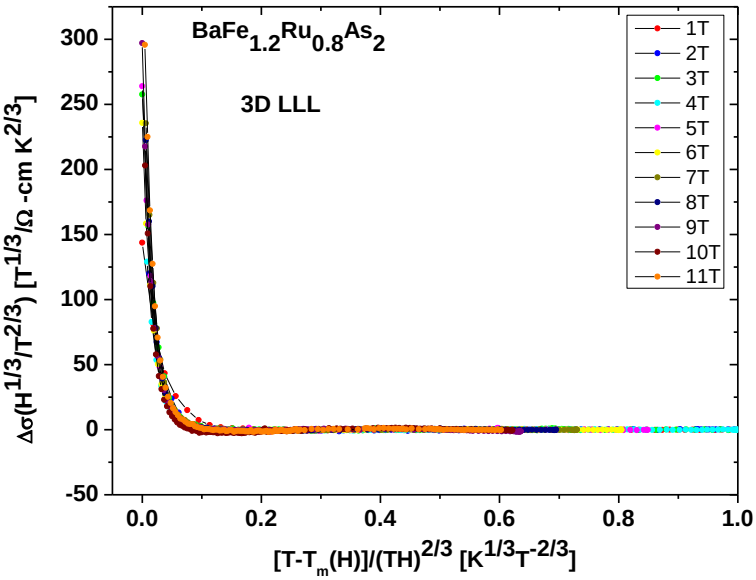

Figure 6.4: Three dimensional scaling of the excess conductance. All the excess conductivity plots beyond 1 T and up to 11 T are seen to fall on a single curve.

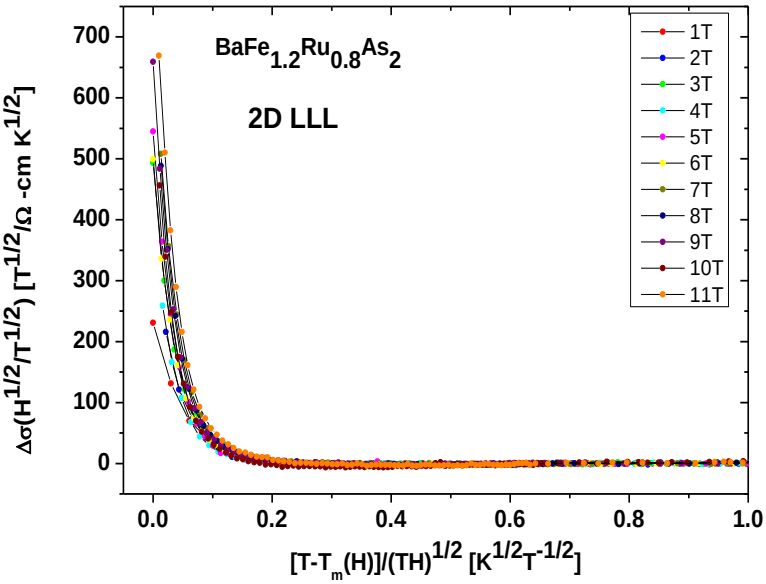

Figure 6.5: Two dimensional LLL scaling analysis of excess conductivity for $BaFe_{1.2}Ru_{0.8}As_2$ single crystal. The scaled plots of excess conductivity do not fall on a single curve. Possibility of two dimensional fluctuation effects is ruled out up to 11 T field.

Having studied the critical fluctuations in $BaFe_{1.2}Ru_{0.8}As_2$, it was of interest to investigate if the nature of fluctuations changes with Ru composition. This was attempted through an analysis of *R(T)* plots of the superconducting $BaFe_{2-x}Ru_xAs_2$ single crystals under magnetic field (see Chapter 4). However, In all the under-substituted superconducting single crystals, the *R(T)* plots show a very broad hump (See Figure 4.1) which restricted the polynomial fitting of the normal state resistance of the single crystals and hence the correct determination of excess conductance. While we have not been able to do the scaling analysis, for various Ru compositions, from the resistance data, magnetisation being a thermodynamic quantity is not subject to the uncertainties in the interpretation that arises concerning dynamical and non-equilibrium properties [27], the dimensionality dependent scaling analysis has been possible from magnetisation studies, as discussed in the following.

6.4.2 Fluctuation effects in reversible magnetisation

The diamagnetic response of $BaFe_{1.45}Ru_{0.55}As_2$ superconducting single crystal was recorded for different fields up to 8 T, applied parallel to *c-axis*. Measurements were performed using vibrating sample magnetometer. Figure 6.6 shows the zero field cooled (*ZFC*) plots of magnetisation as a function of temperature. Each curve was recorded after cooling the sample in zero field and then recording magnetisation in the presence of a measuring field. After each measurement, for a particular field, the field was switched off and the sample was warmed up to temperatures well above the T_C. The superconducting transition can be seen shifting to lower temperatures with increasing magnetic field. A rounding of the curves can be seen near the transition temperature. The plots shift parallel to each other with increasing field,

which is similar to typical mean field behaviour. The normal state magnetisation shows considerable scatter ~ 10^{-4} emu due to a small magnetisation value in normal state. The raw data were shifted constantly to have M=0 at 20 K.

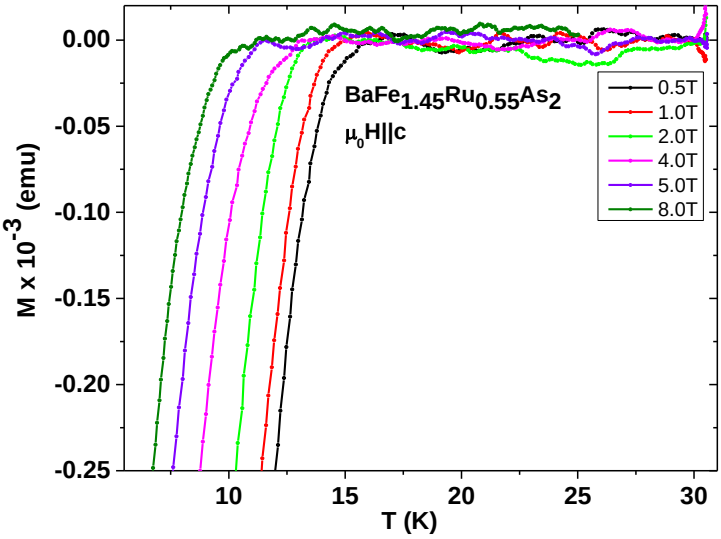

Figure 6.6: Zero field cooled diamagnetic magnetisation response of $BaFe_{1.45}Ru_{0.55}As_2$ superconducting single crystal. The magnetic fields were applied parallel to c-axis on zero field cooled samples and magnetisation was recorded as a function of increasing temperature. The *M(T)* curves shift to lower temperatures, parallel to each other with increasing field, but a small, effect of fluctuations can be seen as rounding of *M(T)* plots near T_C in the reversible magnetisation regime.

The three dimensional lowest Landau level scaling of reversible magnetisation vs. temperature was performed with the above data. The scaled curves of $[M/(TH)^{2/3}]$ vs. $[(T-T_C(H))/(TH)^{2/3}]$ are shown in figure 6.7. All the curves are seen to collapse on one another, indicating a *3D* scaling behaviour. This provides further evidence, over and above resistance measurements (see figure 6.4) that the fluctuations in $BaFe_{2-x}Ru_xAs_2$ system are three dimensional in full temperature and field range studied.

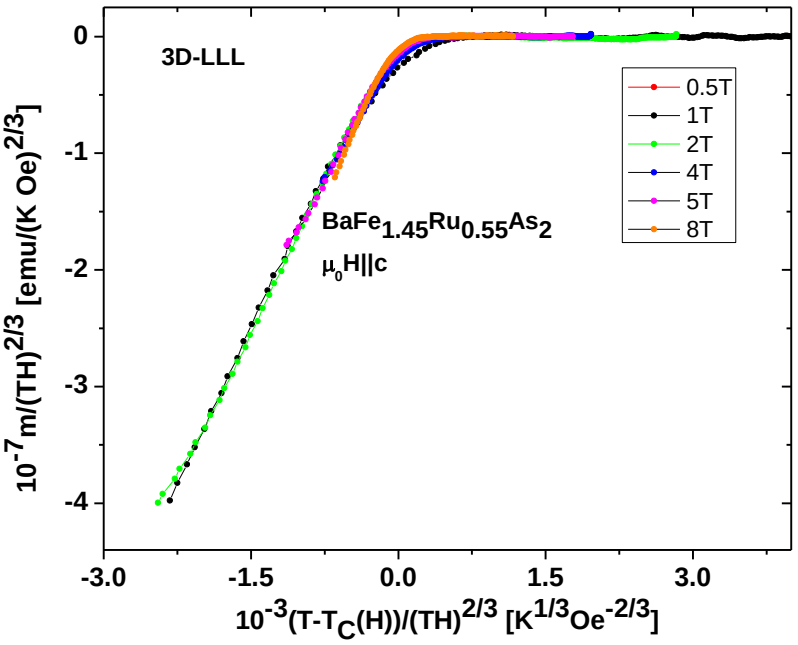

Figure 6.7: Three dimensional LLL scaling of reversible magnetisation of $BaFe_{1.45}Ru_{0.55}As_2$ single crystal under applied magnetic fields up to 8 T. All the scaled curves are falling on a single function F_{3D} characteristic of the given sample. This again substantiate that the fluctuations in $BaFe_{2-x}Ru_xAs_2$ system are three dimensional.

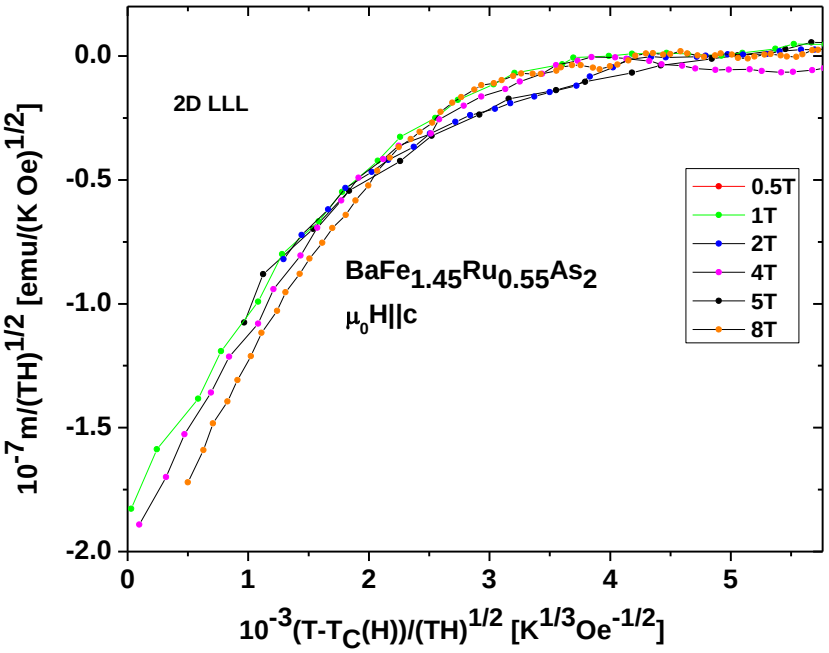

Figure 6.8: 2D-lowest Landau level scaling curves of reversible magnetisation of $BaFe_{1.45}Ru_{0.55}As_2$ single crystal under applied magnetic fields as high as 8 T. It can be seen that the scaled plots do not follow a single functional form. The curves are not scaling and thus it can be emphasised that the fluctuations in the system are not two dimensional.

As in the case of resistance measurements (see figure 6.5), a two dimensional lowest Landau level scaling analysis of the reversible magnetisation of $x = 0.55$ sample was performed using equation 6.11. The plot of $[M/(TH)^{1/2}]$ *vs.* $[(T-T_C(H))/(TH)^{1/2}]$ for various fields up to 8 T are shown in figure 6.8. The scaled plots of magnetisation are not falling on one another, indicating that the fluctuations giving rise to excess magnetisation in the critical region are not two dimensional.

The scaling analysis for another Ru composition, $BaFe_{1.29}Ru_{0.71}As_2$, is shown in figure 6.9. The inset shows the zero field magnetisation versus temperature curves [28]. The main panel of figure 6.9 shows the 3D-lowest Landau level scaling analysis for the excess magnetisation of $BaFe_{1.29}Ru_{0.71}As_2$.

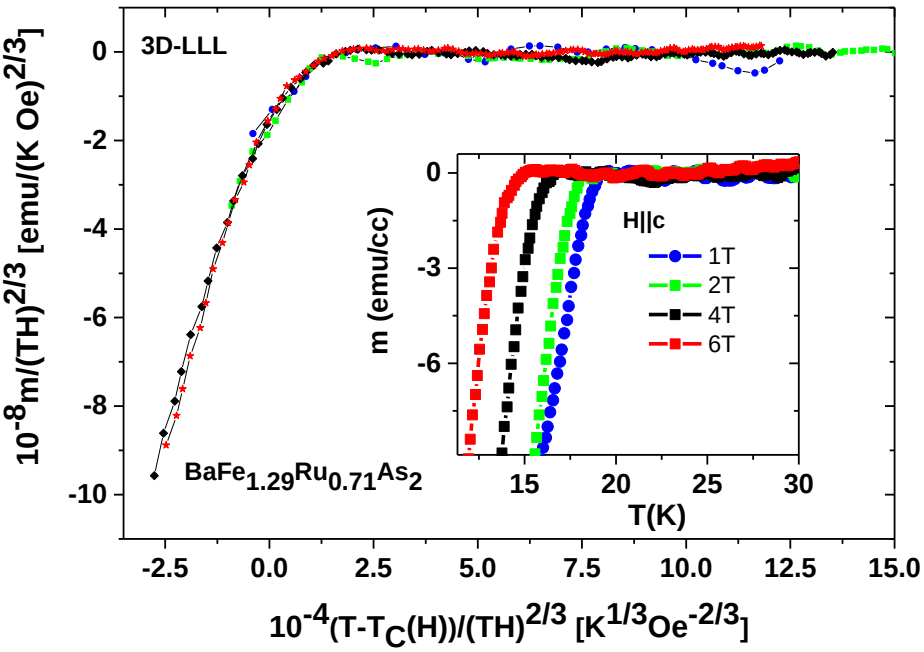

Figure 6.9: 3D lowest Landau level scaling analysis of excess magnetisation for $BaFe_{1.29}Ru_{0.71}As_2$ superconducting single crystals. Three dimensional scaling of fluctuation magnetisation suggests the existence of three dimensional superconductivity in these compounds. **Inset:** Magnetisation as a function of temperature for various magnetic fields applied parallel to c-axis on $BaFe_{1.71}Ru_{0.29}As_2$ single crystal.

In this case too, the three dimensional scaling function describes the excess magnetisation due to superconducting fluctuations. These scaling analyses of excess magnetisation for two different superconducting samples having different T_C and varying Ru-substitutions provide substantive evidence that the $BaFe_{2-x}Ru_xAs_2$ system is a three dimensional superconducting system.

Similar dimensional scaling analysis of excess conductivity and excess magnetisation near the critical region have been carried out in K-doped $Ba_{1-x}K_xFe_2As_2$ (hole doped) [29] and Co-doped $Ba(Fe_{1-x}Co_x)_2As_2$ (electron doped) [7, 30], wherein also a three dimensional scaling in the critical fluctuation region, has been observed. It is seen that similar to charge doped $BaFe_2As_2$ superconductors, the isovalent Ru-substituted family of $BaFe_{2-x}Ru_xAs_2$ superconductors also belongs to class of three dimensional superconductors.

References

[1] Skocpol W J and Tinkham M 1975 Fluctuations near superconducting phase transitions *Reports on Progress in Physics* **38** 1049

[2] Welp U, Fleshler S, Kwok W K, Klemm R A, Vinokur V M, Downey J, Veal B and Crabtree G W 1991 High-field scaling behavior of thermodynamic and transport quantities of $YBa_2Cu_3O_{7-\delta}$ near the superconducting transition *Physical Review Letters* **67** 3180-3

[3] Lobb C J 1987 Critical fluctuations in high-T_C superconductors *Physical Review B* **36** 3930-2

[4] Glover R E 1967 Ideal resistive transition of a superconductor *Physics Letters A* **25** 542-4

[5] Rosenstein B, Shapiro B Y, Prozorov R, Shaulov A and Yeshurun Y 2001 Fluctuations in single-crystal $YBa_2Cu_3O_{6.5}$: Evidence for crossover from two-dimensional to three-dimensional behavior *Physical Review B* **63** 134501

[6] Gurevich A 2011 Iron-based superconductors at high magnetic fields *Reports on Progress in Physics* **74** 124501

[7] Kim S H, Choi C H, Jung M-H, Yoon J-B, Jo Y-H, Wang X F, Chen X H, Wang X L, Lee S-I and Choi K-Y 2010 Fluctuation conductivity of single-crystalline $BaFe_{1.8}Co_{0.2}As_2$ in the critical region *Journal of Applied Physics* **108** 063916-4

[8] Pallecchi I, Fanciulli C, Tropeano M, Palenzona A, Ferretti M, Malagoli A, Martinelli A, Sheikin I, Putti M and Ferdeghini C 2009 Upper critical field and fluctuation conductivity in the critical regime of doped SmFeAsO *Physical Review B* **79** 104515

[9] Kacmarcik J, Marcenat C, Klein T, Pribulova Z, van der Beek C J, Konczykowski M, Budko S L, Tillman M, Ni N and Canfield P C 2009 Strongly dissimilar vortex-liquid regimes in single-crystalline NdFeAs(O,F) and $(Ba,K)Fe_2As_2$: A comparative study *Physical Review B* **80** 014515

[10] Holm W 1996 Superconducting fluctuations as a tool to determine microscopic properties of $YBa_2Cu_3O_{7-\delta}$. In: *Department of Solid State Physics,* (Stockholm: Royal Institute of Technology) p 11

[11] Aslamasov L G and Larkin A I 1968 The influence of fluctuation pairing of electrons on the conductivity of normal metal *Physics Letters A* **26** 238-9

[12] Maki K 1968 The Critical Fluctuation of the Order Parameter in Type-II Superconductors *Progress of Theoretical Physics* **39** 897

[13] Maki K 1968 Critical Fluctuation of the Order Parameter in a Superconductor. I *Progress of Theoretical Physics* **40** 193

[14] Thompson R S 1970 Microwave, Flux Flow, and Fluctuation Resistance of Dirty Type-II Superconductors *Physical Review B* **1** 327-33

[15] Abrahams E and Woo J W F 1968 Phenomenological theory of the rounding of the resistive transition of superconductors *Physics Letters A* **27** 117-8

[16] Schmid A 1968 The resistivity of a superconductor in its normal state *Z. Physik* **215** 210-2

[17] Patton B R 1971 Fluctuation Theory of the Superconducting Transition in Restricted Dimensionality *Physical Review Letters* **27** 1273-6

[18] Varlamov A A, Balestrino G, Milani E and Livanov D V 1999 The Role Of Density Of States Fluctuations In The Normal State Properties Of High T_C Superconductors *Advances in Physics* **48** 655-783

[19] Balestrino G, Marinelli M, Milani E, Varlamov A A and Yu L 1993 Experimental evidence in favor of the fluctuation origin of the transverse-resistance increase near the edge of the superconducting transition in $Bi_2Sr_2CaCu_2O_{8+\delta}$ *Physical Review B* **47** 6037-42

[20] Axnäs J, Holm W, Eltsev Y and Rapp Ö 1996 Sign Change of c-Axis Magnetoconductivity in $YBa_2Cu_3O_{7-\delta}$ Single Crystals *Physical Review Letters* **77** 2280-3

[21] Ong N P, Wang Z Z, Hagen S, Jing T W, Clayhold J and Horvath J 1988 Transport and tunneling studies on single crystals of $YBa_2Cu_3O_7$ *Physica C: Superconductivity* **153–155, Part 3** 1072-7

[22] Ullah S and Dorsey A T 1991 Effect of fluctuations on the transport properties of type-II superconductors in a magnetic field *Physical Review B* **44** 262-73

[23] Li D and Rosenstein B 1999 Lowest Landau level approximation in strongly type-II superconductors *Physical Review B* **60** 9704-13

[24] Lee P A and Shenoy S R 1972 Effective Dimensionality Change of Fluctuations in Superconductors in a Magnetic Field *Physical Review Letters* **28** 1025-8

[25] Wahl A, Hardy V, Warmont F, Maignan A, Delamare M P and Simon C 1997 Scaling behavior of conductivity and magnetization in high-temperature superconductors *Physical Review B* **55** 3929-34

[26] Tešanović Z, Xing L, Bulaevskii L, Qiang L and Suenaga M 1992 Critical fluctuations in the thermodynamics of quasi-two-dimensional type-II supeconductors *Physical Review Letters* **69** 3563-6

[27] Kivelson S A and Fradkin E H 2010 Fluctuation diamagnetism in high-temperature superconductors *Physics* **3** 15

[28] Sharma S, Vinod K, Sundar C S and Bharathi A 2012 Evidence of 3D fluctuations in magnetization of $BaFe_{1.25}Ru_{0.75}As_2$ single crystal *AIP Conference Proceedings* **1447** 885-6

[29] Salem-Sugui S, Ghivelder L, Alvarenga A D, Pimentel J L, Luo H, Wang Z and Wen H-H 2009 Superconducting fluctuations in the reversible magnetization of the iron-pnictide $Ba_{1-x}K_xFe_2As_2$ *Physical Review B* **80** 014518

[30] Changho C, Soo Hyun K, Ki-Young C, Myung-Hwa J, Sung-Ik L, Wang X F, Chen X H and Wang X L 2009 The fluctuation effect of $BaFe_{1.8}Co_{0.2}As_2$ single crystals from reversible magnetization *Superconductor Science and Technology* **22** 105016

Chapter 7

Summary and Conclusions

In this thesis, we have presented the discovery of new superconducting system by isovalent Ru substitution at Fe site in $BaFe_2As_2$ parent compound, and investigated its critical properties. The key results and findings of the study are listed below.

It is shown that Ru-substitution, similar to charge doping and external pressure suppresses the spin density wave ground state and stabilizes superconductivity in $BaFe_2As_2$. Through the transport and magnetization measurements on single crystalline samples with different Ru fractions, the phase diagram has been established. Paramagnetic (PM), Antiferromagnetic (AF) and superconducting (SC) ground states are shown in phase diagram.

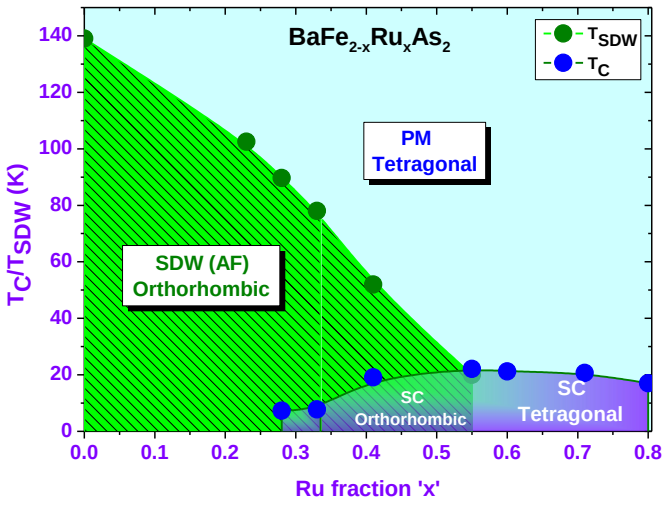

In an effort to understand the superconductivity in the Ru doped system, detailed band structure calculations have been carried out, that show an increased density of carriers at Fermi level. Further, these calculations also revealed that the magnetic moment on Fe gets suppressed for superconducting compositions, substantiated by Mossbauer studies.

X-ray diffraction experiments have been carried out to investigate the variation of structural parameters like FeAs bond length, tetrahedra angles, and arsenic height in the $FeAs_4$ tetrahedral, for various Ru compositions, to correlate with the observed T_C. The largest T_C of 22 K was found to occur for distorted $FeAs_4$ tetrahedra. The temperature dependence of the degree of orthorhombicity, across the SDW and superconducting transition has been followed for various $BaFe_{2-x}Ru_xAs_2$ single crystals. The structural phase transition was found to shift to lower temperatures with increasing Ru content. For the x=0.55 sample, no discernable change in the orthorhombic distortion was found below superconducting transition temperature but this needs to be investigated further.

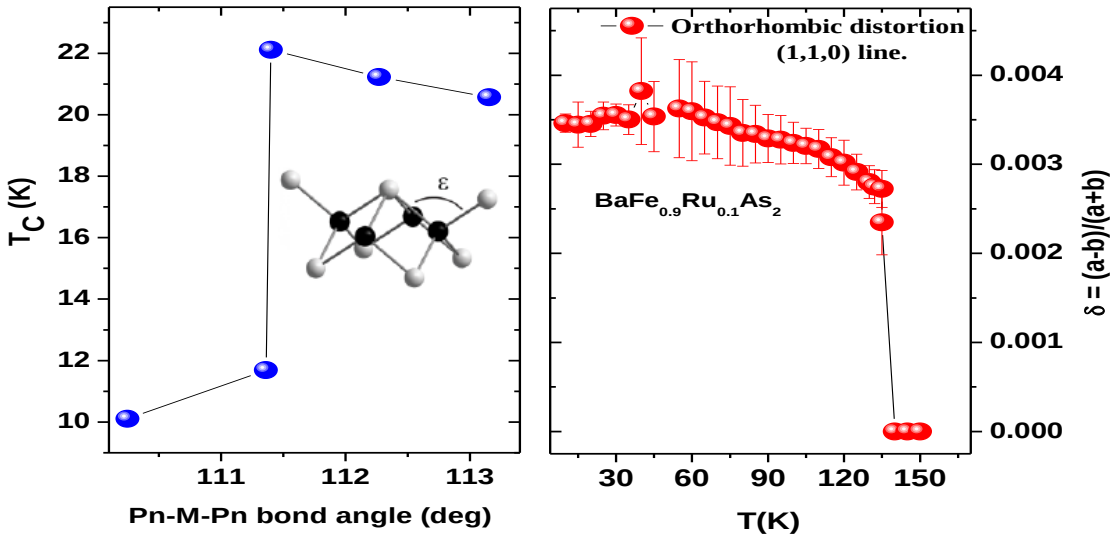

The critical fields and critical currents of the Ru-substituted samples have been investigated through resistivity and magnetization measurements. Through experiments on single crystals, the anisotropies in the critical properties have been examined. Based on the temperature variation of upper critical field, irreversibility field and features in isothermal magnetization, a magnetic phase diagram showing different vortex phases has been proposed.

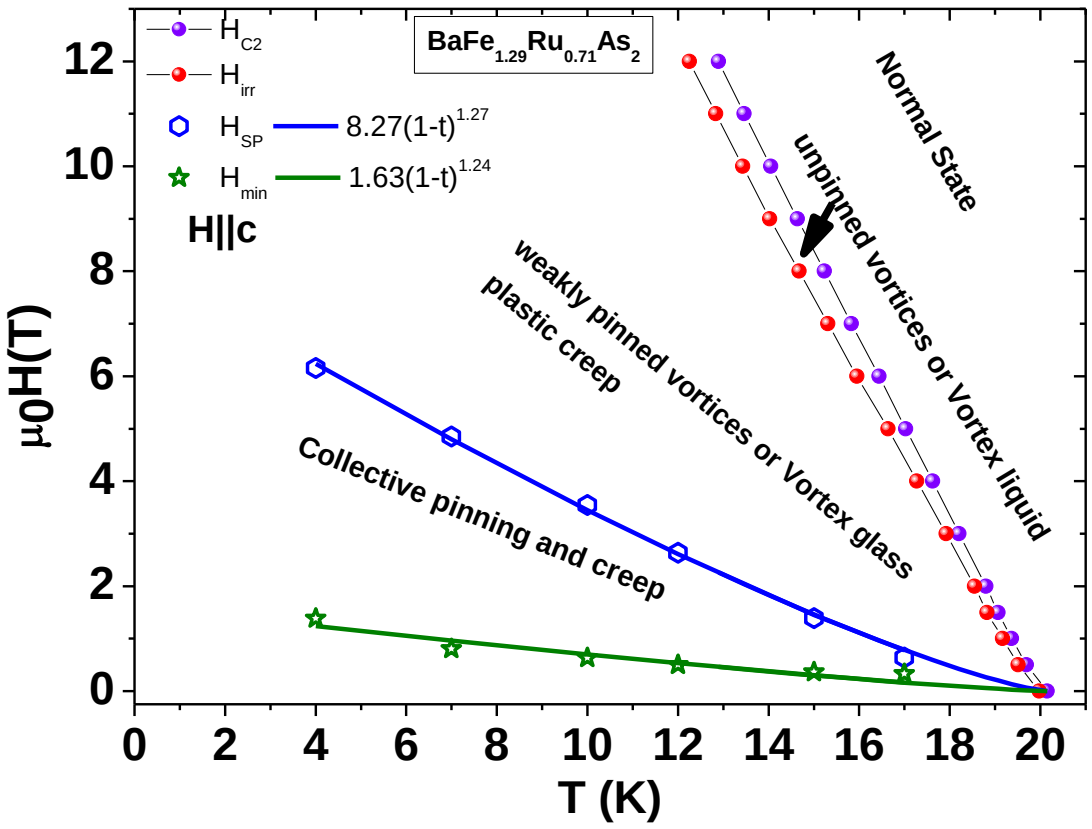

The critical fluctuations in Ru-substituted $BaFe_{2-x}Ru_xAs_2$ have been investigated through a study of the conductivity and magnetization in the vicinity of the superconducting phase transition. An analysis of the scaling behavior of the excess

conductivity ($\Delta\sigma(T)$) and magnetization ($\Delta M(T)$), points to the existence of 3D fluctuations in this system.

Future Outlook

The observation of superconductivity in $BaFe_{2-x}Ru_xAs_2$ has added another system to the 122 family of arsenide superconductors. The interest accrues from the fact that superconductivity has been obtained by an isovalent substitution of Fe by Ru. Given that this investigation in itself was motivated by the observation of pressure induced superconductivity in pristine $BaFe_2As_2$, it would be of interest to carry out the effect of pressure on superconductivity in $BaFe_{2-x}Ru_xAs_2$.

One of the generic features, accruing from investigations on various doped arsenide superconductors, is the importance of Fe-As bond lengths and angles. While these have been investigated in the Ru-doped system too, as reported in the present thesis, further high resolution structural studies on the variation of orthorhombic distortion across the superconducting transition, and a comparison with other doped system such as the $BaFe_{2-x}Co_xAs_2$ would be worthwhile.

The results on the critical properties of the $BaFe_{2-x}Ru_xAs_2$ indicate that they have high critical fields, irreversibility fields and critical currents. These coupled to low anisotropy, suggest that attempts at technical exploitation can also be pursued. These would suggest taking up studies on thin films and attempts to make superconducting wires from these compounds using powder in tube method.

List of Publications

Included in thesis

1. Superconductivity in Ru-substituted polycrystalline $BaFe_{2-x}Ru_xAs_2$, Shilpam Sharma, et.al Physical Review B 81 (2010) 174512.

2. ICDD PDF data submission for $BaFe_{1.125}Ru_{0.875}As_2$ Shilpam Sharma, A. Bharathi, V.S. Sastry, PDF release 2013, International Centre for Diffraction Data 2011

3. Critical current density and magnetic phase diagram of BaFe1.29Ru0.71As2 single crystals Shilpam Sharma, K. Vinod, A.T. Satya, A. Bharathi and C.S. Sundar, Supercond. Sci. Technol. 26 (2013) 015009

4. Evidence of 3D fluctuations in magnetization of $BaFe_{1.25}Ru_{0.75}As_2$ single crystal, Shilpam Sharma, K. Vinod, C. S. Sundar, and A. Bharathi, AIP Conf. Proc. 1447 (2012) 885.

5. Phase diagram of Ru doped $BaFe_2As_2$ K. Vinod, Shilpam Sharma, A. T. Satya, C. S. Sundar, and A. Bharathi, AIP Conf. Proc. 1447 (2012) 889.

Not included in thesis

1. Superconducting and critical properties of $PrOFe_{0.9}Co_{0.1}As$: effect of P doping, Shilpam Sharma et.al. Superconductor Science & Technology 24 (2011) 065020.

2. Effect of external perturbations induced charge-order melting in $Pr_{0.5}Ca_{0.5}MnO_3/YBa_2Cu_3O_7/ Pr_{0.5}Ca_{0.5}MnO_3$ trilayer heterostructures Dipak Kumar Baisnab, M. P. Janawadkar, Shilpam Sharma, R. M. Sarguna, L. S. Vaidhyanathan and A. Bharathi, Submitted to Journal of Applied physics

3. ^{75}As NMR probe of antiferromagnetic fluctuations in $Ba(Fe_{1-x}Ru_x)_2As_2$ Tusharkanti Dey, P. Khuntia, A. V. Mahajan, Shilpam Sharma, A. Bharathi, Journal of Physics: Condensed Matter, 23 (2011) 475701.

4. Upper critical field anisotropy in $BaFe_{2-x}Co_xAs_2$ single crystals synthesized without flux, K. Vinod, A. T. Satya, Shilpam Sharma, C. S. Sundar, and A. Bharathi, Physical Review B 84 (2011) 012502.

5. High Pressure Studies on $RuIn_3$ single crystal,
   Awadhesh Mani, Shilpam Sharma, Sharat Chandra, and A. Bharathi, J. Phys.: Condens. Matter 23 (2011) 205802 .

6. Critical properties of superconducting $Ba_{1-x}K_xFe_2As_2$,
   A. Bharathi, Shilpam Sharma, S. Paulraj, A.T. Satya, Y. Hariharan, C.S. Sundar, Physica C 470 (2010) 8-11.

7. Kohler's rule in $Ba_{1-x}K_xFe_2As_2$,
   N. Ghosh, A. Bharathi, A.T. Satya, Shilpam. Sharma, Awadhesh Mani, R. M. Sarguna, D. Sornadurai, V.S. Sastry and C.S. Sundar, Solid State Communications 150 (2010) 19401943.

8. Critical Field and Critical Current Density in $PrOFe_{0.9}Co_{0.1}As$: Effect of P Substitution
   Shilpam Sharma, J. Prakash, G. S. Thakur, A. Bharathi, A.K. Ganguli, C.S. Sundar, AIP Conf. Proc. 1349 (2011), 899.

9. Dirac cone states in Ru doped $BaFe_2As_2$ as observed by magneto resistance measurements,
   A. T. Satya, K. Vinod, Shilpam Sharma, C. S. Sundar, and A. Bharathi, AIP Conf. Proc. 1447 (2012), 901.

10. Hall Coefficient measurements in $Ba_{1-x}K_xFe_2As_2$ superconductor
    Shilpam Sharma, A.Bharathi, Y. Hariharan and C.S. Sundar, Proceedings of 53rd DAE Solid State Physics Symposium (2008)